UNIVERSIDAD COMPLUTENSE DE MADRID
FACULTAD DE CIENCIAS FÍSICAS

TESIS DOCTORAL

Simulaciones Monte Carlo de confinamiento de iones rápidos en stellarators : modelado, teoría y validación experimental de forzado de corriente por inyección de haces neutros en TJ-II y cálculos de pérdidas tempranas en configuraciones helias

Monte Carlo simulations of fast-ion confinement in stellarators : modelling, theory and experimental validation of neutral-beam current drive in TJ-II and evaluation of prompt losses in helias configurations

MEMORIA PARA OPTAR AL GRADO DE DOCTOR

PRESENTADA POR

Sadig Mulas Gassim al Seed

Director

Álvaro Cappa Ascasíbar

Madrid

UNIVERSIDAD COMPLUTENSE DE MADRID
FACULTAD DE CIENCIAS FÍSICAS

TESIS DOCTORAL

SIMULACIONES MONTE CARLO DE CONFINAMIENTO DE IONES RÁPIDOS EN STELLARATORS: MODELADO, TEORÍA Y VALIDACIÓN EXPERIMENTAL DE FORZADO DE CORRIENTE POR INYECCIÓN DE HACES NEUTROS EN TJ-II Y CÁLCULOS DE PÉRDIDAS TEMPRANAS EN CONFIGURACIONES HELIAS

MONTE CARLO SIMULATIONS OF FAST-ION CONFINEMENT IN STELLARATORS: MODELLING, THEORY AND EXPERIMENTAL VALIDATION OF NEUTRAL-BEAM CURRENT DRIVE IN TJ-II AND EVALUATION OF PROMPT LOSSES IN HELIAS CONFIGURATIONS

MEMORIA PARA OPTAR AL GRADO DE DOCTOR

PRESENTADA POR

SADIG MULAS GASSIM AL SEED

DIRECTOR

ÁLVARO CAPPA ASCASÍBAR

UNIVERSIDAD COMPLUTENSE DE MADRID
FACULTAD DE CIENCIAS FÍSICAS

TESIS DOCTORAL

SIMULACIONES MONTE CARLO DE CONFINAMIENTO DE IONES RÁPIDOS EN STELLARATORS:
MODELADO, TEORÍA Y VALIDACIÓN EXPERIMENTAL DE FORZADO DE CORRIENTE POR INYECCIÓN DE HACES NEUTROS EN TJ-II Y CÁLCULOS DE PÉRDIDAS TEMPRANAS EN CONFIGURACIONES HELIAS

MONTE CARLO SIMULATIONS OF FAST-ION CONFINEMENT IN STELLARATORS:
MODELLING, THEORY AND EXPERIMENTAL VALIDATION OF NEUTRAL-BEAM CURRENT DRIVE IN TJ-II AND EVALUATION OF PROMPT LOSSES IN HELIAS CONFIGURATIONS

MEMORIA PARA OPTAR AL GRADO DE DOCTOR

PRESENTADA POR

SADIG MULAS GASSIM AL SEED

DIRECTOR

ÁLVARO CAPPA ASCASÍBAR

Simulaciones Monte Carlo de confinamiento de iones rápidos en stellarators

Modelado, teoría y validación experimental de forzado de corriente por inyección de neutros en TJ-II y cálculos de pérdidas tempranas en configuraciones helias

---

Monte Carlo simulations of fast-ion confinement in stellarators

Modelling, theory and experimental validation of neutral-beam current drive in TJ-II and evaluation of prompt losses in helias configurations

By

Sadig Mulas Gassim al Seed

Universidad complutense de Madrid
Facultad de Ciencias Físicas
Programa de doctorado en ciencias Físicas

Director: Álvaro Cappa Ascasíbar
Tutor: Luis Ignacio Dinis Vizcaíno

March 2023

GOBIERNO DE ESPAÑA
MINISTERIO DE CIENCIA E INNOVACIÓN
Laboratorio Nacional de Fusión
Ciemat
Infraestructuras Científicas y Técnicas Singulares
UNIÓN EUROPEA
Fondo Europeo de Desarrollo Regional

To my grandparents.

“*MEN WANTED: for hazardous journey, small wages, bitter cold, long months of complete darkness, constant danger, safe return doubtful, honor and recognition in case of success*”

Ernest Shackleton, 4 Burlington st.

Acknowledgements

And here it comes the most important part of the thesis (and probably the most interesting to many). I have just read that the word *acknowledgement* is made of the Old and Middle English words for discover and recognize, now I realize that this work has much of both.

First, I want to thank my (adoptive) supervisor, Álvaro, for guiding and centered me through the messy and wide field of fusion. I will always be grateful not only for the bunch of things I have discovered but also for the colleague and friend that you have been to me during these years. You will always have my recognition as a profesional and a friend, I hope I have been up to you.

Certainly, I must write something to the "ASCOTers near and far", specially to Taina and Joona, who were there almost since the beginning. Apart from inviting me to spend a few weeks in Finland and providing me with the code this thesis is based on, you have been a week-by-week source of expertise in the fast-particle field. Your willing to help and your efforts for keeping the ASCOT community tight and up to date is what the fusion field needs. I hope this thesis is useful for the current and future members of the group.

Additionally, I have to be grateful to the BSC colleagues (Mervi, Edgar, Nacho and the rest of the team) for being welcoming in my stays in Barcelona and their help with Marenostrum. The visit to such impressive and beautiful computing infrastructure has been one of the highlights during this time.

I would like to thank the theory group, of which I have been a member, for their will to help when needed and for the trust they placed on me to carry out the fast-particle part of the brand-new stellarator optimization group that has become part of my thesis. I have learnt a lot from you. I must add a special mention to Daniel, who has always found time to make extra work and discuss with Álvaro and me about my research. Daniel, JL, Edi, Iván (the rest go in another paragraph), you all are part of this thesis!

It would not be fair not to include in these lines those that have contributed to this work from behind: the TJ-II team. Thanks to all the members of the operation/experimental groups that keep this naughty and whimsical device running. Particularly, I have to thank Macarena (ex-leader of the NBI group) for the many details about the NBI that only expertise can reveal and that theoreticians usually skip.

Now, it is time for the magnificent, singular and fun building 20F and its inhabitants. This place has felt almost home (a humble one, though) during these years not only for the long hours spent here but also because its people have been my family here. There are so many names that deserve a place in these lines for the importance that they have had during this time. Nerea, Jose, Antonio, Manolis, Javi, Igor, Pedro, Dhaval, Raúl, Jaime, Guillermo (and, of course, all the rest) thank you for the laughs, the psicological cabinet we all have needed (and still need) from time to time, the semanthic (i.e. stupid) endless debates (being economics, physics, maths, cooking, The Silmarillion, religion and politics the hot topics) and the many coffees/teas/neverending-breakfasts beside you. I don't exagerate saying that if I have reached till this point, it is also your merit. Besides all its lacks (or maybe because of them), this building has made us stronger and better people as well as (unique and more precise) profesionals. I will never forget the support and the experiences in and out of the building with you.

Moving out of CIEMAT, I want to thank my flatmates for making my life easier and happier (at least most of them), especially to Rosana and Ana for the unbeatable organized team we made during the hard lockdown due to the pandemic in a dark flat of Gran vía. Also to Tere, who has stood my complains and thoughts during these last months of hard work.

I feel that the point at which I am currently is the summit of many more years than those of the PhD. It has been a long journey through the University, master and previous jobs in research. That is the reason why I am forced to mention my "VeCiNiTos" and Sergio, Emilio, Yasin and Lucía (and all my friends from Melilla). You guys arrived when it all started, a few even earlier, in Granada and are still here. Thank you so much for listening (everybody knows that you didn't pay attention, though) my freak ideas and (always unrequested) physics lessons and the infinite number of experiences and memories, through thick and thin, in all these years. You are my second family (now in the distance) and somehow you have definitely also pushed me to this point. Thank you!

Lastly, I must show gratitude to my family for being the spring that bounces me back up when I fall. In particular, to my parents and their "bueno, haz lo que quieras" that has always served me as a drive to follow my path fearlessly (although they would prefer that I become a well-paid radiophysicist, we'll see what happens). Also to my brother, who transfers me the peacefulness and discipline he irradiates, and my sister, who disperses my mental storms when we are together. To my uncles, aunts and cousins, who make me feel that nothing has changed despite the time and distance. Finally, and above all, I have to kneel before my grandparents. For giving me everything and continuing teaching me so much even without being here. Now, the lessons you planted in me long ago start to sprout and I know that without them I would not be writing these lines. This thesis is the result of your wishes for me when I said goodbye before leaving in a train or plane: good luck and hard work. I will always feel grateful to you, knowing that you would be more proud of this work than I am. I will always carry your wisdom in the many train stations to come.

Table of Contents

Summary

During the last two decades, the theoretical developments regarding neoclassical transport in stellarators have enhanced the interest in many aspects of the fast-ion physics in these devices. This work is devoted to the study of the dynamics of fast ions and to the validation of fast-ion modelling codes in stellarators, which is fundamental when it comes to interpreting experimental data and making preliminary predictions before the realization of the experiments.

A detailed analysis of the calculated fast-ion distribution function has been performed by means of the orbit-following Monte Carlo code ASCOT5 in different plasma scenarios of the TJ-II stellarator. This distribution function is used to carry out the calculation and validation of the electric current driven by the injection of neutral beams, usually employed for plasma heating. The neutral-beam injection (NBI) system of TJ-II has been simulated with the module of ASCOT5 beamlet-based neutral-beam injection (BBNBI). This Monte Carlo code takes the operational parameters and the geometry of the neutral-beam injectors and simulates the flight of the neutral particles towards the plasma as well as their ionization process within it. ASCOT5, taking the fast ions generated with BBNBI, the magnetic configuration, the plasma profiles and a model of the first wall of TJ-II, solves the Fokker-Planck equation of the fast-ion distribution function with a Monte Carlo method following the trajectories of the fast ions along the magnetic field and simulating the energy transfer to the plasma (slowing-down). The calculated fast-ion distribution function is then used to compute the neutral-beam current drive (NBCD), which has two contributions: the current carried by the fast ions and the response of the plasma electrons to this current. The former is calculated from the parallel velocity moment of the distribution function, while the latter is derived by solving analytically the drift-kinetic equation (DKE) for the plasma electrons at low collisionality. Together with the estimates of NBCD, results of the shine-through, deposited power, and fast-ion density are also presented for high-density TJ-II plasmas.

Next, the computational results of the shine-through fraction and NBCD have been validated against experimental values gathered in selected plasma scenarios with both co- and counter injectors separately. Measurements of the shine-through fraction, obtained with thermographic imaging, and of the toroidal plasma current, measured with a Rogowski coil, have been compared to the estimates of BBNBI and NBCD, respectively. For the validation of the NBCD, we need to account for the contribution of the bootstrap current to the toroidal current, which is calculated with the code DKES. The comparison of the shine-through fractions shows agreement between simulations and experiments for both injectors, while the comparison of the calculated toroidal plasma current and the measured one shows agreement only for the counter-injector case. The possible causes of the discrepancy observed for the co-injection cases are discussed.

Taking advantage of the expertise acquired with ASCOT5, a validation of a new model (Γ_α) for a fast evaluation of the fraction of prompt losses in stellarators was carried out for different magnetic configurations of the Wendelstein 7-X stellarator (W7-X). This has allowed to include it in the stellarator optimization suite of codes STELLOPT. The prediction of the Γ_α model has been tested with ASCOT5 by following the orbits of a population of fast ions uniformly distributed in phase space in several magnetic configurations of the W7-X. The fraction of lost ions at $t = 1$ ms has been compared with the values given by Γ_α showing quantitative agreement between the two methods. This study has also demonstrated the better performance of Γ_α against other models, such as Γ_c, that are used extensively in stellarator optimization suites.

Lastly, the fast-ion loss fraction of a new quasi-isodynamic configuration optimized for fast-ion confinement, obtained with STELLOPT, has been assessed following the same techniques. The results show a very good confinement of fast ions at $\beta = 1.5\%$ that becomes excellent at $\beta = 4\%$. During a second phase of the optimization process, a set of coils was designed for the new configuration. Despite the fact that a degradation of the confinement was expected in this more realistic situation, the loss fraction given by ASCOT5 indicates that the configuration has preserved the good confinement of fast ions at the plasma core.

List of publications

I: "ASCOT5 simulations of neutral-beam heating and current drive in the TJ-II stellarator"
S. Mulas, Á. Cappa et al, Nucl. Fusion **62** 106008 (2022)

II: "A model for the fast evaluation of prompt losses of energetic ions in stellarators"
J.L. Velasco, I. Calvo, S. Mulas, E. Sánchez, F. I. Parra, Á. Cappa and W7-X Team
Nucl. Fusion **61** 116059 (2021)

III: "Validating neutral-beam current drive simulations in the TJ-II stellarator"
S. Mulas, Á. Cappa et al, https://arxiv.org/abs/2301.03488 (Accepted in Nuclear Fusion)

IV: "A quasi-isodynamic configuration with good confinement of fast ions at low plasma β"
E. Sánchez, J. L. Velasco, I. Calvo and S. Mulas, https://doi.org/10.48550/arXiv.2212.01143
(Accepted in Nuclear Fusion)

Other publications and works:

"Stability analysis of TJ-II stellarator NBI driven Alfvén eigenmodes in ECRH and ECCD experiments"
Á. Cappa et al, Nucl. Fusion **61** 066019 (2021)

"On the interplay between turbulent forces and neoclassical particle losses in zonal flow dynamics"
R. Gerrú et al, Nucl. Fusion **59** 106054 (2019)

"Overview of recent TJ-II stellarator results"
E. Ascasíbar et al, Nucl. Fusion **59** 112019 (2019)

"Overview of the TJ-II stellarator research programme towards model validation in fusion plasmas"
C. Hidalgo et al, Nucl. Fusion **62** 042025 (2022)

Contributions to conferences:

"Estimation of Neutral Beam Current Drive in TJ-II" (main author)
22nd International Stellarator and Heliotron Workshop (ISHW 2019)

"Experimental validation of neutral beam current drive simulations in TJ-II plasmas" (main author)
28th IAEA Fusion Energy Conference (FEC 2020)

"Simulations of neutral beam injection in TJ-II stellarator using the Monte Carlo code ASCOT" (main author)
1st Spanish Fusion HPC Workshop

“NBI-driven shear Alfvén waves in the presence of ECR heating and EC driven current in the TJ-II stellarator”
28th IAEA Fusion Energy Conference (FEC 2020)

“Stellarator Fast Ion Physics in Wendelstein 7-X”
23rd International Stellarator and Heliotron Workshop (ISHW 2022)

“Theoretical prediction of improved energetic ion confinement in low-β Wendelstein 7-X plasmas with reduced turbulence”
23rd International Stellarator and Heliotron Workshop (ISHW 2022)

“KNOSOS, a fast neoclassical code for the optimization of three-dimensional geometries”
19th European Fusion Theory Conference (EFTC 2021)

“Impact of ECCD on fast ion driven modes in stellarators (HJ, LHD, TJ-II) and contribution to ITPA-EP activities”
19th Coordinated Working Group Meeting

Preface

One of the greatest challenges of society is the chase for clean and sustainable energy sources. The anthropogenic emissions of greenhouse gases (GHG) since the industrial revolution, mainly due to the use of fossil fuels, have produced an increase of the global temperatures of 1°C, which drives the appearance of extreme climatic events (storms, droughts, floods, etc) that can have serious ecological and social effects for the forthcoming generations. The common strategy adopted by countries concerned with the situation is the substitution of GHG-emitting energy sources by cleaner ones, to avoid or reduce the increase of the global temperatures. To date, the best candidates for this task have been renewable energy sources (mainly solar, wind and hydro) and nuclear. However, the lack of an energy storage makes that the inherent intermittency of the former ones is a major drawback for overlapping the continously-increasing energy demand of society with the energy production. Although, in principle, the stable energy production of nuclear fission might act as a support for renewables, its use has been a matter of debate due to problems such as its real costs, the management of radioactive waste, the potentially harmful ecological damage in case of accidents or the development of nuclear weapons using the same facilities that process nuclear fuel. However, the high energy density of nuclear fission keeps it operating for the energy mix of most of the countries. The little sister of nuclear energies, nuclear fusion, could have many the best of both worlds. Contrary to nuclear fission, where the energy output is obtained from the mass deffect between the reactants and the products ($E = \Delta mc^2$) created when splitting heavy atoms, fusion energy is released (also from mass deffect) when two light atoms fuse (see figure 1(a)). Compared to renewables, fusion energy can be thought as the origin of all of them, since the Sun (and all stars) are huge fusion reactors whose energy drives the majority of the processes on Earth, from ocean flows to photosynthesis. Therefore, with the development of a fusion reactor we would have an on-demand energy source with a high-energy density. The advantages of nuclear fusion with respect to fission are clear: unlike fission products, fusion ones are not radioactive; the technology can not be used with military purposes and the effect that a total accident would have in the ecosystem is almost inexistent. This makes fusion a true candidate as an alternative energy source. Nevertheless, despite fusion itself does not generate nuclear waste, the elements of the first wall of the reactor become radioactive under neutron impacts and they must be treated as short-life radioactive materials, as well as other elements of the device that contain tritium. Nonetheless, fusion presents a huge technological and scientific challenge. Since the 1950s, several laboratories around the globe have gathered efforts to develop a fusion nuclear reactor but the extreme and complex conditions needed to create a continuous source of fusion reactions makes the progress in this field a long-haul task [1]. In order to fuse two nuclei, their thermal energy must overcome the Coulomb force at distances of the order of the nucleus size, which makes nuclear fusion occur at such high temperatures ($\sim 10^9$ K) that the nuclei and the electrons are decoupled from each other in a state of plasma. Because of these high temperatures, constructing a material envelope to keep the plasma inside and withstand the large particle and energy fluxes is a challenging task. In stars, the thermal expansion of the plasma is balanced by the great gravitational force of the star. However, in a prospective reactor, the plasma can not touch the plasma-facing wall of the device or it would melt. One method to tame the plasma is making use of magnetic fields. The charged particles of the plasma follow the magnetic field lines, which confines them to a great extent and paves the path to obtain a controlled fusion-producing system provided that high densities and temperatures are achieved.

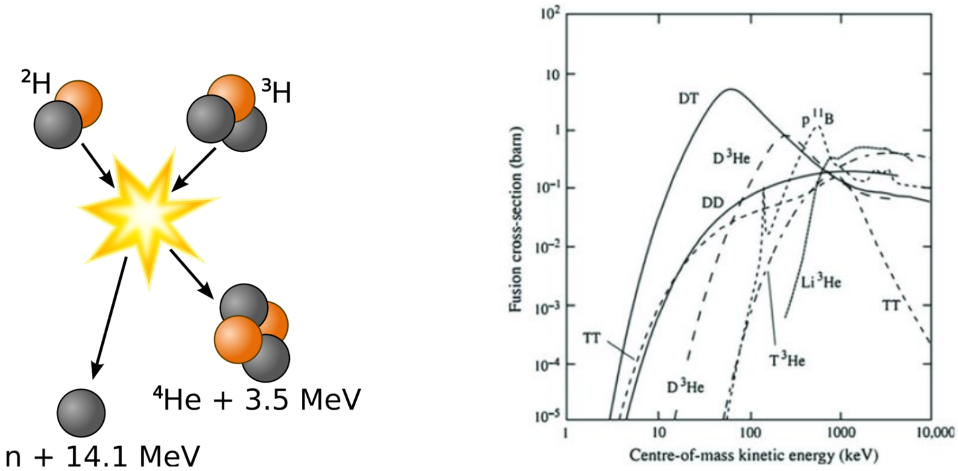

(a) **(b)**

Figure 1: (a) Schematic DT fusion reaction. (b) Cross section of different fusion reactions as a function of the center-of-mass energy of the collision . The DT reaction presents its maximum cross section at lowest energies compared to other reactions, what makes it very convenient for energy production.

The most accessible fusion reaction (see figure 1b) is $D^+ + T^+ \rightarrow He^{2+}(3.5\text{MeV}) + n^0(14.1\text{MeV})$, where two hydrogen isotopes (deuterium, D^+, and tritium, T^+) fuse to give an alpha particle (He^{2+}) and a neutron (n^0), which carries most of the kinetic energy of the reaction. In a hypothetical magnetic confinement reactor, the energy of the alpha particles will heat the plasma and maintain the fusion reactions while the neutrons will escape and deposit their energy in the blanket modules of the reactor producing heat that later will be transformed in electricity with turbines. Therefore, one of the crucial challenges in this field is the good confinement of the fast alpha particles, so that they leave all their energy in the plasma.

Acronyms

NBI Neutral Beam Injection

BBNBI Beamlet-Based Neutral Beam Injection

NBCD Neutral-Beam Current Drive

DKE Drift Kinetic Equation

ICRH Ion-Cyclotron Resonance Heating

ECRH Electron-Cyclotron Resonance Heating

MHD Magnetohydrodynamics

AE Alfvén Eigenmode

HPC High-Performance Computing

LNF Laboratorio Nacional Fusión

OH Ohmic Heating

FO Full Orbit

GC Guiding Center

CX Charge eXchange

PT Port Through

ST Shine Through

HIBP Heavy-Ion-Beam Probe

NPA Neutral-Particle Analyzer

BS BootStrap (current)

DR Doppler Reflectometer

IRC InfraRed Camera

LCFS Last Closed magnetic Flux Surface

GHG Greenhouse Gases

ECCD Electron-Cyclotron Current Drive

ECE Electron-Cyclotron Emission

FILD Fast-Ion Loss Detector

MSE Motional Stark Effect

Introduction

Ideally, the operation of magnetic-confinement fusion reactors requires that the high-energetic alpha particles, product of the fusion reactions, stay confined the time it takes them to transfer their full energy to the plasma (*slowing-down time*) to keep it hot. In this case the plasma reaches the so-called *ignition* phase. However, the only active experiment prepared to withstand fusion reactions from the nuclear safety point of view is the JET tokamak, while the rest of the operational devices are devoted to study the physics of fusion plasmas. Therefore, the study of fast ions in fusion plasmas is not only restricted to fusion alphas in reactors, since they are used, for instance, to heat the plasmas in fusion experiments. The most common sources of fast ions in experiments (usually protons and deuterons) are neutral-beam injection (NBI) and ion-cyclotron resonance heating (ICRH). The first one consists in injecting into the plasma a beam of high-energetic neutral particles that, after getting ionized, leave their energy in the plasma through collisions. The second method is based on coupling to the plasma an electromagnetic wave that oscillates at the cyclotron frequency of the thermal ions. The cyclotron motion of these ions resonates with the wave and increase their energy, which will be transferred later to the rest of the plasma via collisions.

In addition to heating, fast ions can be used as knobs in plasma operation. For instance, in steady-state scenarios in tokamaks, the current driven by the injection of the neutral beam, inherent to NBI, is used to generate the stationary current that creates the poloidal magnetic field needed for confinement.

In stellarator experiments, where a source of plasma current is not strictly needed for confinement, NBI or ICRH are currently used for heating. As in the case of tokamaks, the presence of NBI fast ions generates currents that modify the vacuum magnetic-field configuration, which might cause undesirable effects in the plasma performance. Moreover, the modification of the magnetic structure can open the way to the existence of unstable magnetohydrodynamic (MHD) modes that could deteriorate the confinement. Despite their undesired effects, fast ions can be also beneficial for stellarators. Another always-present undesired source of current in stellarators is bootstrap current [2], which is created by the neoclassical parallel transport of the thermal plasma species. This current could be compensated with NBCD in search for current-free scenarios.

In the case of the TJ-II stellarator, NBI injection is needed to achieve high-density plasmas. In this device, in non-balanced NBI operation, the NBCD is high enough so as to produced strong modifications of the rotational-transform profile that, as mentioned before, opens the way to the exitation of MHD shear Alfvén eigenmodes (AE). Previous studies of AEs in TJ-II showing the strong change in the AE spectrum were the main motivation to investigate the fast-ion distribution and the NBCD. Since AEs are triggered by fast ions, the codes that model the dynamics of AEs, e.g. STELLGAP or FAR3D, rely on parameters of the fast-ion population such as its pressure, density or energy distribution. Besides, they also need the rotational-transform profile of the magnetic configuration during plasma operation, which differs from the vacuum one mainly due to NBCD. Until this thesis, no calculations/validations of the amount of NBCD or its profile had been performed in TJ-II.

The calculation and validation of the NBCD has been the final goal of this project. This task is complex and has involved theoretical and computational developments as well as experiments to test the models. First, a deep knowledge of the neutral-beam injector physics, which depends on specific details of the injector geometry and its coupling to the vacuum vessel of TJ-II, is needed in order to understand the role of each of the parameters characterizing the emitted neutral beam. The boundary conditions imposed by TJ-II itself have been decisive for the precise quantification of the injected power or its shine-through fraction. The good agreement between the predicted and calculated shined-through fractions has assured the quality of the results. Secondly, the many different physical phenomena involved in fast-ion studies, such as charge-exchange (CX) processes, motion of particles in non-uniform electromagnetic fields or the kinetic theory that describes the collisions of the fast ions with the thermal plasma, cover many of the different disciplines of magnetic-confinement fusion. Thirdly, all this knowledge needs to be implemented successfully into a code, for which the familiarity at script level, the development of new capabilities, and the high-performance computing (HPC) facilities to run it efficiently, are crucial for succeeding and gather as much information as possible. Lastly, in order to check the model, its predictions have to be validated against experimental measurements. Therefore, it is mandatory to understand how these experiments are designed and performed as well as what information can be acquired from the diversity of plasma diagnostics available.

The structure of this work has been decided on the basis of providing sufficient information so that the reader can follow a thread of reasoning through the many aspects of the previous paragraph and the relationship between them with no intention of being exhaustive with the details.

Chapter one provides a description of the magnetic-field topology needed to confine a plasma and the different realizations that it can present. Chapter two is devoted to the understading of the fundamental equations that govern the motion of the plasma particles in such a field both from a single-particle perspective (Lagrangian dynamics) and from a collective one (kinetic theory). Chapter three presents the relevant features of the TJ-II stellarator, its heating systems and the main diagnostics used to obtain the experimental plasma parameters needed in the simulations. In chapter four, we explain the procedure followed to implement TJ-II NBI into the code ASCOT5 and how this code models the NBI, the fast-ion trajectories and the obtainment of the fast-ion distribution function. Chapter five is a detailed description of the theoretical model that calculates the NBCD in stellarators. The model presented here is valid for the common conditions of fusion plasmas provided that the fast-ion distribution function is known. In chapter six, we present final computational results of the fast-ion distribution function simulated with ASCOT5 and the corresponding NBCD calculated according to the results presented in chapter five, in a wide range of NBI TJ-II plasmas. Chapter seven is aimed at validating the numerical calculation of NBCD in a set of plasma scenarios specifically designed to perform such validation.

Then, in chapter eight, we have taken advantage of the knowledge acquired so far about the capabilities of the ASCOT5 code to validate a new theoretical model for the fast estimation of prompt losses in optimized stellarator configurations, via a model developed at the Theory Unit of Laboratorio Nacional de Fusión (LNF). This new model is aimed at providing a more precise value of such losses in suites of codes used for optimizing stellarators. In addition, results of the evaluation of prompt losses in a new stellarator configuration obtained with the optimization suites is presented. The new configuration is framed in the search for a new and optimized stellarator device for CIEMAT (*Hic sunt dracones!*).

The last chapter, nine, presents the general conclusions and relevance of the results of the thesis in a broader view.

Finally, four appendices are included for a deeper insight of certain topics. The first one details the expressions of the collision operator used in chapter five and defines the quantities on which it depends. The second one describes the motion of the trapped particles in an inhomogeneous magnetic field, giving a more detailed explanation of the fundamental dynamics behind the model presented in chapter eight. The third Appendix describes the method developed recently at LNF to decouple the inductive and non-inductive contributions to the experimental toroidal plasma current. This method is based on the observations showing that the proximity of the plasma to the TJ-II coils produce a coupling between the oscillations in coil currents and the plasma current that hides the expected exponential evolution of the toroidal current when a non-inductive current contribution (for instance NBCD) is created in the plasma. The last Appendix gives a more detailed description of the charge-exchange processes that the fast ions undergo, and its effects on the fast-ion distribution function, both in TJ-II and Wendelstein 7-X (W7-X) stellarators.

1. Magnetic-confinement fusion

The term magnetic confinement refers to the method used to contain a plasma in a volume by means of a magnetic field. In a first approximation, when the charged particles of the plasma feel the magnetic field, they lose one spatial degree of freedom, being the two remaining the direction of the magnetic-field line and a phase angle around it. The particle trajectories describe a helical motion whose axis is the field line, which confines the particle in the direction perpendicular to it. The geometry of a device designed to achieve magnetic confinement is determined by the structure of the magnetic field. Since any magnetic field $\mathbf{B}$ must fulfill the Maxwell's equation $\nabla \cdot \mathbf{B} = 0$, a simple way to create a closed confining region would be bending a solenoidal conductor bringing its ends together to form a toroid. In this chapter, we describe the two existing concepts of toroidal devices used as candidates for magnetic-confinement fusion reactors and we will present the mathematical formalism used to describe their magnetic field structures.

1.1 Magnetic equilibrium

Let us consider a plasma embedded in a magnetic field. The model that describes the macroscopic equilibrium and stability properties of such system is *Magnetohydrodynamics* (MHD) [3]. The momentum-conservation equation in this framework is

$$n\left(\frac{\partial \mathbf{V}}{\partial t} + \mathbf{V} \cdot \nabla \mathbf{V}\right) = -\nabla p + \nabla \cdot \mathbf{\Pi} + \mathbf{J} \times \mathbf{B} \tag{1.1}$$

where n is the plasma density,$\mathbf{V}$ is the plasma-flow velocity, p is the plasma pressure, $\mathbf{\Pi}$ is the viscosity tensor, $\mathbf{J}$ is the plasma current, and $\mathbf{B}$ the magnetic field. If we consider a steady-state ($\partial/\partial t = 0$) and flowless ($\mathbf{V} = 0$) regime, we get the ideal force-balance equation of MHD,

$$\mathbf{J} \times \mathbf{B} = \nabla p, \tag{1.2}$$

where we have assumed that the viscosity is small. From equation (1.2), three important features can be deduced [4]:

- the lines of **J** and **B** lie in surfaces of constant pressure
- these surfaces must be topologically isomorphic to a torus, otherwise the tangent vectorial fields defined on them (**J** and **B**) would vanished in at least one point[1]
- given this toroidal topology, a convenient reference system is $(p,\ \vartheta,\ \varphi)$, being ϑ and φ arbitrary poloidal and toroidal coordinates such that ϑ increases by 2π in a transversal turn around the torus and so does φ in a longitudinal turn.

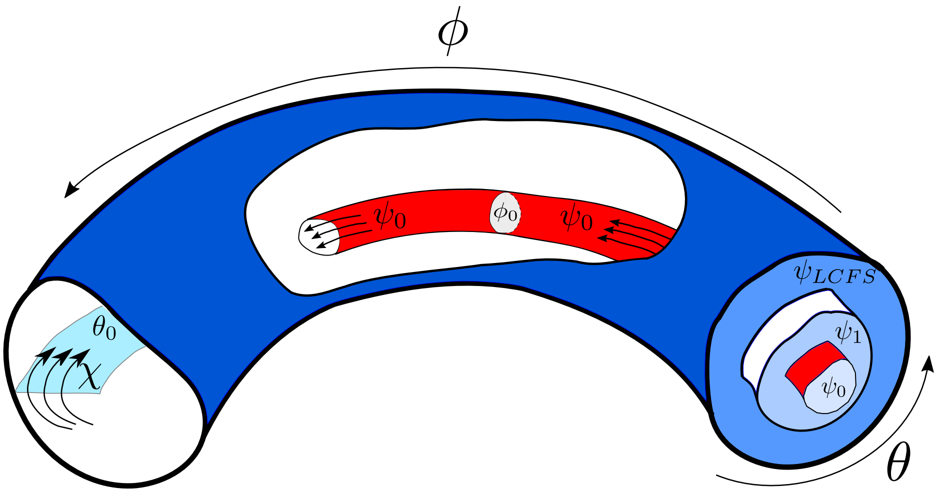

Figure 1.1: Scheme of a general toroidal coordinate system where (ψ, θ, ϕ) are the radial, poloidal and toroidal coordinates, respectively. The nested surfaces are defined such that the toroidal flux (ψ) enclosed within them is constant (red surface). The poloidal flux (χ) is defined as the magnetic flux passing through a surface of constant poloidal angle θ_0.

Let us define the toroidal and poloidal magnetic fluxes passing through constant φ_0 and ϑ_0 surfaces, respectively, as.

$$\psi = \frac{1}{2\pi}\int_{\varphi=\varphi_0} \mathbf{B}\cdot d\mathbf{S}_{\varphi_0}, \tag{1.3}$$

$$\chi = \frac{1}{2\pi}\int_{\vartheta=\vartheta_0} \mathbf{B}\cdot d\mathbf{S}_{\vartheta_0}. \tag{1.4}$$

If the constant pressure surfaces are nested, one can demonstrate that the toroidal flux, ψ, flowing through the contour defined by the intersection of a constant pressure surface

---

[1] This is stated by the so-called Hairy ball theorem.

with a constant φ_0 surface is the same for any φ_0. Thus, the constant pressure surfaces are given the name of *flux surfaces*[2]. In this case, new coordinate systems can be found in which the magnetic field lines are straight, where the new radial, poloidal and toroidal coordinates are $\{\psi, \theta, \phi\}$ (see figure 1.1). Here, $\theta, \phi \in [0, 2\pi)$ are the angular coordinates. The different coordinates systems in which the magnetic field lines are straight are called *magnetic coordinate systems.* In these coordinates [5], the magnetic field can be written as

$$\mathbf{B} = \nabla\psi \times \nabla\theta + \nabla\phi \times \nabla\chi \tag{1.5}$$

A relevant quantity in magnetic confinement is the *rotational transform*, ι, which is defined as

$$\iota = \frac{d\chi}{d\psi}, \tag{1.6}$$

and measures the number of poloidal turns a field line makes per each toroidal turn. Using this definition, equation 1.5 can be expressed in Clebsch's representation as

$$\mathbf{B} = \nabla\psi \times \nabla\alpha, \tag{1.7}$$

with $\alpha = \theta - \iota\phi$. Instead of using the radial coordinate ψ, it is common in the magnetic-fusion community the use of other coordinates such as the normalized magnetic flux, $s = \psi/\psi_{LCFS} \in [0, 1]$, where ψ_{LCFS} is the toroidal magnetic flux at the last closed flux surface (LCFS) of the magnetic configuration, or the normalized plasma radius, defined as $\rho = \sqrt{s}$. The expression of the magnetic field using the radial coordinate s becomes

$$\mathbf{B} = \psi_{LCFS}\nabla s \times \nabla\alpha, \tag{1.8}$$

A commonly used operator in magnetic confinement is the *flux-surface-average operator*, which averages the values of a given function on a fixed flux surface. For a function $h = h(s, \theta, \phi)$ it is defined as

$$\langle h \rangle (s) = \frac{\displaystyle\iint h(s, \theta, \phi)\sqrt{g}\, d\theta d\phi}{\displaystyle\iint \sqrt{g}\, d\theta d\phi} \tag{1.9}$$

where $\sqrt{g}$ is the Jacobian of the metric space.

---

[2] The degenerate flux surface with limiting value of zero flux is called *magnetic axis.*

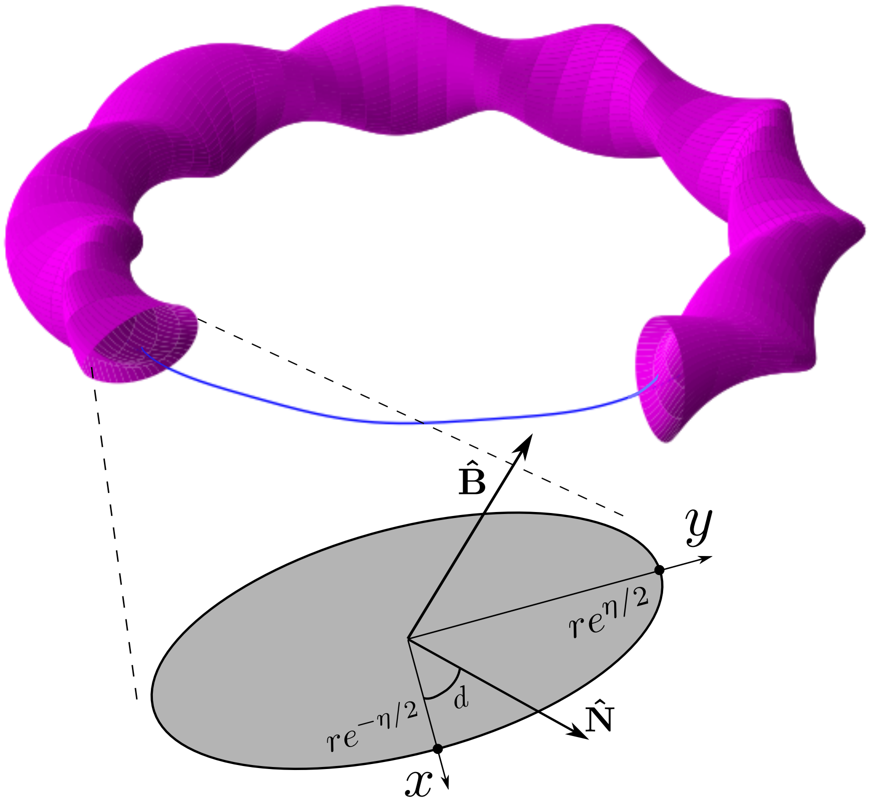

Figure 1.2: Definitions of the quantities appearing in equation (1.10). The vectors $\hat{\mathbf{N}}$ and $\hat{\mathbf{B}}$ are the normal and binormal vectors of the magnetic axis.

As it will be shown in chapter 2, when the magnetic field is inhomogeneous, the trajectories of the particles do not follow exactly the magnetic field lines, but an extra component perpendicular to the field line makes them "drift" away of the confinement region [6]. This effect of the inhomogeneity of the magnetic field can be sorted out if the net outward drift is compensated as the particle travel around the torus, which can be achieved by generating rotational transform in the magnetic field. It can be demonstrated by solving Maxwell's equations $\nabla \cdot \mathbf{B} = 0$ and $\nabla \times \mathbf{B} = \mu_0 \mathbf{J}$ in a region close to the magnetic axis that, for a large aspect ratio torus, the flux-surface cross sections are ellipses and the rotational transform is given by the following expression[3] [4],

$$\iota = \frac{1}{2\pi}\int_0^L \left[\frac{\mu_0 J}{2B_0} - (\cosh\eta - 1)d' - \tau\right]\frac{dl}{\cosh\eta} - N_{fp}, \tag{1.10}$$

where B_0 is the magnetic field in the axis, τ is the torsion of the axis, N_{fp} is the number

---

[3] This definition treats ι as a non-dimensional quantity that other authors name $\iota\!\!\!-$, for whom ι is the *rotational transform angle*, which is the poloidal angle a field line deviates from its starting position after one toroidal turn. We decide to use only ι for simplicity of the notation.

of periods of the configuration and l the distance along the magnetic axis. The quantity η is defined so that the major radius of the ellipse is $re^{\eta/2}$, the minor radius is $re^{-\eta/2}$, being πr^2 the area, and $d(l)$ is the angle between the x-axis of the ellipse and the normal vector of the magnetic axis (see figure 1.2). We can see from equation (1.10) that there are three ways to generate rotational transform:

- with a toroidal plasma current in the direction of the field lines (J)
- rotating the poloidal cross section of the plasma along l (d')
- with the torsion of the magnetic axis (τ)

The decision on how to create the rotational transform defines the two big families of magnetic-confinement devices developed so far: tokamaks and stellarators. In tokamaks, the rotational transform is created exclusively by the plasma current, hence, they are toroidally symmetric, making their design comparatively simpler than that of stellarators. In general, stellarators use a combination of the three methods, which makes them much more complicated conceptually but allows for exploring a much wider range of magnetic configurations. In the next sections, the main features, pros and cons of each type of device are briefly explained.

1.2 Tokamaks

The concept of a Tokamak [7] (after the Russian acronym for Toroidal chamber with magnetic coils) was developed in the mid 1950s in the Soviet Union. The first attempts for creating fusion reactions were based on straight solenoidal fusion devices which accelerated particles to high energies and make them collide onto a deuterium blanket to produce the fusion reactions. The approach of the tokamak design solved the problem of the inefficiency of previous devices by bringing together the ends of the solenoid into a torus. However, the bending of the solenoid causes a gradient of magnetic-field intensity from the outer region of the torus towards the inner region, where the coils are closer to each other, that make particles drift away and leave the device. This deleterious effect was overcome, as explained in the previous section, by inducing a rotational transform of the field (creating a poloidal field) generated solely with an inductive toroidal current produced inside the plasma by an Ohmic transformer (the plasma itself acting as the secondary of the transformer). The axisymmetry of tokamaks have very important benefits, such as inherent high confinement of fast particles and simplicity from the engineering point of

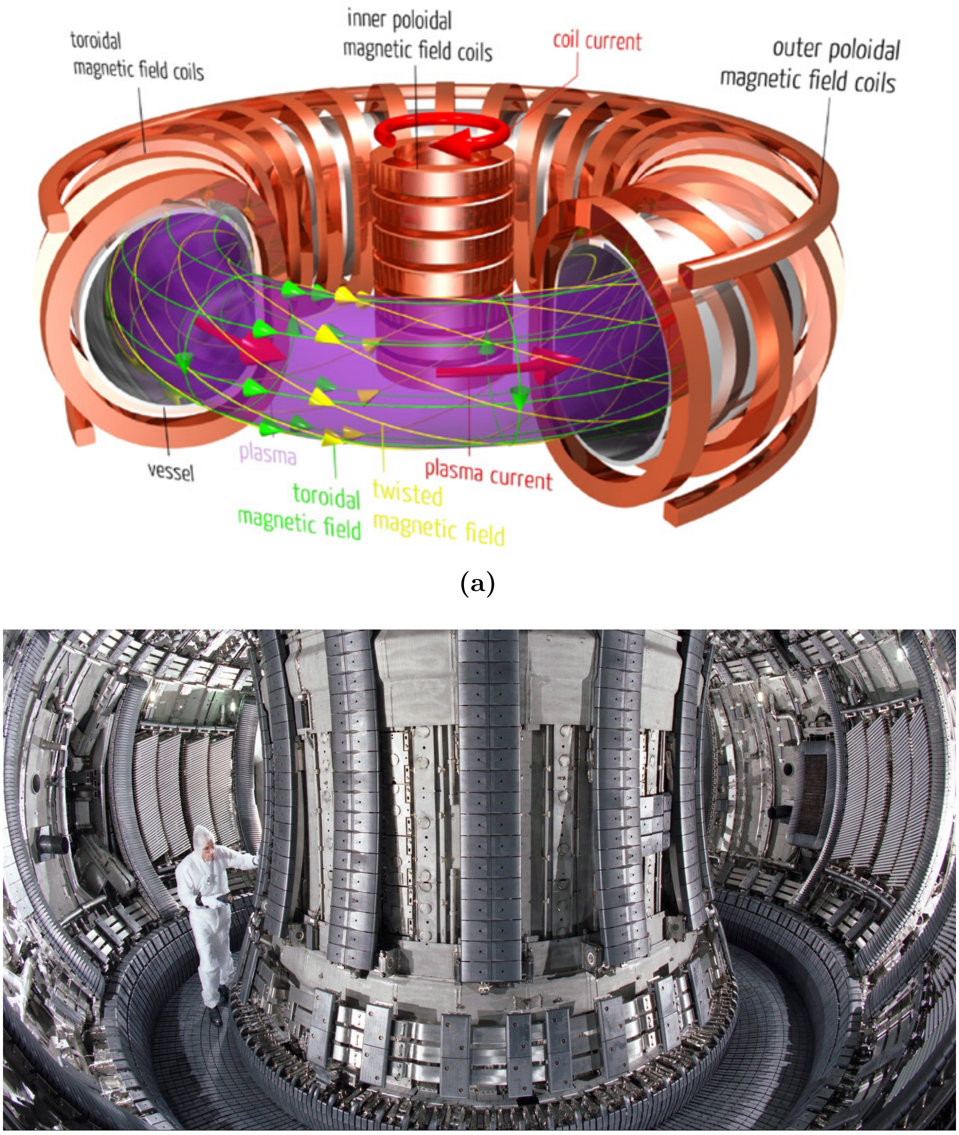

(a)

(b)

Figure 1.3: Schematic drawing of a tokamak design (a) and a picture of the interior of JET (United Kingdom) (b).

view, that make them lead the way for reactor development. Actually, the International Thermonuclear Experimental Reactor (ITER, *the way* in Latin), which will be the first nuclear reactor to demonstrate the scientific viability of fusion as an energy source, will be a tokamak.

Nonetheless, the high amount of current needed to create the poloidal field ($\sim 10^6$A) and its dependence on the plasma parameters can cause destabilization of the magnetic equilibria (*disruptions*), which, in turn, produces a sudden loss of confinement. Thus, the plasma energy is rapidly transferred to the wall and can cause severe damages to the device. In addition, inducing a constant current in the plasma needs a time-varying current in the primary of the transformer, which allows only for an intermittent operation of the device. Many efforts in the scientific side of tokamak research are devoted to mitigate or avoid the disruptions allowing for safe operation, and to investigate steady-state scenarios that do not depend on the OH induced current but on the current induced by external heating and current-drive systems. Figure 1.3 shows a schematic drawing of a tokamak with its main components and an actual picture of the JET tokamak, the largest in operation.

1.3 Stellarators

In parallel to the development of the tokamaks, Lyman Spitzer proposed an alternative way to generate a rotational transform without the need of induced plasma current, using the rotation of the plasma cross section along the toroidal direction or with torsion of the magnetic axis (terms proportional to d' and τ in equation (1.10)).

This solution is based on the design of a 3D magnetic configuration that inherently has a poloidal field component created only with the external coils [8]. There are plenty of different approaches to construct a stellarator depending on the arrangement and shapes of the coils [9] (e.g heliotron, torsatron, heliac, helias, etc), which in general need non-planar shapes that are much more complex than the planar coils of tokamaks. Since stellarators, as opposed to tokamaks, do not rely on any externally created current to build the magnetic field, they naturally allow for a disruptionless operation, which makes them appealing for steady-state operation in a reactor. Figure 1.4 shows the plasma shape and the distribution of coils of the two largest operating stellarators, W7X in Germany and LHD in Japan. The complex 3D internal structure of stellarators is well illustrated in figure 1.5. The main drawback of stellarators, however, is that trapped particles are not naturally confined as they are in tokamaks. The term trapped particle refers to particles that, rather than circulating freely around all the magnetic configuration, are constrained to a small region due to magnetic mirroring (see Appendix D). These particles, in turn, can be confined if their net radial drift is negative or zero (as in tokamaks) or unconfined if it is positive (as in a generic stellarator). This feature is crucial from the reactor point of view, where the trapped fusion-created alphas must remain confined for self-heating efficiency and safety of the reactor.

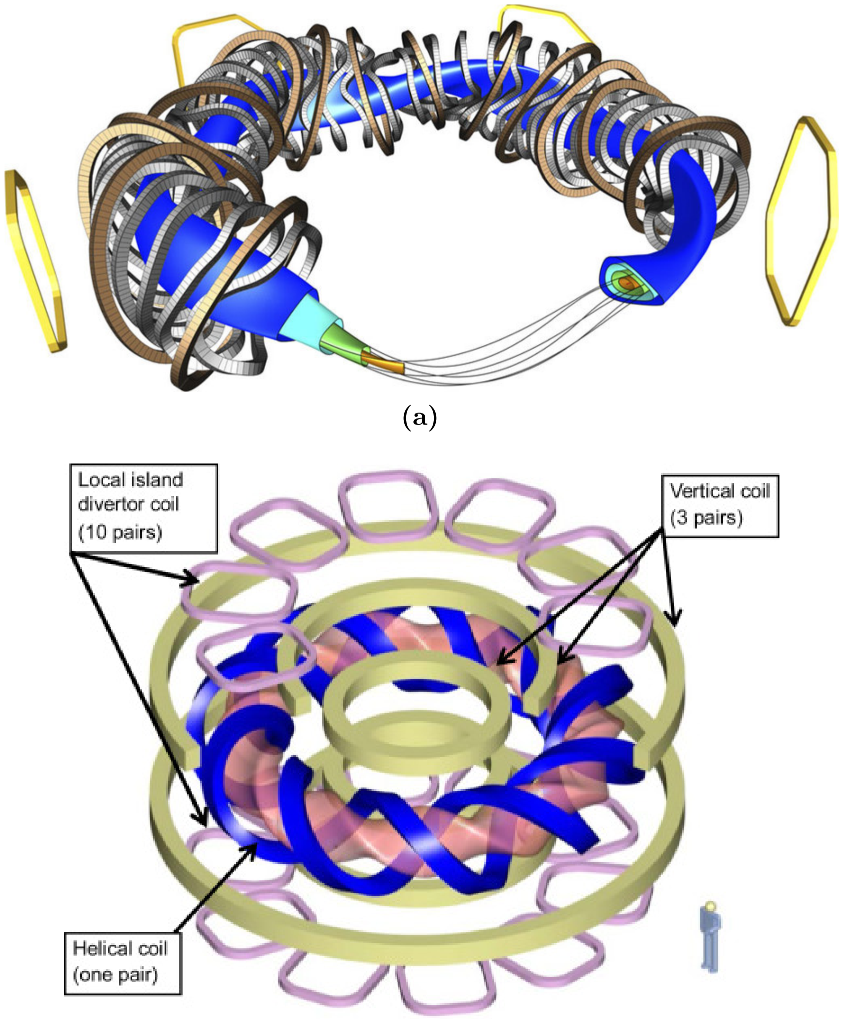

Figure 1.4: (a) Scheme of coil system and flux surfaces of W7-X [10] and, (b) LHD stellarators. The rotational transform in W7-X is created by non-planar coils while in LHD it is created by a set of two helical coils.

Device	**Location**	N_{fp}	**R[m]**	**a[m]**	**B$_0$[T]**
TJ-II	Madrid (Spain)	4	1.5	0.2	1
LHD	Toki (Japan)	10	3.9	0.6	3
HSX	Madison (USA)	4	1.2	0.15	1.4
Heliotron-J	Kyoto (Japan)	4	1.2	0.2	1.5
CNT	Columbia (USA)	2	0.3	0.15	0.2
CTH	Auburn (USA)	2	0.75	0.29	0.7
W7-X	Greifswald (Germany)	5	5.5	0.55	3
SCR-1	Cartago (Costa Rica)	2	0.24	0.05	0.04

Table 1.1: List of operating stellarators and main parameters of the configurations: number of field periods (N_{fp}), major radius (R), minor radius (a) and magnetic field in the axis (B$_0$).

Relatively recent advances in the theory and development of optimized stellarator configurations [11] have paved the way to stellarators with similar, or even better, alpha-particle confinement than tokamaks. The steady-state nature, the absence of disruptions, and the recent results regarding alpha-particle confinement places stellarators as a very promising candidate for fusion reactors. In table 1.1, a list of stellarators in operation at different countries and their configuration parameters are collected.

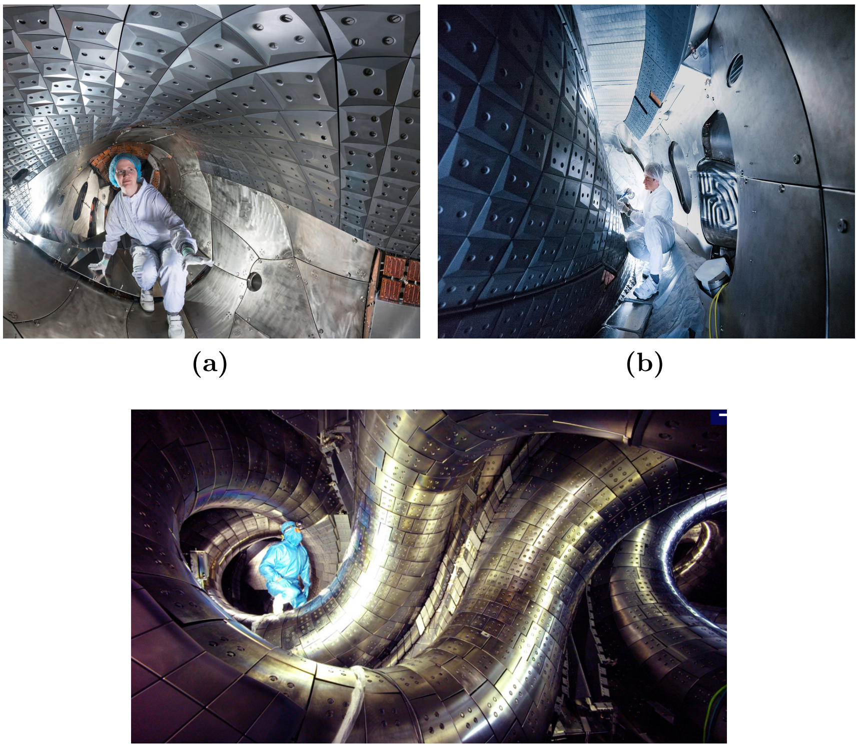

(a)

(b)

(c)

Figure 1.5: Pictures of the interior of W7-X in two toroidal locations, (a) and (b), and of LHD (c). Courtesy of Max-Planck IPP and NIFS.

2. Charged-particle motion in an electromagnetic field

This chapter is devoted to show explicitly the physics that governs the motion of charged particles in a magnetized plasma. We start with the single-particle motion in a general electromagnetic field. Then, we derive the equations of motion of a particle in a static and uniform electromagnetic field, since this result serves as a basis for the discussion of the equations of motion in static non-uniform electromagnetic fields. Later on, the guiding-center formalism will be presented as well as its corresponding equations. Afterwards, we move on from the single-particle treatment to the dynamics of the particles as a collectivity, which is discussed by means of the kinetic theory. Finally, the most common model for the collisions between plasma particles are explained.

2.1 Equations of motion

In order to obtain the equations of motion of a charged particle in a general electromagnetic field, we start from its Lagrangian [12], which is

$$\mathcal{L}(\mathcal{Z},\dot{\mathcal{Z}},t) \equiv \mathcal{L}(\mathbf{r},\mathbf{v},\dot{\mathbf{r}},\dot{\mathbf{v}},t) = [q\mathbf{A}(\mathbf{r},t) + m\mathbf{v}]\cdot\dot{\mathbf{r}} - H(\mathbf{r},\mathbf{v},t), \tag{2.1}$$

where m and q are the mass and charge of the particle, $\mathbf{r}$ and $\mathbf{v}$ are the position and velocity vectors, $\dot{\mathbf{r}}$ and $\dot{\mathbf{v}}$ are their time derivatives, $\mathbf{A}(\mathbf{r},t)$ is the vector potential, $\mathbf{B} = \nabla\times\mathbf{A}$ is the magnetic field, $H = \frac{1}{2}mv^2 + q\phi(\mathbf{r},t)$ is the Hamiltonian, $\phi(\mathbf{r},t)$ is the electric potential and t is the time. The equations of motion are given by the Euler-Lagrange equations [13]

$$\frac{d}{dt}\left(\frac{\partial\mathcal{L}}{\partial\dot{\mathcal{Z}}}\right) - \frac{\partial\mathcal{L}}{\partial\mathcal{Z}} = 0. \tag{2.2}$$

Applying equations (2.2) to the Lagrangian (2.1), we obtain the equations of motion of a charged particle in an electromagnetic field

$$\dot{\mathbf{r}} = \mathbf{v} \tag{2.3}$$

$$\dot{\mathbf{v}} = \frac{q}{m}(\mathbf{E}(\mathbf{r},t) + \mathbf{v} \times \mathbf{B}(\mathbf{r},t)) \tag{2.4}$$

where the electric field is defined as $\mathbf{E} = -\nabla\phi - \dfrac{\partial \mathbf{A}}{\partial t}$.

2.1.1 Particle motion in static and uniform fields

The solution of the particle motion in uniform and static fields can give us a simplified and useful idea of the dynamics of the particle. In this section, we solve the equations (2.3) and (2.4) separating the motions parallel and perpendicular to the magnetic field. With this aim, we project equation (2.4) along and across $\hat{\mathbf{b}}$ to obtain

$$\dot{v}_\parallel = \frac{q}{m}E_\parallel \tag{2.5}$$

$$\dot{\mathbf{v}}_\perp = \frac{q}{m}\mathbf{E}_\perp + \Omega\mathbf{v}_\perp \times \hat{\mathbf{b}} \tag{2.6}$$

where $\hat{\mathbf{b}} = \mathbf{B}/B$ is the unit vector along $\mathbf{B}$, B the magnetic field intensity, $v_\parallel = \mathbf{v}\cdot\hat{\mathbf{b}}$ the parallel velocity, $E_\parallel = \mathbf{E}\cdot\hat{\mathbf{b}}$ the parallel component of the electric field, $\mathbf{v}_\perp = \mathbf{v} - v_\parallel\hat{\mathbf{b}}$ the perpendicular velocity, $\mathbf{E}_\perp = \mathbf{E} - E_\parallel\hat{\mathbf{b}}$ the perpendicular component of the electric field and $\Omega = qB/m$ the *gyrofrequency*. Equation (2.5) can be integrated directly to give

$$v_\parallel = v_{\parallel 0} + \frac{q}{m}E_\parallel t, \tag{2.7}$$

where $v_{\parallel 0}$ is an integration constant. To solve equation (2.6), we substitute the relative velocity $\mathbf{w} = \mathbf{v} - \mathbf{v}_E$ into (2.6), where $\mathbf{v}_E = \mathbf{E}\times\mathbf{B}/B^2$ is known as *E×B-drift*. Thus, equation (2.6) becomes

$$\dot{\mathbf{w}}_\perp - \Omega\mathbf{w}_\perp \times \hat{\mathbf{b}} = 0. \tag{2.8}$$

This is a linear system of differential equations whose solution is found defining an orthonormal basis $\{\hat{\mathbf{e}}_i\}_{i=1,2,3}$ such that $\hat{\mathbf{e}}_3 \equiv \hat{\mathbf{b}} = \hat{\mathbf{e}}_1 \times \hat{\mathbf{e}}_2$. In this basis, the solution is

$$\mathbf{w}_\perp(t) = w_\perp(\cos(\Omega t + \alpha)\hat{\mathbf{e}}_1 - \sin(\Omega t + \alpha)\hat{\mathbf{e}}_2) \tag{2.9}$$

where $w_\perp$ and α are constants. Then, the velocity of the particle is obtained from equations (2.7) and (2.8) as

$$\begin{aligned}\mathbf{v}(t) &= v_\parallel\hat{\mathbf{b}} + \mathbf{v}_\perp \\ &= \left(v_{\parallel 0} + \frac{q}{m}E_\parallel t\right)\hat{\mathbf{b}} + \mathbf{v}_E + w_\perp(\cos(\Omega t + \alpha)\hat{\mathbf{e}}_1 - \sin(\Omega t + \alpha)\hat{\mathbf{e}}_2)\end{aligned} \tag{2.10}$$

and, integrating equation (2.10), we get the trajectory of the particle

$$\mathbf{r}(t) = \mathbf{r}_0 + \left(v_{\parallel 0}t + \frac{q}{2m}E_\parallel t^2\right)\hat{\mathbf{b}} + \mathbf{v}_E t + \rho_L(\sin(\Omega t + \alpha)\hat{\mathbf{e}}_1 + \cos(\Omega t + \alpha)\hat{\mathbf{e}}_2), \tag{2.11}$$

where $\rho_L = w_\perp/\Omega$ is the *Larmor radius* of the particle. The motion that these equations describe is a freely moving particle in the parallel direction (when $E_\parallel = 0$), a constant drift, $\mathbf{v}_E$, across the magnetic-field line and a fast rotation around it with a *gyroradius* ρ_L. It is important to notice that the rotation around the field line, known as *gyromotion*, is the only movement that occurs at a small spatial scale (ρ_L) and in a fast time scale. In the next section, we will take advantage of this fact to rigorously reduce the 6D phase space to a 5D one by expanding, up to a desired order, in the small and fast scales of the gyromotion.

2.1.2 Particle motion in non-uniform fields

Although the motion derived in the previous section is only strictly valid for uniform and time independent fields, it can be extended to fields whose variations are tiny in the time and spatial scales of the gyromotion: Ω^{-1} and ρ_L. If we have a system of size L (normally, in fusion plasmas, this size is chosen to be the plasma minor radius) and a particle with a thermal velocity v_t, we can take as a time scale of the system the time it takes the particle to cover a distance L,

$$\omega^{-1} \sim \left(\frac{L}{v_t}\right). \tag{2.12}$$

Now, let the scales of variation of the fields be

$$\nabla\mathbf{E} \sim \frac{\mathbf{E}}{L}, \qquad \nabla\mathbf{B} \sim \frac{\mathbf{B}}{L}, \qquad \frac{\partial\mathbf{E}}{\partial t} \sim \omega\mathbf{E}, \qquad \frac{\partial\mathbf{B}}{\partial t} \sim \omega\mathbf{B} \tag{2.13}$$

and consider that the plasma is magnetized if the magnetic field is strong enough so that we can define a small parameter ϵ as

$$\epsilon = \frac{\rho_L}{L} \sim \frac{mv_t}{qBL} = \frac{\omega}{\Omega} \ll 1. \tag{2.14}$$

We have to give an approximate value to both the parallel and perpendicular electric fields. Assuming that the parallel potential energy of the particle is comparable to its kinetic energy, the parallel electric field is ordered as

$$E_\parallel \sim \frac{mv_t^2}{qL}. \tag{2.15}$$

Regarding the perpendicular electric field, an upper limit can be chosen so that it compensates the magnetic force, hence

$$\mathbf{E}_\perp \sim v_t B \gg E_\|. \tag{2.16}$$

In these limits, the position and velocity of the particle are ordered as:

$$\mathbf{r}(t) = \underbrace{\mathbf{r}_0}_{\sim L} + \Big(\underbrace{v_{\|0} t}_{\sim v_t t} + \underbrace{\frac{q}{2m} E_\| t^2}_{\sim v_t^2 t^2/L}\Big)\hat{\mathbf{b}} + \underbrace{\mathbf{v}_E t}_{\sim v_t t} + \underbrace{\rho_L(\sin\gamma\hat{\mathbf{e}}_1 + \cos\gamma\hat{\mathbf{e}}_2)}_{\sim \epsilon L} \tag{2.17}$$

$$\mathbf{v}(t) = \Big(\underbrace{v_{\|0}}_{\sim v_t} + \underbrace{\frac{q}{m} E_\| t}_{\sim v_t^2 t/L}\Big)\hat{\mathbf{b}} + \underbrace{\mathbf{v}_E}_{\sim v_t} + \underbrace{w_\perp(\cos\gamma\hat{\mathbf{e}}_1 - \sin\gamma\hat{\mathbf{e}}_2)}_{\sim v_t} \tag{2.18}$$

where $\gamma = \Omega t + \alpha$. Only the fifth term in $\mathbf{r}(t)$ is small and it is dominated by the fast time scale. On the contrary, $\mathbf{v}(t)$ is totally dominated by the fast time scale, because the term in which it appears (fourth) has the same size than the others. In the next section we will see how we can get rid of these small and fast scales.

2.1.3 Guiding-center motion

As we have seen in the previous section, the particle motion has a fast time scale whose associated length scale is small. Thus, in case we want to calculate the trajectories of the particles, we would need to integrate the equations of motion with enough resolution to solve accurately the gyromotion. However, if the electromagnetic field fulfils the orderings (2.14),(2.15),(2.16), we can find a new coordinate system $(\mathbf{R}_g, v_{\|g}, \mu_g, \gamma_g)$ in which the slow time scales can be from the fast one. This is known as guiding-center formalism, where the guiding center (GC) is the center of the particle's helical trajectory around the magnetic-field line (see figure 2.1). In order to obtain the equations of motion of the guiding-center, we present a summary of the much more detailed description developed in [12]. First, we must perform in the Lagrangian (2.1) the coordinate transformation[1] given by

$$\mathbf{r} = \mathbf{R}_g + \epsilon\boldsymbol{\rho}(\mathbf{R}_g, \mu_g, \gamma_g) \tag{2.19}$$

$$\mathbf{v} = v_{\|g}\hat{\mathbf{b}}(\mathbf{R}_g) + \frac{q}{m}\boldsymbol{\rho}(\mathbf{R}_g, \mu_g, \gamma_g) \times \mathbf{B}(\mathbf{R}_g) \tag{2.20}$$

where the gyroradius vector in the new coordiantes is given by

$$\boldsymbol{\rho} = \frac{1}{q}\sqrt{\frac{2m\mu_g}{B(\mathbf{R}_g)}}(\sin\gamma_g\hat{\mathbf{e}}_1(\mathbf{R}_g) + \cos\gamma_g\hat{\mathbf{e}}_2(\mathbf{R}_g)) \tag{2.21}$$

---

[1] The small parameter ϵ is introduced here only to show explicitly the ordering of each of the terms of the equations

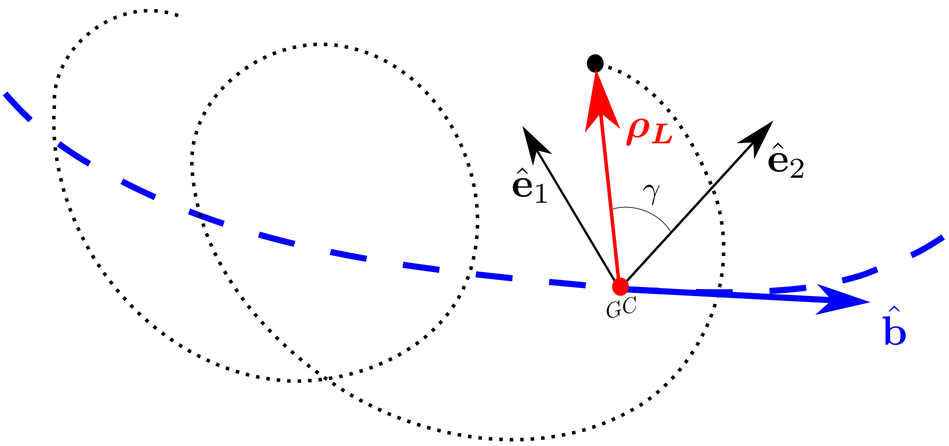

Figure 2.1: Drawing of the orbit followed by a particle around a magnetic field line. The coordinate system solidary with the movement and the gyroradius vector are also represented

Here, $\mathbf{R}_g$ is the guiding-center position, $\mu_g = m\omega_\perp^2/2B$ and γ_g are the magnetic moment and the gyrophase associated to the guiding center, respectively. In these coordinates and for stationary fields, the Lagrangian (2.1), up to first order in ϵ, reads

$$\mathcal{L}_g(\mathbf{R}_g, v_{\|g}, \mu_g, \gamma_g) = \left[\frac{q}{\epsilon}\mathbf{A}_g + mv_{\|g}\hat{\mathbf{b}}_g + \epsilon\boldsymbol{\Gamma}_{\mathbf{r}}^{(1)}\right] \cdot \dot{\mathbf{R}}_g - H^{(0)} - \epsilon H^{(1)}, \tag{2.22}$$

where

$$\begin{aligned} \boldsymbol{\Gamma}_{\mathbf{r}}^{(1)} =& \frac{m\mu_g}{q}\nabla_g\hat{\mathbf{e}}_{2g}\cdot\hat{\mathbf{e}}_{1g} - mv_{\|g}\nabla_g\hat{\mathbf{b}}\cdot\boldsymbol{\rho} - \\ & \frac{q}{2}\left(\boldsymbol{\rho}\cdot\nabla_g B_g\right)\boldsymbol{\rho}\times\hat{\mathbf{b}}_g + \frac{q}{2}\left(\boldsymbol{\rho}\cdot\nabla_g\hat{\mathbf{b}}_g\cdot\left(\boldsymbol{\rho}\times\hat{\mathbf{b}}_g\right)\right)\mathbf{B}_g \end{aligned} \tag{2.23}$$

$$H^{(0)} = \frac{1}{2}mv_{\|g}^2 + \mu_g B_g \tag{2.24}$$

$$H^{(1)} = q\phi_g \tag{2.25}$$

This Lagrangian still depends on ϕ_g but we can relax this dependence, provided that the orderings of the electromagnetic field holds and that we are not interested in the detailed description of the gyromotion, averaging on ϕ_g, which still allow us to see the effects of the finite Larmor radius on average. Thus, defining the gyroaverage operator as

$$\langle\cdots\rangle_\gamma = \frac{1}{2\pi}\int_0^{2\pi}\cdots\, d\gamma \tag{2.26}$$

and applying it to (2.22) we get

$$\langle \mathcal{L}_g(\mathbf{R}_g, v_{\|g,\gamma_g}, \mu_g)\rangle_\gamma \equiv \overline{\mathcal{L}}_g = \left[\frac{q}{\epsilon}\mathbf{A_g} + mv_{\|g}\hat{\mathbf{b}}_g + \epsilon\frac{m\mu_g}{q}\left(-\nabla_g\hat{\mathbf{e}}_{2g}\cdot\hat{\mathbf{e}}_{1g} - \frac{1}{2}\hat{\mathbf{b}}\hat{\mathbf{b}}\cdot\nabla_g\times\hat{\mathbf{b}}\right)\right]\dot{\mathbf{R}} - \frac{m\mu_g}{q}\dot{\gamma}_g - \overline{H} \tag{2.27}$$

with

$$\overline{H} = \frac{1}{2}mv_{\|g}^2 + \mu_g B_g + \epsilon q\phi_g \tag{2.28}$$

The equations of motion for this Lagrangian are given by

$$\dot{\mathbf{R}}_g = v_{\|g}\frac{\mathbf{B}_g^*}{B_{\|g}^*} + \mathbf{E}_g^* \times \frac{\hat{\mathbf{b}}_g}{B_{\|g}^*} + O(\epsilon^2) \tag{2.29}$$

$$\dot{v}_{\|g} = \frac{q}{m}\mathbf{E}_g^*\cdot\frac{\mathbf{B}_g^*}{B_{\|g}^*} + O(\epsilon^2) \tag{2.30}$$

$$\dot{\mu}_g = 0 \tag{2.31}$$

$$\dot{\gamma}_g = \Omega + \dot{\mathbf{R}}_g\cdot\left(-\nabla_g\hat{\mathbf{e}}_{2g}\cdot\hat{\mathbf{e}}_{1g} + \frac{\tau_B}{2}\hat{\mathbf{b}}_g\right) + O(\epsilon^2) \tag{2.32}$$

with

$$\mathbf{B}_g^* = \mathbf{B}_g + \epsilon\frac{mv_{\|g}}{q}\nabla_g\times\hat{\mathbf{b}}_g \tag{2.33}$$

$$\mathbf{E}_g^* = \mathbf{E}_g - \frac{\mu_g}{q}\nabla_g B_g \tag{2.34}$$

$$B_{\|g}^* = \mathbf{B}_g^*\cdot\hat{\mathbf{b}}_g \tag{2.35}$$

2.2 Basics of kinetic theory

The individual charged particles of the plasma move in the electromagnetic field accordingly to the equations presented in section 2.1. However, it is usual that one is interested in the macroscopic properties of a certain kind of particles as a whole [14]. Let the distribution function of some population of particles (*test particles*) be defined as $f(\mathbf{r},\mathbf{v})$ so that $f(\mathbf{r},\mathbf{v})d\mathbf{r}d\mathbf{v}$ is the number of particles[2] in the differential volume element of phase

---

[2] The distribution function can be also thought as a probability distribution. In that scheme, $f(\mathbf{r},\mathbf{v})$ represents the probability of finding a particle in a phase-space volume $(\mathbf{r}+d\mathbf{r},\mathbf{v}+d\mathbf{v})$ and must be normalized to one.

space. The time evolution of that distribution function is given by Boltzmann's equation,

$$\frac{df}{dt} = \frac{\partial f}{\partial t} + \dot{\mathbf{r}}\frac{\partial f}{\partial \mathbf{r}} + \dot{\mathbf{v}}\frac{\partial f}{\partial \mathbf{v}} = \left(\frac{df}{dt}\right)_{coll}, \tag{2.36}$$

where the last term is the contribution to the time evolution due to the collisions. When including the equations of motion for stationary fields, and assuming that we are only interested in the steady state of the system ($\partial f/\partial t = 0$), we get the Fokker-Planck equation

$$\mathbf{v}\frac{\partial f}{\partial \mathbf{r}} + \frac{q}{m}(\mathbf{E} + \mathbf{v} \times \mathbf{B})\frac{\partial f}{\partial \mathbf{v}} = \mathcal{C}(f), \tag{2.37}$$

where

$$\left(\frac{df}{dt}\right)_{coll} \equiv \mathcal{C}(f) \tag{2.38}$$

is the collision operator. The simplification of assuming that the steady steady state has been reached implies that the test particle population does not modify the global system. Otherwise, the solution would be inconsistent. This does not mean that this equation is restricted only to steady-state studies, since its solution can be used to feed transport equations whose results, in turn, can be introduced in equation (2.37), iterating this process until the solution of all the transport equations converge. Although the distribution function is not a measurable magnitude itself, it contains all the information needed to calculate any physical quantity. These are given by the different moments of the distribution function. A few relevant ones are

$$n = \int f(\mathbf{r}, \mathbf{v}) d\mathbf{v}, \tag{2.39}$$

$$\mathbf{V} = \frac{1}{n}\int \mathbf{v} f(\mathbf{r}, \mathbf{v}) d\mathbf{v}, \tag{2.40}$$

$$p = m\int (\mathbf{v} - \mathbf{V})^2 f(\mathbf{r}, \mathbf{v}) d\mathbf{v}, \tag{2.41}$$

which are the density, the average flow and the pressure of the test-particle population. In general, and more particularly in fusion research, because of the complexity of its terms, equation (2.37) can only be solved with numerical methods.

2.2.1 Collision operator

In order to give a complete description of the distribution function (equation (2.37)), we need an expression for its evolution due to the collisions. The main mechanism of interaction between particles in a plasma is the Coulomb interaction. In a neutral gas, the collisions between particles change their initial velocity vectors drastically, which makes particles performed cracked trajectories similarly to pool balls. However, the charged particles in a plasma undergo small and smooth deviations due to the long-range Coulomb interaction. To model this interaction, we will define $F(\mathbf{v}, \Delta\mathbf{v})$ as the probability of a particle to change its velocity from $\mathbf{v}$ to $\mathbf{v} + \Delta\mathbf{v}$ in a time Δt, provided that

$$\int F(\mathbf{v}, \Delta\mathbf{v}) d\Delta\mathbf{v} = 1. \tag{2.42}$$

Then, the distribution function changes as

$$f(\mathbf{r}, \mathbf{v}, t + \Delta t) = \int f(\mathbf{r}, \mathbf{v} - \Delta\mathbf{v}, t) F(\mathbf{v} - \Delta\mathbf{v}, \Delta\mathbf{v}) d\Delta\mathbf{v}. \tag{2.43}$$

Assuming that $|\Delta\mathbf{v}| \ll |\mathbf{v}|$, we can expand equation (2.43) obtaining

$$\begin{aligned} f(\mathbf{r}, \mathbf{v}, t + \Delta t) = \int \Big(& f(\mathbf{r}, \mathbf{v}, t) F(\mathbf{v}, \Delta\mathbf{v}) - \nabla_v (f(\mathbf{r}, \mathbf{v}, t) F(\mathbf{v}, \Delta\mathbf{v})) \cdot \Delta\mathbf{v} \\ & + \nabla_v \nabla_v (f(\mathbf{r}, \mathbf{v}, t) F(\mathbf{v}, \Delta\mathbf{v})) \colon \frac{\Delta\mathbf{v}\Delta\mathbf{v}}{2} - O(\Delta\mathbf{v}\Delta\mathbf{v}\Delta\mathbf{v}) \Big) d\Delta\mathbf{v}, \end{aligned} \tag{2.44}$$

which can be reduced to

$$\begin{aligned} f(\mathbf{r}, \mathbf{v}, t + \Delta t) = & f(\mathbf{r}, \mathbf{v}, t) - \nabla_v \cdot (f(\mathbf{r}, \mathbf{v}, t) \langle \Delta\mathbf{v} \rangle) \\ & + \nabla_v \cdot \nabla_v \cdot \left(f(\mathbf{r}, \mathbf{v}, t) \frac{\langle \Delta\mathbf{v}\Delta\mathbf{v} \rangle}{2} \right) \end{aligned} \tag{2.45}$$

where we have excluded terms of order higher than 2 and defined the average values of $\Delta\mathbf{v}$ and $\Delta\mathbf{v}\Delta\mathbf{v}$ as

$$\langle \Delta\mathbf{v} \rangle = \int \Delta\mathbf{v} F(\mathbf{v}, \Delta\mathbf{v}) d\Delta\mathbf{v} \tag{2.46}$$

$$\langle \Delta\mathbf{v}\Delta\mathbf{v} \rangle = \int \Delta\mathbf{v}\Delta\mathbf{v} F(\mathbf{v}, \Delta\mathbf{v}) d\Delta\mathbf{v}. \tag{2.47}$$

Now, we can present the expression for the collision operator

$$\begin{aligned} \mathcal{C}(f) \equiv & \lim_{\Delta t \to 0} \frac{f(\mathbf{r}, \mathbf{v}, t + \Delta t) - f(\mathbf{r}, \mathbf{v}, t)}{\Delta t} \\ & = -\nabla_v \cdot (\mathbf{F} f(\mathbf{r}, \mathbf{v}, t)) + \nabla_v \cdot \nabla_v \cdot (\mathbf{D} f(\mathbf{r}, \mathbf{v}, t)) . \end{aligned} \tag{2.48}$$

The first term of equation 2.48 produces a friction (average change in velocity), while the second one a diffusion. The friction coefficient ($\mathbf{F}$) and the diffusion tensor ($\mathbf{D}$) are defined as

$$\mathbf{F} = \lim_{\Delta t \to 0} \frac{\langle \Delta \mathbf{v} \rangle}{\Delta t} \tag{2.49}$$

$$\mathbf{D} = \lim_{\Delta t \to 0} \frac{\langle \Delta \mathbf{v} \Delta \mathbf{v} \rangle}{2\Delta t}. \tag{2.50}$$

The derivation of the explicit form of $\mathbf{F}$ and $\mathbf{D}$ for Coulomb collisions of particle species a against species b can be found in [14]. These expressions are given by

$$\mathbf{F_a} \equiv \sum_b \mathbf{F}_{ab} = -\sum_b \frac{c_{ab}}{m_a^2} \left(1 + \frac{m_a}{m_b}\right) \int f_b(\mathbf{v}') \frac{\mathbf{u}}{u^3} d\mathbf{v}' \tag{2.51}$$

$$\mathbf{D_a} \equiv \sum_b \mathbf{D}_{ab} = \frac{1}{2} \sum_b \frac{c_{ab}}{m_a^2} \int f_b(\mathbf{v}') \left(\frac{\mathbf{I}}{u} - \frac{\mathbf{uu}}{u^3}\right) d\mathbf{v}'. \tag{2.52}$$

where m_a and m_b are the masses of species a and b, $c_{ab} = q_a^2 q_b^2 \ln\Lambda_{ab}/\epsilon_0$, q_a and q_b are the charges of species a and b, $\ln\Lambda$ is the Coulomb logarithm (defined in Appendix A), f_b is the distribution function of species b, and $\mathbf{u} = \mathbf{v} - \mathbf{v}'$.

If particle species b are in thermodynamic equilibrium, as in the case of the thermal plasma, its distribution function is a Maxwellian given by

$$f_{Mb}(v) = n_b \left(\frac{m_b}{2\pi T_b}\right)^{3/2} \exp\left(\frac{-mv^2}{2T_b}\right). \tag{2.53}$$

In this case, equation 2.51 and 2.52 become

$$\mathbf{F_a} \equiv \sum_b \mathbf{F}_{ab} = -\sum_b \left(1 + \frac{m_b}{m_a}\right) \nu_{ab} \mathbf{v} \tag{2.54}$$

$$\mathbf{D_a} \equiv \sum_b \mathbf{D}_{ab} = D_{\parallel,ab} \frac{\mathbf{vv}}{u^2} + D_{\perp,ab} \left(\mathbf{I} - \frac{\mathbf{vv}}{v^2}\right). \tag{2.55}$$

with the scalar fiction and diffusion coefficients are given by

$$\nu_{ab}(v) = \frac{n_b c_{ab}}{m_a m_b v_b^2} \frac{G(v/v_b)}{v} \tag{2.56}$$

$$D_{\parallel,ab}(v) = \frac{n_b c_{ab}}{2 m_a^2 v} G(v/v_b) \tag{2.57}$$

$$D_{\perp,ab}(v) = \frac{n_b c_{ab}}{2 m_a^2 v} \left(\text{erf}(v/v_b) - \frac{1}{2} G(v/v_b)\right), \tag{2.58}$$

where $v_b = \sqrt{2T_b/m_b}$ is the thermal velocity of species b, $\mathrm{erf}(x) = 2\pi^{-1/2}\int_0^x \exp(-\xi^2)d\xi$ is the error function, and the Chandrasekhar function, $G(x)$, is given by

$$G(x) = \frac{\mathrm{erf}(x) - \dfrac{2x}{\sqrt{\pi}}\exp(-x^2)}{x^2}. \tag{2.59}$$

2.2.2 Langevin equations

A common way of solving the Fokker-Planck equation is recurring to the Langevin approach, which can be divided in three steps. Firstly, following the methods of statistical mechanics, one can demonstrate (see [15]) that the trajectories of the individual particles whose distribution function is the solution of the Fokker-Planck equation are given by its associated Langevin (stochastic) equations. This is, for a given Fokker-Planck equation, such as (2.37), these trajectories are given by:

$$d\mathbf{r} = \left(\mathbf{v} + \frac{q}{m}(\mathbf{E} + \mathbf{v}\times\mathbf{B})\right)dt, \tag{2.60}$$

$$d\mathbf{v} = \mathbf{F}dt + \left(\sqrt{2D_\parallel}\hat{\mathbf{v}}\hat{\mathbf{v}} + \sqrt{2D_\perp}(\mathbf{I} - \hat{\mathbf{v}}\hat{\mathbf{v}})\right)\cdot d\boldsymbol{\mathcal{W}}. \tag{2.61}$$

Here, the term $d\boldsymbol{\mathcal{W}}$ is the Wiener process (see [15]), which carries all the stochastic dependence of the equation. Equation (2.60) is fully deterministic and describes the trajectories of the particles. Equation (2.61), which describes the evolution of the velocity vector of the particles, presents two terms: the first is deterministic and represents the drag or friction against the plasma, the second one is stochastic and models the diffusion in velocity space. The distribution function, $f(\mathbf{r},\mathbf{v})$ can be calculated evolving the Langevin equations (orbit-following) and reconstructing $f(\mathbf{r},\mathbf{v})$ statistically from the trajectories of the particles in phase space at every time step.

These equations determine the movement of the particles that we will simulate in the following chapters. Equations (2.60) and (2.61) correspond to the case of *full-orbit* trajectories, i.e. without averaging the gyrophase. The derivation of the analogous equations for the guiding-center formalism is out of the scope of this work, because all the simulations performed have been for the full-orbit (FO) treatment, and we refer to reference [16] for a detailed description of the method to obtain the equations of motion with collisions in the guiding-center approach.

3. TJ-II stellarator: heating systems and diagnostics

The TJ-II stellarator (see figure 3.1) is a four-period flexible heliac ($R = 1.5$ m, $\langle a \rangle \leq 0.22$ m, $B_0 = 0.95$ T) with high rotational transform and low magnetic shear [17]. Magnetic configurations with central values of rotational transform from $\iota\!\!\!-(0) = 0.9$ to $\iota\!\!\!-(0) = 2.2$ are available in the device. Figures 3.2 show two vertical cross-sections at different toroidal angles ϕ and a 2D map of the magnetic field intensity inside the plasma calculated with the VMEC code [18]. In this case ϕ and θ are the angular coordinates as defined in the VMEC code (ϕ is actually the cylindrical coordinate angle). The rotational transform profile is shown in figure 3.3. The values of B and $\iota\!\!\!-$ shown in the figures are the ones corresponding to the so-called standard magnetic configuration. Typical plasma densities

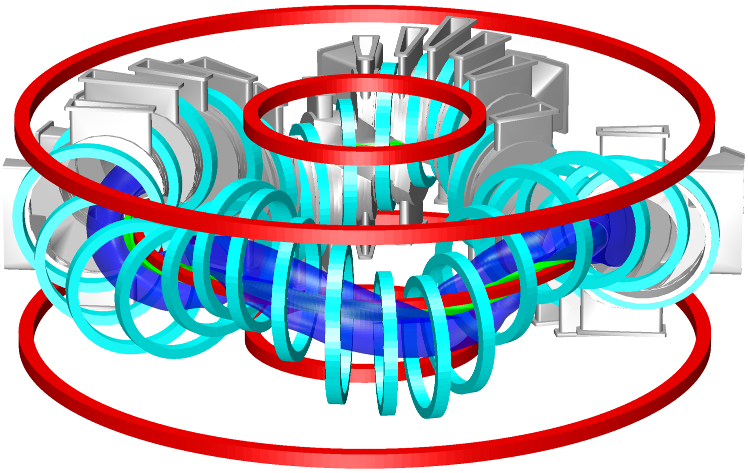

Figure 3.1: TJ-II stellarator. The plasma confined inside the device is shown in dark blue. Magnetic configuration coils (red and cyan) and half vacuum vessel (grey) are also shown.

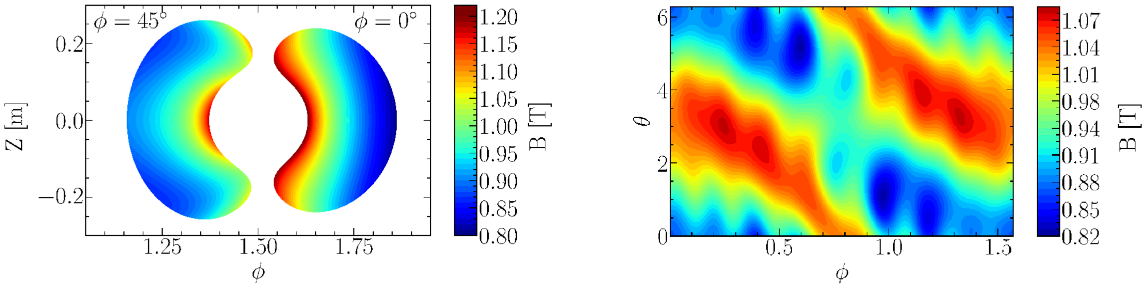

(a) **(b)**

Figure 3.2: (a) Vertical cross sections of the magnetic field intensity at $\phi = 0°$ and $\phi = 45°$, (b) Magnetic field intensity evaluated all over the $\rho = 0.46$ flux surface.

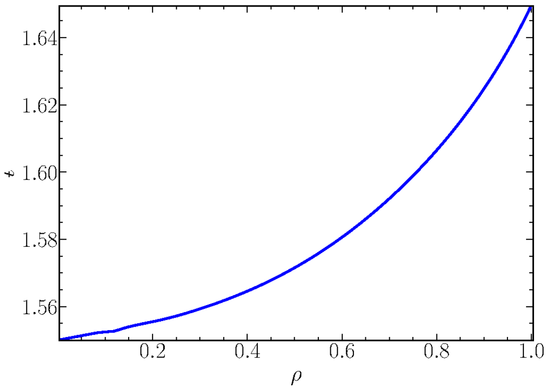

Figure 3.3: Rotational transform profile for the standard configuration.

and temperatures achieved in stationary conditions range from 0.5 to 1.5×10^{19} m^{-3} and 1.8 to 0.5 keV respectively. Plasma is created and heated by ECRH, NBI or a combination of both. A brief description of both systems, with emphasis on the production of the neutral beam inside the injector, is presented in the following sections.

3.1 ECRH system

Two 53.2 GHz gyrotrons, each of them generating up to 250 kW of EC power, heat the plasma using second harmonic X–mode [19]. The power of each gyrotron is guided towards the vacuum vessel by its corresponding quasi-optical transmission line. Two internal steerable mirrors, one for each ECRH beam (ECRH1 and ECRH2), allow us to scan the plasma toroidally and poloidally. The mirrors are located at stellarator-symmetric positions[1] ensuring, in principle, electron-cyclotron driven current compensation when launching parameters are equivalent. ECRH and NBI heating systems and their power injection geometry are illustrated in figure 3.4.

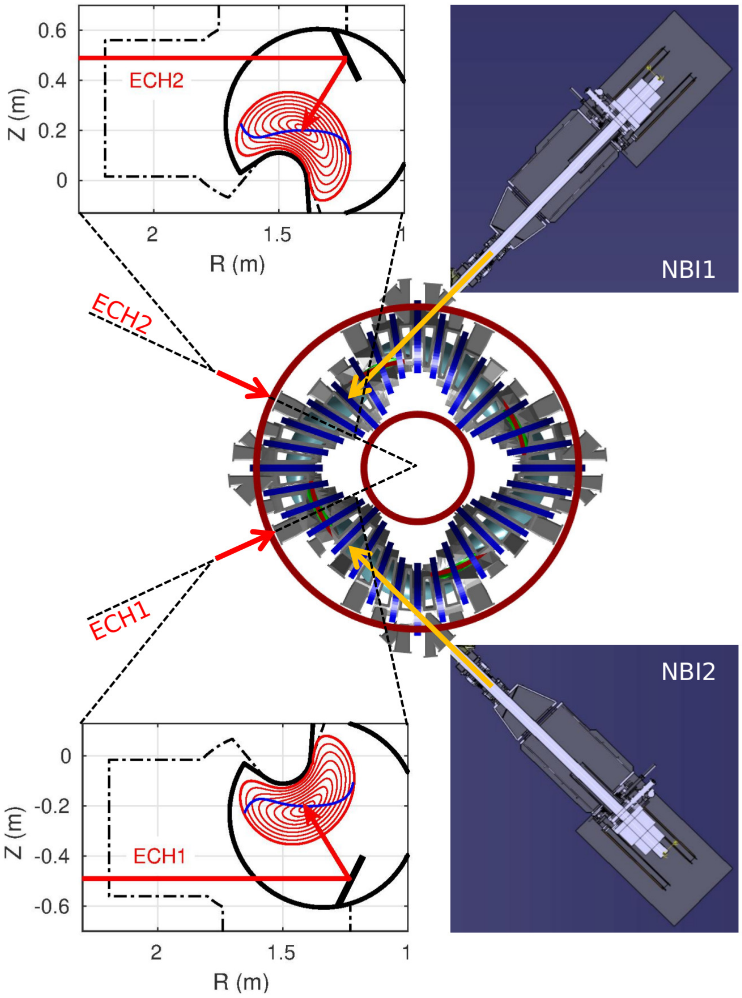

Figure 3.4: TJ-II stellarator heating systems. The last mirror of each ECRH transmission line is steerable. Both are located inside the vessel at stellarator-symmetric positions. Neutral-beam sources launch their beams parallel and anti-parallel to the magnetic field direction, which is mainly counter-clockwise when looking from above. NBI1 is the co-injector.

---

[1] Stellarator symmetry is defined as the transformation $(R, \phi, z) \to (R, -\phi, -z)$ by which scalar and vector fields transform as $f(R, \phi, z) = f(R, -\phi, -z)$ and $[F_R, F_\phi, F_z] = [-F_R, F_\phi, F_z]$.

3.2 NBI system

The NBI heating system consists of two injectors, NBI1 and NBI2, each providing up to 700 kW of co- and counter sub-Alfvénic H_0 beams ($v_{beam}/v_A \sim 0.3-0.5$ for line averaged densities around $0.5-1.0 \times 10^{19}$ cm^{-3} with ion source currents up to 60 A and with a maximum acceleration voltage of 34 kV [20]. As corresponds to tangential injection (see figure 3.4), a high fraction of the fast ions have passing trajectories with a pitch ($\xi = v_{\|}/v$) distribution of the born ions strongly peaked around $\xi = 1$ [21]. Although they are technically identical, the focusing points of the injectors are also located at stellarator symmetric positions. The beam produced by NBI1 (see figure 3.4) is directed parallel to the magnetic field (co-injection) while the beam produced by NBI2 is directed in the opposite direction (counter-injection). The production of the neutral beam starts in the ion source of the injector (see figure 3.5).

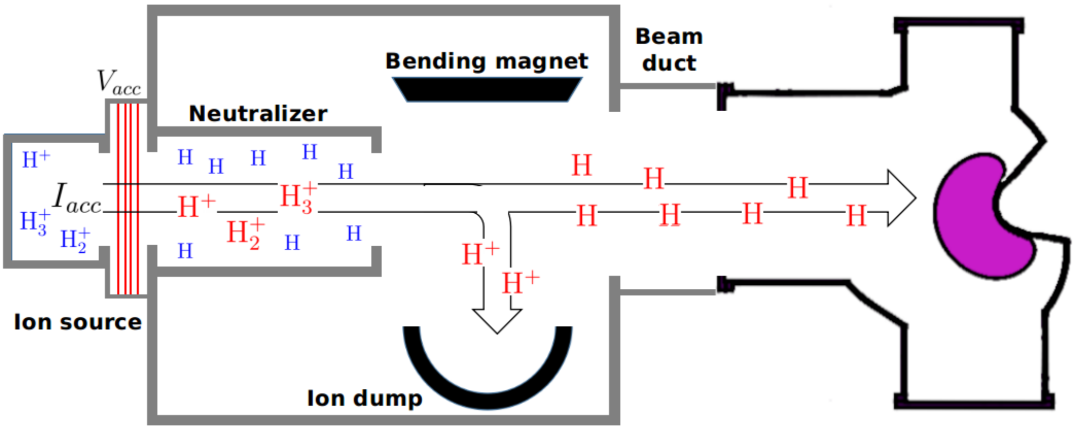

Figure 3.5: Sketch of an NBI injector and its different components coupled to the TJ-II vessel. The blue and red colors represent cold and accelerated particles, respectively.

There, pure-hydrogen gas is injected to generate a cold plasma (partially ionized only) with an electric arch. The fraction of gas ionized by the arch is extracted from the ion source and accelerated with a set of charged grids, resulting in an ion current I_{acc} composed of H^+, H_2^+, and H_3^+ molecules at $E_{max} = qV_{acc}$. Once the ion beam has passed the last grid (grounded) of the ion source, it enters the neutralizer, which consists essentially of a chamber containing hydrogen gas and an ion dump. Most of the beam ($\sim$ 60%) gets neutralized by CX reactions with the background gas and the rest is deviated to the ion dump using a bending magnet. In addition, the collisions with the gas make the molecules resulting from the neutralization dissociate in $H_n + E_{max} \rightarrow n(H + E_{max}/n)$

to finally give a total neutral beam of hydrogen whose particle energy fractions[2] are approximately 40%, 30%, 30% at energies E_{max}, $E_{max}/2$, $E_{max}/3$, respectively. The neutral beam generated directs through the duct to the vacuum chamber of TJ-II (see figure 3.5).

3.3 TJ–II Diagnostics

TJ-II is equipped with several diagnostics allowing us to fully characterize the plasma. Among all the available diagnostics, the ones which are relevant, whose inputs are needed to carry out fast-ions simulations, are:

- Microwave interferometer: provides the line integrated plasma density
- Thomson scattering [22]: measures the radial profiles of electron density and temperature once per shot
- Heavy-ion-beam probes [23](HIBP): measure the radial profiles of plasma potential at different toroidal locations among other quantities
- Doppler reflectometer [24]: provides the radial electric field in the outer region of the plasma
- Profile reflectometry [25] and Helium beam [26]: provides plasma profiles in the outer region of the plasma
- Neutral particle analyzer (NPA) [27]: gives the central ion temperature
- Radiation diagnostics: used to reconstruct the effective charge profiles (Z_{eff}) and the density of neutrals in the plasma.

Other diagnostics [28], as the electron cyclotron emission radiometer (ECE), that traces the time evolution of the plasma temperature or the Rogowski coils, used to measured the toroidal plasma current are also available.

---

[2] These values depend on I_{acc} and V_{acc}. In fact, some of the different combinations of the two parameters can change the beam divergence to the extent of reducing significantly the efficiency of the injector. The parameter directly related with the beam divergence is the perveance, $P = I_{acc}/V_{acc}^{3/2}$

4. Fast-ion modelling in TJ-II with ASCOT5

The ASCOT5 code [29–31] is an orbit-following Monte Carlo code whose main purpose is to calculate the fast-ion distribution function[1]. The inputs taken by ASCOT5 are a model of the vacuum vessel of the device, the components of the magnetic field and normalized magnetic flux evaluated in a spatial grid, the plasma density, temperature and electric-field profiles, and a representative initial distribution of the test particles. Taking all the inputs together, ASCOT5 solves the Fokker-Planck equation by integrating its associated Langevin's equations of motion (see equations (2.60) and (2.61)) in cylindrical coordinates, accounting also for the collisions with the background plasma, The construction of the distribution function is carried out statistically in runtime from the position and velocities of the test particles.

As in fluid mechanics, the computation of the trajectories of a realistic number of particles ($\sim 10^{23}$) in the plasma is impossible in technical terms. This problem is sorted out in Monte Carlo simulations using an artifact. Computationally, the population of test particles can be substituted by a distribution of entities, *markers*, so that the distribution of test particles is represented by a much smaller number of these artificial markers, whose behaviour in the system is similar to the actual particles's. The markers are labelled with a weight (w) that accounts for the actual number of test particles per second each marker represents. Hence, the total power carried by the test-particle population is $P = \sum_{i=0}^{N} w_i E_i$, where N is the number of markers and E_i their energies. In practice, the number of test particles in the k^{th} differential volume element of phase space is $N_k = \sum_{i=0}^{N} w_i (\Delta t)_{ik}$, where $(\Delta t)_{ik}$ is the time the i^{th}-marker has spent in the k^{th} volume element. The distribution of initial markers must characterize sufficiently well the initial distribution of test particles so that the solution obtained from such population of markers provides an accurate solution of the Fokker-Planck equation (2.37). Likewise,

---

[1] ASCOT5 can also be used for thermal particles or for the study of single-particle orbits.

its number must be high enough to have a converged solution and reduce the statistical error.

The independent orbit-following and slowing-down processes (equations (2.60) and (2.61)) take the initial markers and evolve their equations of motions in the electromagnetic field and the plasma. In a typical simulation of TJ-II plasmas, the full-orbit trajectories of roughly $2 \cdot 10^5$ markers are followed. The trajectories are computed until they meet at least one of the ending conditions, which are given also as input parameters. The time discretization of the orbit has been chosen to be $\Delta t = (\Omega_i/20)^{-1}$, where Ω_i is the ion gyrofrequency. Although there are several independent ending conditions implemented in ASCOT5, the most commonly used are "thermalization" and "wall hit". Markers have been considered thermalized (i.e. they are no longer fast ions) when their energy is reduce down to $2T_i$, where T_i is the thermal ion temperature, and the "wall hit" occurs when the trajectory of the marker crosses one of the tiles of the wall mesh. Another commonly used ending condition is the maximum radial coordinate, especially if one is not interested in the wall hits or in the slowing-down process. This allows us to end the trajectories of the markers when the radial drift moves the markers to a user-defined value of the radial coordinate ($\rho = 1$ for the LCFS).

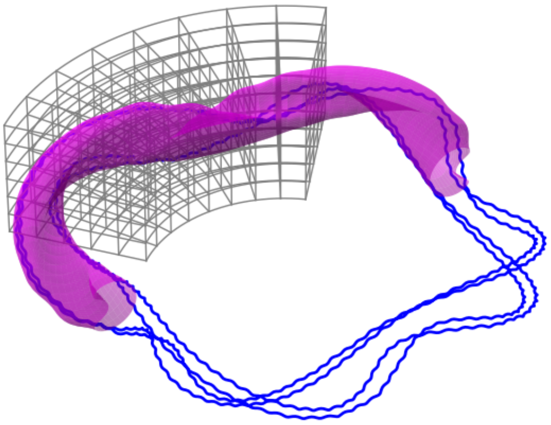

Figure 4.1: Computed trajectory of a marker in TJ-II.

One of the main differences with other analogous codes, and the reason to choose ASCOT5 for this thesis, is that it is able to follow the complete gyro orbit of the markers, without needing to invoke the guiding-center approximation[2], which is not necessary valid in small/low-field devices, such as TJ-II. In addition, ASCOT5 can also include extra physical phenomena such as CX reactions or MHD activity. The diversity of inputs

---

[2] This approximation is valid only when the magnetic-field variation during one gyro orbit is small, $B/\nabla B \gg \rho_L$.

that ASCOT5 needs makes necessary the use of other specific purpose codes. The choice of these codes is not unique and there are many options available in the community. The aim of this chapter is to make a detailed description of the procedure followed to obtain the inputs for ASCOT5.

4.1 Wall model

ASCOT5 can follow the initial markers up to the first wall of the device (same as the vacuum vessel in the TJ-II case), therefore, a model of a first wall of the actual device must be included in the simulations. The format of the model is a triangular mesh of the first wall, which is enough, for instance, to evaluate the power loads to the tiles corresponding to sensitive plasma facing components or to predict fast-ion loss detector (FILD) performance using the ASCOT5 output. The wall input format is similar to the STL file that, in our case, has been exported from the CAD files of the device (see figure 4.2). The triangular wall mesh used in the TJ-II simulations is composed of 303241 tiles.

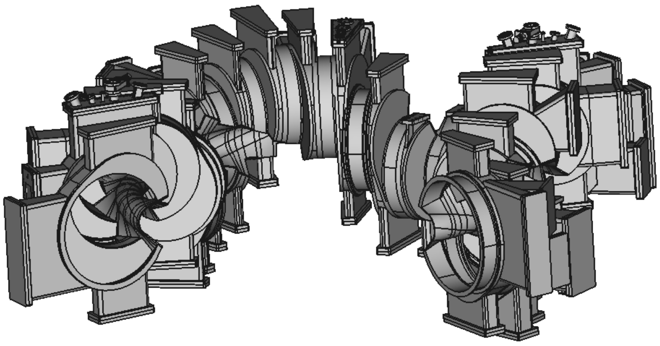

Figure 4.2: Model of the TJ-II vacuum vessel.

4.2 Magnetic configuration

The input of the magnetic configuration in ASCOT5 consists of four spatial 3D grids: one for each component of the magnetic field and another for the normalized magnetic flux. The former ones are used to compute the trajectories of the test particles, and the latter for evaluating the radial positions of the markers, which are used in turn to evaluate the radial plasma profiles or to finalize the marker's trajectories at a predetermined radial position (such as when they leave the plasma region at $\rho = 1$). This is a quite common approach in slowing-down simulations. The grids of the magnetic configuration have been constructed from a magnetic-equilibrium calculation and a filamentary model of the actual coils of the device with their corresponding currents. The coil system of TJ-II is composed of thirty two toroidal field circular-shaped coils (TF), two vertical field circular-shaped coils, a circular coil (CC) and a helical coil (HX). Figure 4.3 shows the TJ-II coils (left) and the filamentary model used to describe the magnetic field (right). It is worth mentioning that all the coils of TJ-II are modeled by a single filament except the helical one, which is modeled by ten filaments.

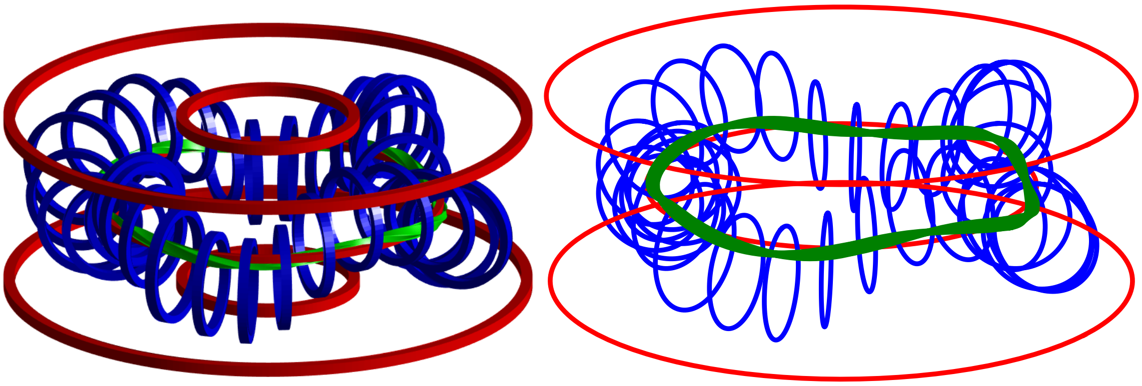
(a) **(b)**

Figure 4.3: (a) Representation of the actual coils of TJ-II and (b) their corresponding filamentary model used to calculate the magnetic field outside the plasma region.

The widely used equilibrium-code VMEC [18], which solves equation (1.2), gives the information to obtain the coordinates of the flux surfaces and the magnetic field structure as a function of the normalized magnetic flux, s. However, this code only gives information about equilibrium, which is defined only up to the LCFS. Then, for the purpose of orbit-following codes that need to calculate the trajectories of the markers beyond this boundary, another code must be used to calculate the magnetic field in the region beyond the LCFS. The code EXTENDER [32] has been used with that aim. It takes as input the VMEC equilibrium file and the model of the coils to give a cylindrical grid with the components of the magnetic field in the whole volume of the device. In figure 4.4, the result of EXTENDER for the intensity of the magnetic field is plotted on the left and the normalized magnetic flux grid obtained from VMEC on the right, both at $\phi = 0$.

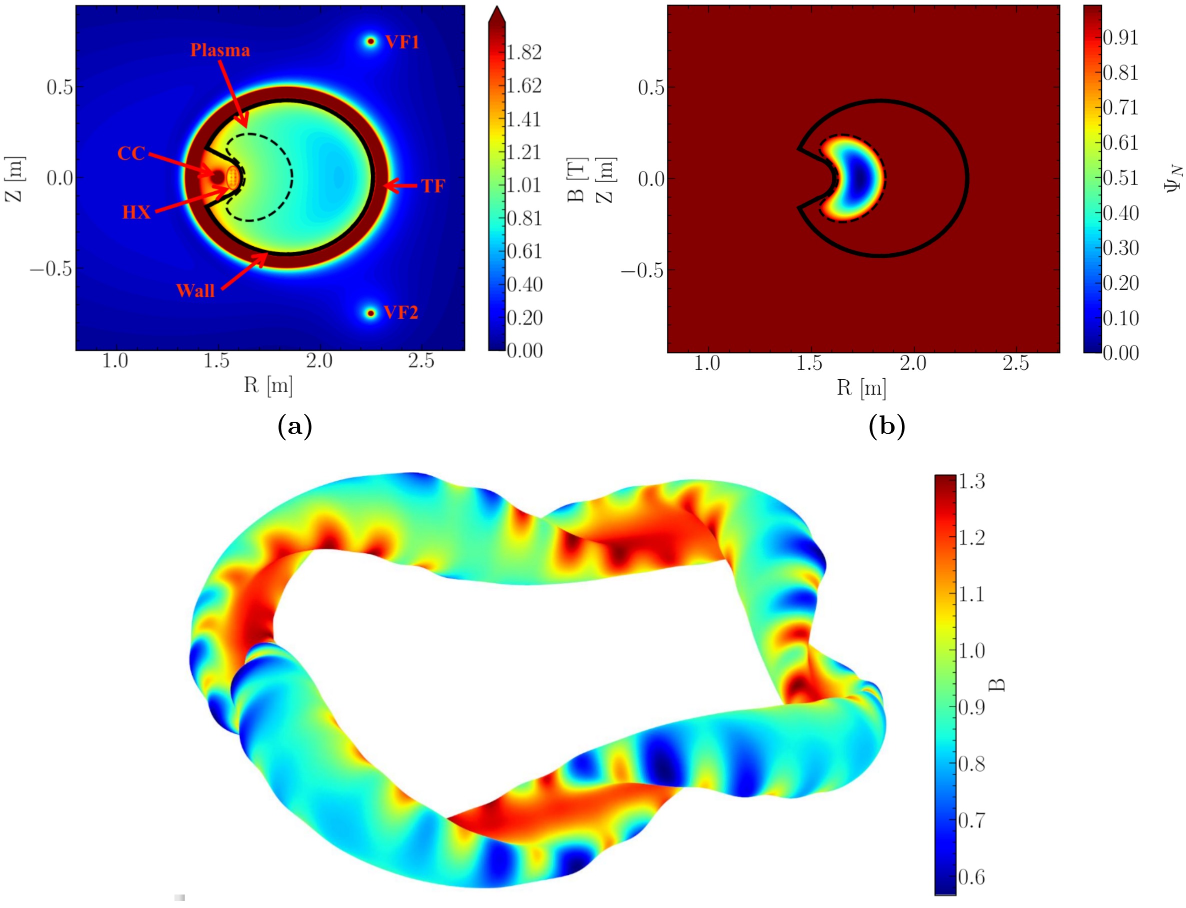

(a) **(b)**

(c)

Figure 4.4: (a) Intensity of the magnetic field created by the coils (saturated to 2 T) and position of the wall and LCFS (solid and dashed black lines). (b) Contours of the normalized magnetic flux, the position of the wall and LCFS (solid and dashed black lines). Both quantities correspond to the standard magnetic configuration of TJ-II at $\phi = 0$. (c) Contours of magnetic-field intensity on the LCFS.

4.3 Plasma profiles

In order to account for the collisions, we need to include the radial profiles[3] of the thermal plasma. These profiles must contain the electron and ion[4] densities, the electron and ion temperatures, and the electric field. The source of all this information is generally taken from plasma diagnostics or from transport codes. This thesis includes both kinds of simulations: profiles obtained from experimental data and from the transport code

---

[3] Actually, ASCOT5 is able to calculate collisionless trajectories or even include 3D profiles.

[4] Several ion species ($Z < 9$) can be included

ASTRA [33]. In figure 4.5, a typical example of NBI plasma profiles is shown.

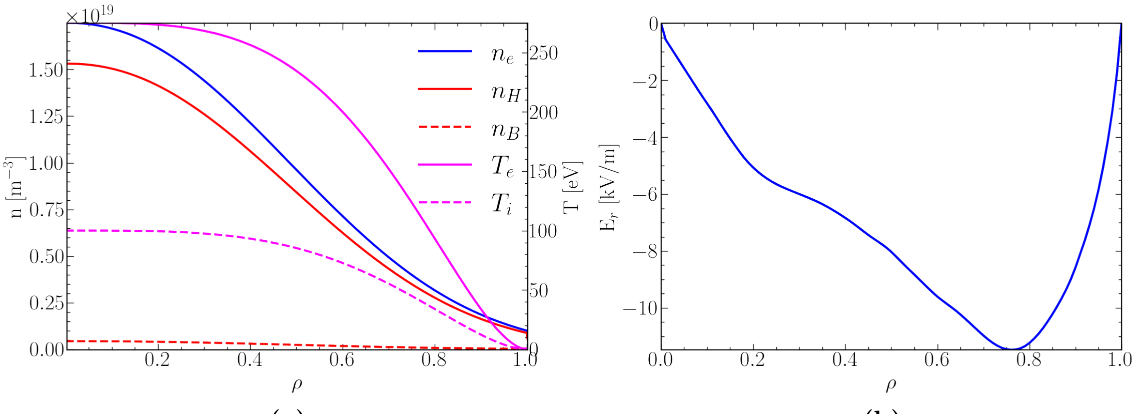

(a) **(b)**

Figure 4.5: (a) Densities and temperature plasma profiles of the thermal species. (b) Radial electric-field profile.

4.4 BBNBI: Initial distribution of NBI markers

The Monte Carlo code BBNBI (beamlet-based neutral beam injection) [34, 35] is a module of the ASCOT5 code that simulates the initial markers representing the population of newly born fast ions created by the NBI. Starting from geometric models of the actual injectors, BBNBI follows the ballistic trajectories of the neutral particles and simulates their ionization process within the plasma.

4.4.1 Geometric model of the injector

The actual elements of the injectors needed to model the NBI are the last grid of the injector, figure 4.6, and the scrapers (duct or window port) that the neutrals might come across in their trajectory towards the plasma. The NBI is modelled in BBNBI with a set of sub-beams (*beamlets*) whose origins lie in the last grid (represented as the last red line of the ion source in figure 3.5) and point at the focus of the injector (see figure 4.7). The finite size of the holes of the grid is taken into account distributing the power of each beamlet according to a normal distribution $\mathcal{N}(0, \delta_e)$, where δ_e is the *divergence angle* (see, for instance, [20]). The rest of the NBI parameters included in the model are the injected species, total injected power, full energy of the beam and the particle fractions.

The markers will follow ballistic trajectories until they hit any obstacle or they enter the plasma, where the ionization process takes place.

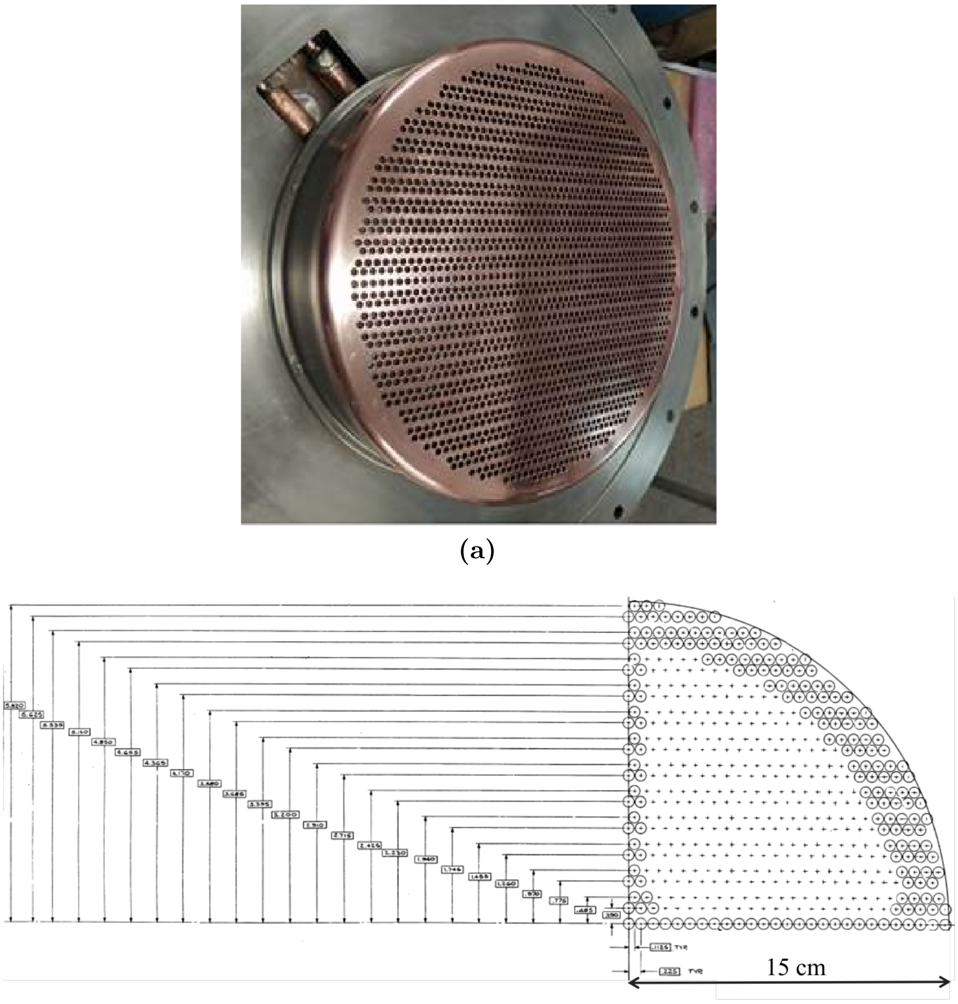

(a)

(b)

Figure 4.6: Picture and technical drawing of the grounded grids of the TJ-II injectors.

4.4.2 Ionization model

Once the neutral marker has entered the plasma, the ionization process is modelled cumulatively. The probability of ionization is given as

$$\mathcal{P}(l) = 1 - \exp\left(\int_0^l n_e \sigma(l') dl'\right) \tag{4.1}$$

where l is the distance that the marker has covered and σ is the ionization rate. This quantity is obtained from an analytical fit of experimental data, known as Suzuki's model

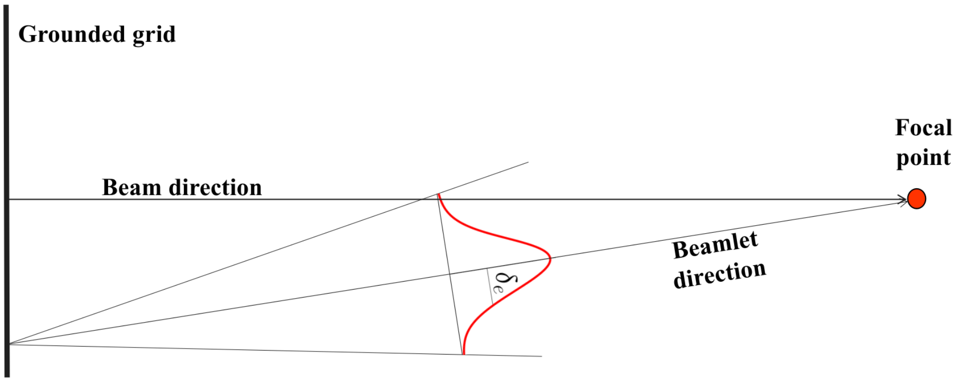

Figure 4.7: Cartoon of the beamlet divergence.

[36], and its expression is

$$\begin{aligned}\sigma =& A_1\frac{10^{-16}}{E}(1+A_2\varepsilon+A_3\varepsilon^2)[1+[1-\exp(-A_4N)]^{A_5}(A_6+A_7\varepsilon+A_8\varepsilon^2)]\\ &\cdot(1+A_9U+A_{10}U^2)\end{aligned} \tag{4.2}$$

where $\varepsilon = \ln(E[\text{keV/a.m.u}])$, $N = n_e/10^{19}$, $U = \ln(T_e[\text{keV}])$ and $\{A_j\}_{j=1}^{10}$ are fitting coefficients. In practice, a threshold is chosen randomly from a uniform $\mathcal{U}[0,1)$ distribution and if $\mathcal{P}$ reaches this threshold before the neutral collides with the vacuum vessel, it ionizes creating a fast-ion marker. In addition, if the marker exits the plasma and hits the wall without being ionizing, it is considered as shine-through. The total injected power is then sorted between the ionized makers and the shine-through ones. In figure 4.8, we can see a picture of the markers created by BBNBI inside the LCFS of a TJ-II plasma.

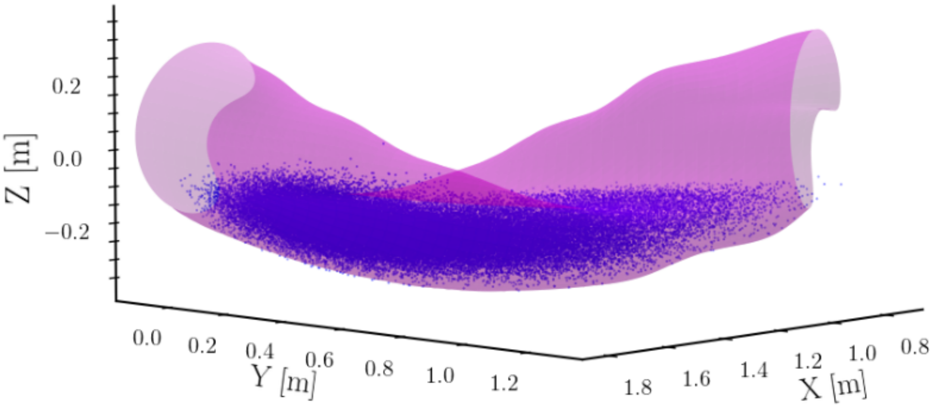

Figure 4.8: 3D distribution of initial markers inside the plasma created by BBNBI

4.5 Distribution function

The main result obtained from ASCOT5 is the distribution function of the test particles. ASCOT5 can calculate the distribution in 5D, either in $(\rho, \theta, \phi, v_\parallel, v_\perp; t, q)$ or $(r, \phi, z, v_\parallel, v_\perp; t, q)$ coordinate systems, and in 6D, using $(\rho, \theta, \phi, v_r, v_\phi, v_z; t, q)$ or $(r, \phi, z, v_r, v_\phi, v_z; t, q)$. This flexibility allows us to filter the test-particle species by their charges (very useful in simulations including CX) or by time scales (interesting to study processes whose time scale is bounded, such as prompt losses). A 2D example of a fast-ion slowing-down distribution function in velocity space, generated by co-NBI, is presented in figure 4.9.

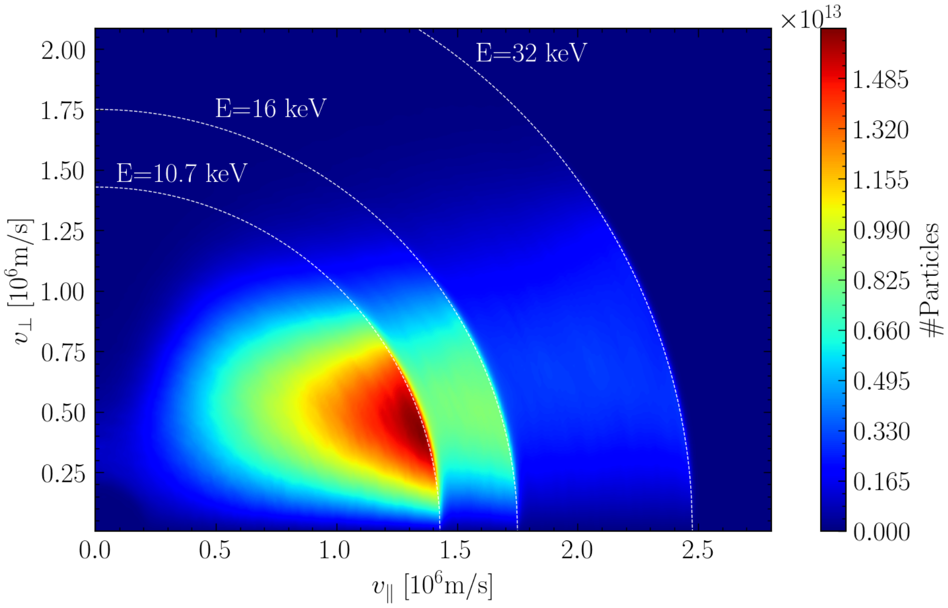

Figure 4.9: 2D histogram (proportional to the distribution function) calculated by ASCOT5 in velocity space. The dotted lines represent constant-energy curves.

5. Theoretical model of the neutral-beam current drive

The neutral-beam current drive (NBCD) is the non-inductive current generated in the plasma by NBI. In general, the population of fast ions in the plasma has a non-vanishing average parallel velocity, which results in a fast-ion current that drives the NBCD[1]. In tokamaks, NBCD is an active knob in plasma operation, e.g. to create the poloidal field in steady-state scenarios or to control the ι-profile and plasma rotation. Hence, its value can be comparable to the coil currents. In stellarators, however, the use of non-inductive currents is not necessary, since the magnetic configuration is fully created by external coils from design. Consequently, the existence of a net NBCD in the plasma can have a deleterious effect on the tailored magnetic configuration. Furthermore, the presence of NBCD in the plasma changes drastically the ι-profile, which in turn can produce undesirable effects on the plasma performance. On the one hand, it produces a shift in the relative position of the magnetic islands and divertors in stellarators that rely on the island divertor concept[2], such as W7-X. On the other hand, it modifies the spectrum of shear Alfvén waves, giving rise to the existence of unstable modes that, if excited, can deteriorate the fast-ion confinement, reducing their heating efficiency.

The current carried by the fast-ion beam in the direction parallel to the magnetic field is

$$J_{b\parallel} = Ze \int v_\parallel f_b(\mathbf{r}, \mathbf{v}) \, d\mathbf{v}, \tag{5.1}$$

---

[1] It is worth mentioning that scenarios with very low or even null NBCD can be designed either with sufficiently perpendicular or balanced NBI. The balanced scenarios are developed by injecting two neutral beams in opposite directions.

[2] The divertors are the components of the first wall specially designed to withstand high-power fluxes. The island divertor uses the magnetic islands, in which the radial transport is much higher than in the confinement region, to funnel the lost power to the divertors adjusting the position of the islands over them.

where $f_b(\mathbf{r}, \mathbf{v})$ is the fast-ion distribution function. The first attempt to calculate the NBCD in tokamaks was carried out by Ohkawa [37]. In that work, he gave an estimate of the electron return current that is created by the plasma electrons as a response to the beam ions, $J_{e||}$, so that the total NBCD would be

$$J_{||} = J_{b||} + J_{e||}. \tag{5.2}$$

This work was based on momentum conservation between the beam ions and the Maxwellian plasma electrons but the result could not explained the measured induced current at high electron temperatures [38]. Later studies took into account deviations from the Maxwellian distribution of the plasma electrons (*non-adiabatic electrons*) as well as electron trapping and electron-electron collisions in different collisionality regimes and for different approximations of the factor v_{Te}/v_b, where v_b is the typical velocity of the beam ions [39–44]. All these works were developed either for infinite plasmas or for tokamak geometries. Only one work, [45], has been found in the literature that is valid for non-axisymmetric configurations at low collisionalities. Therein, the result of the current driven by the beam in an infinite plasma developed in [40] is modified with a factor accounting for the electron trapping.

In this chapter, we present the drift kinetic equation (DKE) for the non-adiabatic plasma electrons in the presence of a population of fast ions and solve it in the low-collisionality regime. Particularly, the results of [45] are recovered and expanded to obtained a three-dimensional dependence of the electron return current that was not explicitly given in the original work.

5.1 Electron return current

We aim at calculating the electric current parallel to the magnetic field, $J_{||}$, driven by the beam ions. Assuming that the only contribution to the parallel flow of ions comes from the beam ions[3], equation (5.2) can be expressed as

$$J_{||} = e\left(Z_b n_b V_{b||} - \int v_{||} g_e \mathrm{d}^3 v\right). \tag{5.3}$$

---

[3] The flow of bulk ions and impurities is small enough to be neglected in stellarators (see Appendix A.4 of [46] and references therein)

Here, $V_{b||}$ is assumed to be given and g_e is the non-adiabatic component of the deviation of the electron distribution from a Maxwellian distribution[4],

$$f_{Me}(s,v) = n_e(s)\left(\frac{m_e}{2\pi T_e(s)}\right)^{3/2}\exp\left(-\frac{m_e v^2}{2T_e(s)}\right), \tag{5.4}$$

where we have maken explicit the dependence of equation (2.53) on the radial coordinate, s. We will employ the magnitude of the velocity, v, and the pitch-angle variable, $\lambda = B^{-1}(1 - v_{||}^2/v^2)$, as independent coordinates in velocity space.

We proceed to calculate g_e. The electron DKE reads

$$v_{||}\hat{\mathbf{b}}\cdot\nabla g_e - C_e^{(\ell)}[g_e] = -\Upsilon_e \mathbf{v}_M\cdot\nabla s f_{Me}, \tag{5.5}$$

where $\mathbf{v}_M\cdot\nabla s$ is the radial magnetic drift, Υ_e is a linear combination of the gradients of the plasma profiles and $C_e^{(\ell)}$ is the linearized electron collision operator (see Appendix A),

$$C_e^{(\ell)}[g_e] = C_{ee}^{(\ell)}[g_e] + C_{ei}^{(\ell)}[g_e] + \sum_k C_{ez_k}^{(\ell)}[g_e] + C_{eb}^{(\ell)}[g_e], \tag{5.6}$$

with $C_{ee}^{(\ell)}$, $C_{ei}^{(\ell)}$, $C_{ez_k}^{(\ell)}$ and $C_{eb}^{(\ell)}$ the electron-electron collision operator, the collision operator between electrons and main ions, the collision operator between electrons and impurities and the collision operator between electrons and beam ions, respectively. The expressions for these collision operators are given in Appendix A. Using those expressions, we can write (5.5) as

$$\begin{aligned} &v_{||}\hat{\mathbf{b}}\cdot\nabla g_e - \left(\nu_{ee} + \nu_{ei} + \sum_k \nu_{ez_k}\right)\mathcal{L}[g_e] \\ &\quad - \frac{m_e v_{||}}{T_e}\left(\nu_{ee}u_e + \nu_{ei}V_{i||} + \sum_k \nu_{ez_k}V_{z_k||}\right) f_{Me} = -\Upsilon_e \mathbf{v}_M\cdot\nabla s f_{Me} + \nu_{eb}\frac{m_e v_{||}V_{b||}}{T_e} f_{Me}, \end{aligned} \tag{5.7}$$

where the expressions for the collision frequencies and the operator $\mathcal{L}$ are also given in Appendix A. In (5.7), we have used that the pitch-angle scattering term of the $e-b$ collisions is negligible compared to the pitch-angle scattering term of the $e-i$ collisions because $n_b \ll n_i$.

---

[4] Indeed, using that $n_b V_{b||}/n_i \ll v_{te}$, one can prove that, to lowest order in n_b/n_i, the electron distribution function is of the form (5.4).

The solution of (5.7) is the sum of the solutions driven by each of the source terms on its right-hand side. Here, we are interested in computing the piece of g_e that is driven exclusively by the last term in (5.7). Hence, we concentrate in solving

$$v_{||}\hat{\mathbf{b}}\cdot\nabla g_e - \nu_e\mathcal{L}[g_e] - \nu_{ee}\frac{m_e v_{||} u_e}{T_e} f_{Me} = \nu_{eb}\frac{m_e v_{||} V_{b||}}{T_e} f_{Me}, \tag{5.8}$$

where we have defined

$$\nu_e := \nu_{ee} + \nu_{ei} + \sum_k \nu_{ez_k} \tag{5.9}$$

and used that the flows $V_{i||}$ and $V_{z_k||}$ produced by $V_{b||}$ are negligible, as it was mentioned at the beginning of this section.

5.2 Solution of the electron drift-kinetic equation at low collisionality

Define the collisionality of electrons with species s by $\nu_{es*} = \nu_{es}R_0/v_{te}$, where R_0 is the major radius of the device. If $\nu_{es*} \ll 1$ for $s = e, i, b$, we can expand g_e in powers of the collisionality,

$$g_e = g_e^{(0)} + g_e^{(1)} + \ldots \tag{5.10}$$

Without loss of generality, we can assume that $g_e^{(2k)}$ is odd in $v_{||}$ and $g_e^{(2k+1)}$ is even. To lowest order in this expansion, equation (5.8) gives

$$v_{||}\hat{\mathbf{b}}\cdot\nabla g_e^{(0)} = 0. \tag{5.11}$$

In what follows, we will need to distinguish between trapped and passing electrons. Trapped trajectories correspond to $\lambda > 1/B_{\max}$, where $B_{\max}$ is the maximum value of B on the flux surface. Passing particles are characterized by $\lambda \leq 1/B_{\max}$. For trapped particles, equation (5.11) implies that $g_e^{(0)}$ is constant along orbits and, for passing particles, that $g_e^{(0)}$ is constant on the flux surface. This piece of the electron distribution is found by going to next order in the collisionality expansion of the electron drift-kinetic equation.

Taking the next-to-lowest-order terms of (5.8) and averaging along the orbit we get, for trapped electrons,

$$\overline{\frac{v_{||}}{B}\partial_\lambda\left(v_{||}\lambda\partial_\lambda g_e^{(0)}\right)} = 0, \tag{5.12}$$

where the overbar denotes bounce average. The only solution to this equation that is odd in $v_{||}$ is

$$g_e^{(0)} = 0, \qquad \lambda > B_{\max}^{-1}. \tag{5.13}$$

Now, consider passing electrons. Multiplying the next-to-lowest-order terms of (5.8) by $B/v_{||}$ and flux-surface averaging, we obtain

$$\left\langle \frac{B}{v_{||}} \mathcal{L}[g_e^{(0)}] \right\rangle = -\frac{m_e}{\nu_e T_e} \left(\langle \nu_{eb} B V_{b||} \rangle + \nu_{ee} \langle B u_e \rangle \right) f_{Me}. \tag{5.14}$$

Using the expression for $\mathcal{L}$, this equation becomes

$$\partial_\lambda \left(\langle v_{||} \rangle \lambda \partial_\lambda g_e^{(0)} \right) = -\frac{(v/v_{te})^2}{\nu_e} \left(\langle \nu_{eb} B V_{b||} \rangle + \nu_{ee} \langle B u_e \rangle \right) f_{Me}. \tag{5.15}$$

Integrating once in λ, starting at $\lambda = 0$, we find

$$\partial_\lambda g_e^{(0)} = -\frac{(v/v_{te})^2}{\nu_e \langle v_{||} \rangle} \left(\langle \nu_{eb} B V_{b||} \rangle + \nu_{ee} \langle B u_e \rangle \right) f_{Me}. \tag{5.16}$$

The solution of this equation that is continuous at $\lambda = 1/B_{\max}$ is

$$g_e^{(0)} = -\frac{(v/v_{te})^2}{\nu_e} \left(\langle \nu_{eb} B V_{b||} \rangle + \nu_{ee} \langle B u_e \rangle \right) \left(\int_{B_{\max}^{-1}}^{\lambda} \langle v_{||} \rangle^{-1} \mathrm{d}\lambda \right) f_{Me}, \qquad \lambda \le B_{\max}^{-1}. \tag{5.17}$$

It remains to calculate $\langle B u_e \rangle$. Imposing the relation (A.7) on (5.17), we deduce

$$\begin{aligned} \langle B u_e \rangle = -&\left[\int \nu_{ee} \frac{m_e v_{||}^2}{T_e} f_{Me} \mathrm{d}^3 v + \left\langle B \int_{\lambda \le B_{\max}^{-1}} v_{||} \frac{\nu_{ee}^2 (v/v_{te})^2}{\nu_e} \left(\int_{B_{\max}^{-1}}^{\lambda} \langle v_{||} \rangle^{-1} \mathrm{d}\lambda \right) f_{Me} \mathrm{d}^3 v \right\rangle \right]^{-1} \\ &\times \left\langle B \int_{\lambda \le B_{\max}^{-1}} \langle \nu_{eb} B V_{b||} \rangle v_{||} \frac{\nu_{ee} (v/v_{te})^2}{\nu_e} \left(\int_{B_{\max}^{-1}}^{\lambda} \langle v_{||} \rangle^{-1} \mathrm{d}\lambda \right) f_{Me} \mathrm{d}^3 v \right\rangle, \end{aligned} \tag{5.18}$$

where $\int_{\lambda \le B_{\max}^{-1}} (\cdot)$ indicates that integration in velocity space is restricted to passing trajectories.

Then, the current due to the injection of neutral beams is

$$J_{||} = e \left(Z_b n_b V_{b||} - \int_{\lambda \le B_{\max}^{-1}} v_{||} g_e^{(0)} \mathrm{d}^3 v \right), \tag{5.19}$$

with $g_e^{(0)}$ given by (5.17) and (5.18). The explicit calculation of the integrals in equation (5.19) shows that $J_{||}$ can be written as

$$J_{||} = e Z_b n_b V_{b||} (1 - A) \tag{5.20}$$

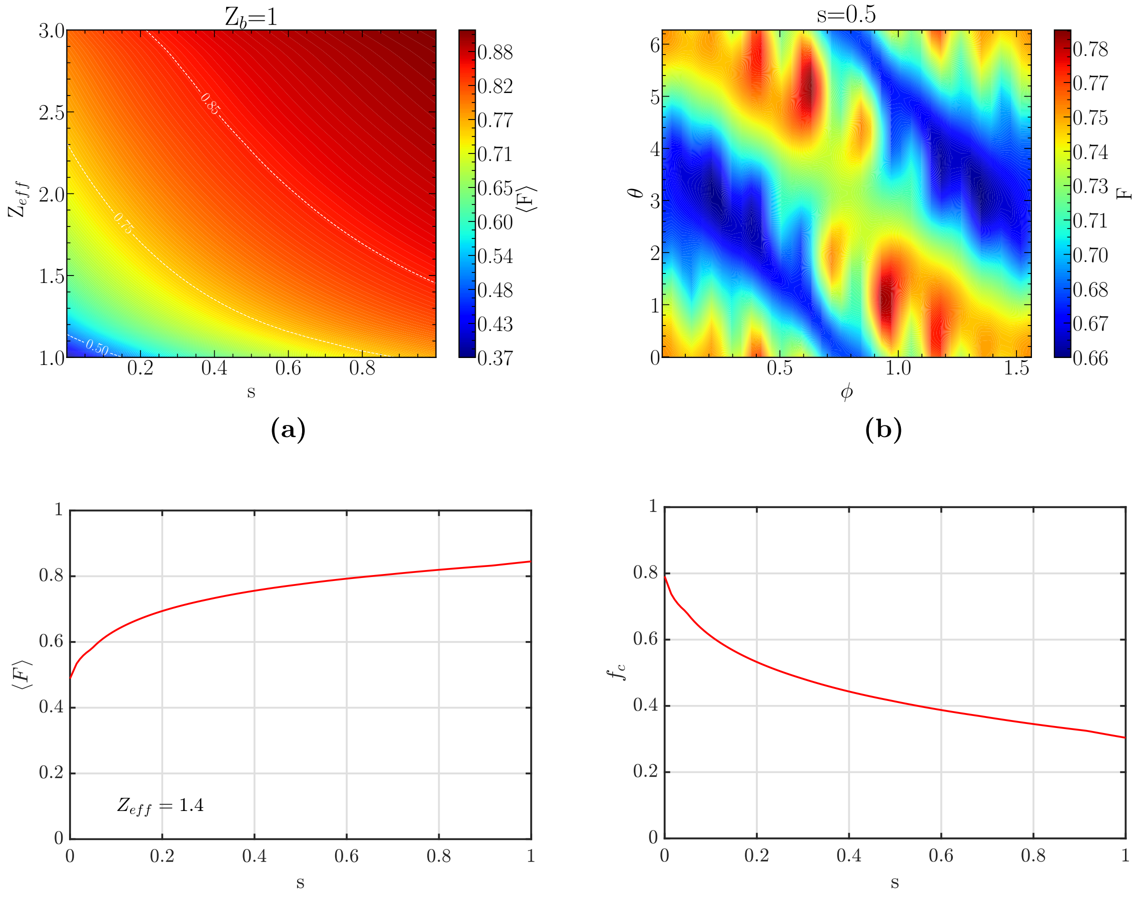

(a) **(b)**

(c) **(d)**

Figure 5.1: (a) Flux-surface-averaged shielding factor $\langle F \rangle$ as a function of Z_{eff} and s for the TJ-II standard configuration and hydrogen injection ($Z_b = 1$). (b) F evaluated at $s = 0.5$. (c)$\langle F \rangle$-profile for $Z_{eff} = 1.4$. (d) Radial profile of factor f_c.

with A given by

$$A = \frac{Z_b}{Z_{eff}} \frac{B\langle B \rangle}{\langle B^2 \rangle} \left[1 - \frac{8}{3\sqrt{\pi}} \frac{I_1}{1 + Z_{eff} \dfrac{I_2}{I_3} \dfrac{f_c}{f_t}} \right] f_c. \tag{5.21}$$

In (5.21), f_c is defined as

$$f_c = \frac{3}{4} \left\langle B^2 \right\rangle \int_0^{B_{max}^{-1}} \frac{\lambda}{\langle \sqrt{1 - \lambda B} \rangle} d\lambda, \tag{5.22}$$

and

$$\begin{aligned} f_t &= 1 - f_c, \\ I_1(Z_{eff}) &= \int_0^\infty \frac{x^4 h(x) e^{-x^2}}{h(x) + Z_{eff}} dx, \\ I_2(Z_{eff}) &= \int_0^\infty \frac{x h(x) e^{-x^2}}{h(x) + Z_{eff}} dx, \\ I_3 &= \int_0^\infty x h(x) e^{-x^2} dx \approx 0.27, \\ h(x) &= \phi(x) - G(x), \end{aligned}$$

where $x = v/v_{Te}$ and the functions $\phi(x)$ and $G(x)$ are given in Appendix A. Equation (5.20) shows that the NBCD is calculated applying the factor $1 - A$ to the fast-ion beam current. One of the main features of the term A is that it has a 3D dependence inherited from its proportionality to B, which means that the NBCD in general will not be a flux function. In addition, its inverse proportionality to Z_{eff} reveals that the more impurities in the plasma the less efficient the electron response, causing the NBCD to be closer to the fast-ion beam current. Lastly, the term Z_b makes that, for sufficiently high atomic number of the beam species injected, the direction of the NBCD can be opposite to that of the beam.

6. Simulations of NBCD in TJ-II

In this chapter, the computational methodology to simulate NBI with ASCOT5 and the theoretical tools to calculate NBCD, presented in chapters 4 and 5, come together to provide the numerical results about the fast-ion distribution function and its corresponding NBCD in TJ-II.

With the aim of exploring a wide range of plasma scenarios, a scan in the electron density and temperature profiles has been performed. The range of densities and temperatures selected for the scan correspond to high-density NBI plasmas and the reason for chosing such plasma scenarios choice was based on the level of development of the code ASCOT5. At the time this study was carried out, the code had not implemented CX reactions between the beam ions and the thermal neutrals of the plasma, which are known to be very important in low-collisionality TJ-II plasmas [47] ($>$ 70% of the ionized power lost by CX). Therefore, for the sake of a better accuracy of the results, the study was centered in high-collisional plasmas, which exhibit low levels of fast-ion losses due to CX (6%-12% of the ionized power).

For those plasma scenarios, we present the results for the neutral-beam ionization as well as features of the fast-ion distribution function such as density, energy distribution, power deposition and NBCD. In addition, comparisons between the NBI1 and NBI2 injectors and estimates of the fast-ion radial current are also included.

6.1 Plasma profiles

In order to obtain sets of consistent plasma profiles, a previous simulation of an evolving TJ–II NBI plasma, in which density increases, has been performed with the transport code ASTRA. The radial profiles with the lowest and highest core values produced by ASTRA ($3 \cdot 10^{19}$ and $6 \cdot 10^{19}$ m^{-3} for the density and 160 eV and 300 eV for the temperature) have been selected as boundaries for the scan in n_e, T_e-space (see blue and red curves in figure 6.1). The density profiles have been obtained by linear interpolation between the lowest and highest core values while the temperature profiles are the ones given by ASTRA for these densities. Here, the radial coordinate is ρ. The independent combinations of these density and temperature profiles give a total amount of 10×10 sets of plasma profiles that have been simulated with ASCOT5 and the results used to obtain 2D maps illustrating the dependence of the available power, power deposition and current drive on the plasma electron density and temperature.

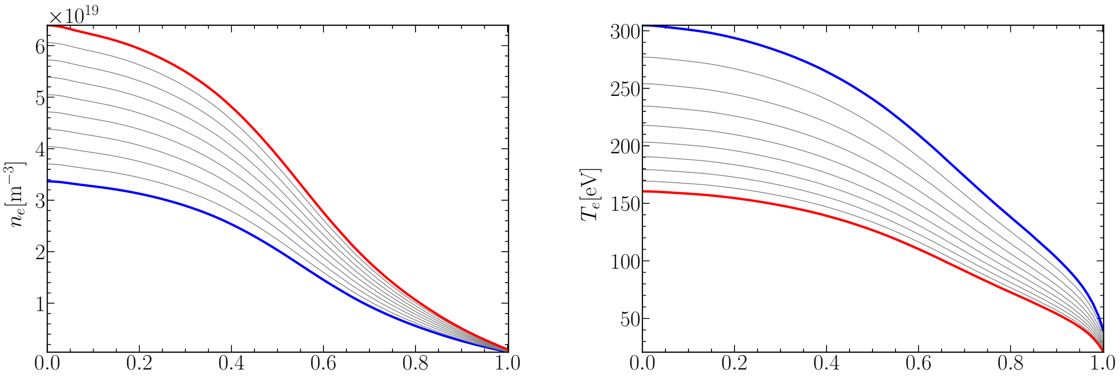

(a) **(b)**

Figure 6.1: Electron plasma density (a) and temperature (b) profiles used in the simulations. The consistent pairs of profiles obtained with ASTRA are plotted in red and blue lines.

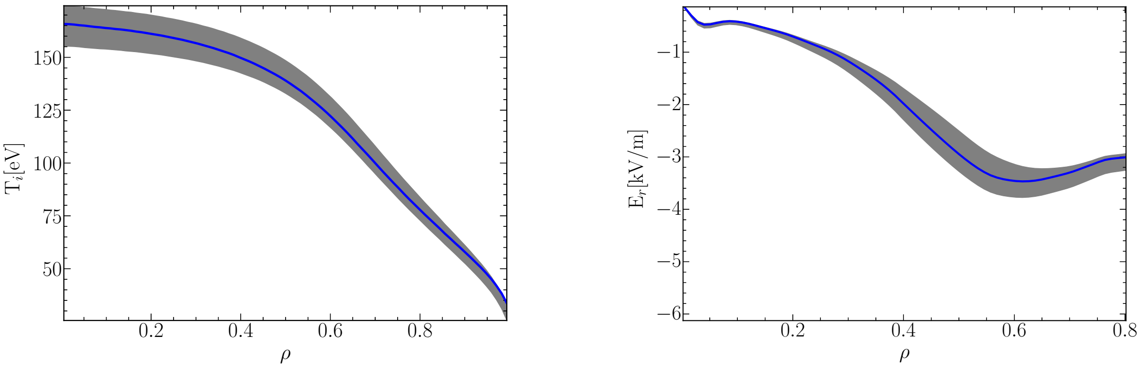

(a) **(b)**

Figure 6.2: Constant ion temperature (a) and radial electric field (b) profiles used in the simulations (solid blue lines). The shaded areas represent the variation of the profiles during the ASTRA simulation.

The rest of the plasma profiles (T_i, E_r, Z_{eff}, i.e. ion temperature, radial electric field and effective charge) have been kept fixed for all the ASCOT5 simulations since, on the one hand, ASTRA has shown no relevant differences as density increases and, on the other hand, it has been observed that such small variations of these quantities do not affect significantly the slowing-down fast-ion distribution function. The radial profiles of T_i and E_r are plotted in figure 6.2. No plasma impurities have been considered in the simulations ($Z_{eff} = 1$).

6.2 Initial distribution of markers

The initial ensemble of markers in the plasma has been calculated with BBNBI, which, using the specifications of the actual geometry of the neutral-beam injectors, simulates the ballistic trajectories of the hydrogen neutrals from the last (grounded) grid until they are either ionized in the plasma or lost as shine-through (ST) (see section 4.4). The NBI parameters of the BBNBI simulations have been $E_{max} = 31.5$ keV, with energy fractions of [55%, 25%, 20%] for the energy components [E_{max}, $E_{max}/2$, $E_{max}/3$] respectively and a port-through (PT) power of 500 kW. A total amount of $2 \cdot 10^5$ markers, which represents the population of initial fast ions in the plasma, has been obtained for each simulation. A top view illustrating the birth positions of the ensemble of NBI1 and NBI2 markers in the plasma is shown in figure 6.3, while figure 6.4 depicts six different cross-sections of the vacuum vessel and the position of the cloud of NBI1 markers within the LCFS. It can be seen in figure 6.5, where the number of initial NBI1 and NBI2 markers as a function of the device toroidal angle is shown, that the penetration of each neutral beam into the plasma column extends a bit further than half a period of the configuration (45°).

The dependence of the initial distribution of markers generated with NBI1 (co-injection) on ρ, pitch-angle ($v_\parallel/v$) is illustrated in figure 6.6 for the four different combinations of the highest and lowest densities and temperatures of section 6.1. A slight dependence on density is observed. Note that the results shown in figure 6.6 only reflect changes in the distribution of the $2 \cdot 10^5$ markers independently of the amount of power they represent, which depends on the specific values of n_e and T_e. The markers radial profile for the lowest density case (blue lines in figure 6.6a) appears shifted towards the core of the plasma, as the mean free path of the neutrals through the plasma is inversely proportional to the electron density [36]. No dependence on temperature is observed in the results (solid versus dashed lines in figure 6.6a). As for the dependence on the pitch-angle (see figure 6.6b), no clear changes are observed for different plasmas. The

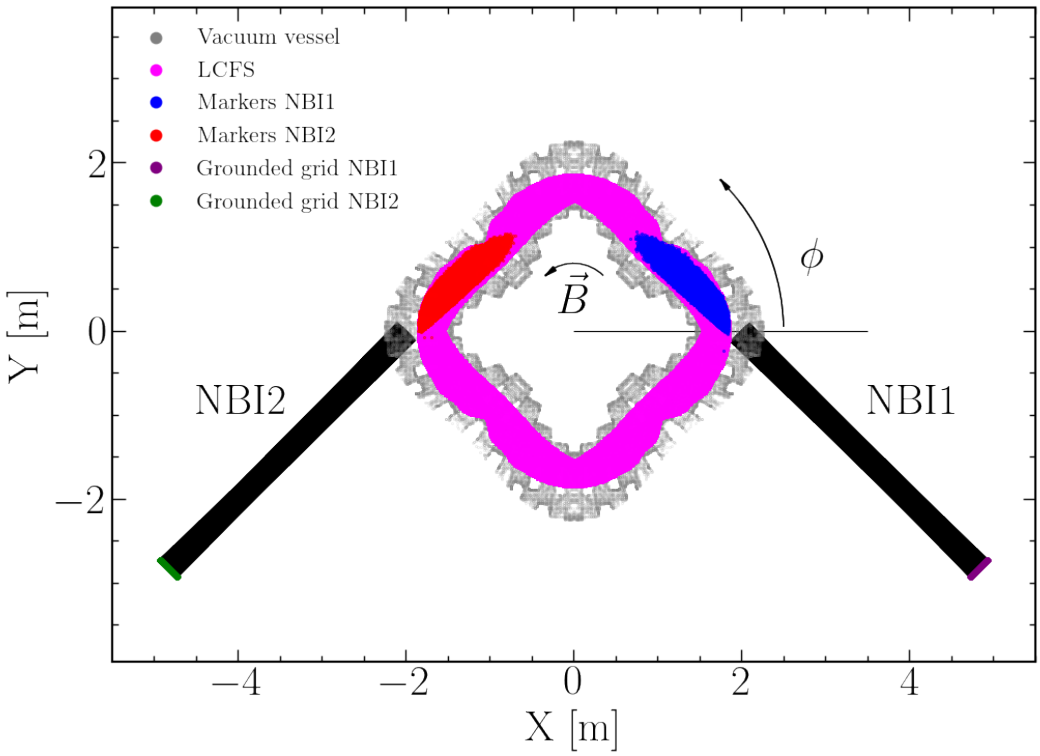

Figure 6.3: Top view of the TJ-II plasma, vacuum vessel, NBI directions, and location of the markers created by both injectors for the low-density high-temperature case.

pitch-angle of the initial markers illustrates the highly parallel character of the beams ($v_{\|}/v > 0.8$ for most of the markers). Regarding the initial energy distributions, around 30% of the initial markers are created with energy E_{max}, 31% with $E_{\mathrm{max}}/2$ and 39% with $E_{\mathrm{max}}/3$. The energy fractions of the initial markers are different from those of the injected neutrals because the ionization cross-section is higher at low energies [36]. Varying plasma density results in small differences (below 5%) in the proportion of markers created at each of the injection energies while no dependence on temperature is observed. The initial distribution of markers resulting from simulating NBI2 (counter-injection) are analogous to those of the NBI1 except for the pitch angle, which changes its sign.

The PT-power distributes in two parts depending on the capability of the plasma to ionize neutrals: the so-called available power, which is carried by the initial markers representing ionized neutrals; and the power lost as shine-through (ST), carried by neutrals that have crossed the plasma column without being ionized. The results, as obtained by BBNBI, showing the dependence of the available power on density and temperature are

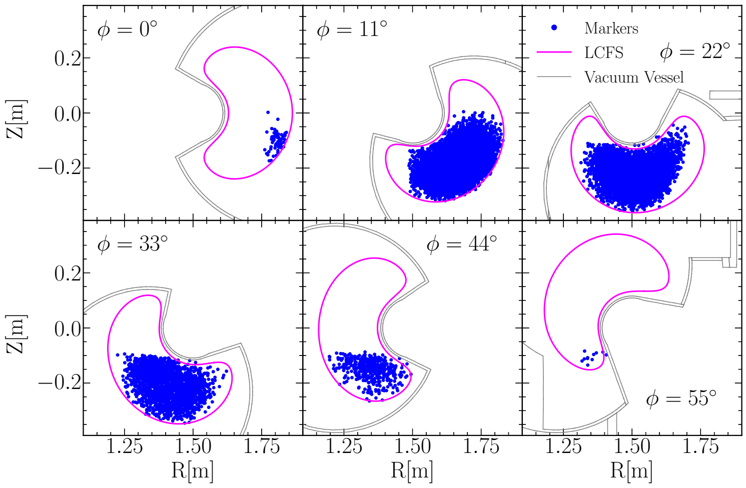

Figure 6.4: Position of NBI1 markers in the R-Z plane for six different toroidal angles. The LCFS and the vacuum vessel are also shown. The low-density high-temperature case is represented.

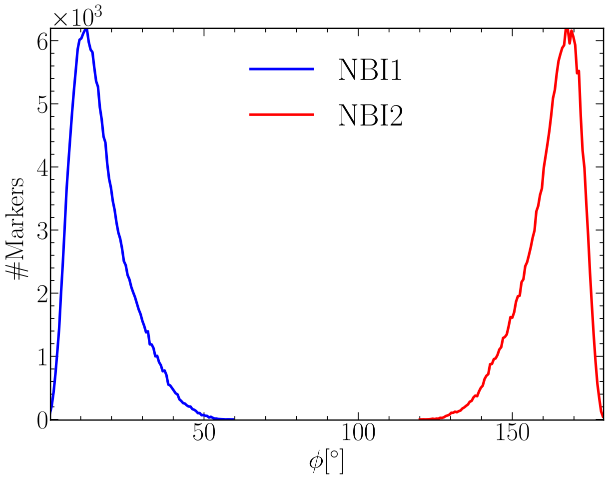

Figure 6.5: Number of NBI1 and NBI2 markers along the toroidal angle for the low-density high-temperature case.

shown in figure 6.7(a). The dependence on density for constant temperature ($T_e = 234$ eV) is shown in figure 6.7(b). The available power is highly dependent on the plasma density and almost independent of the temperature.

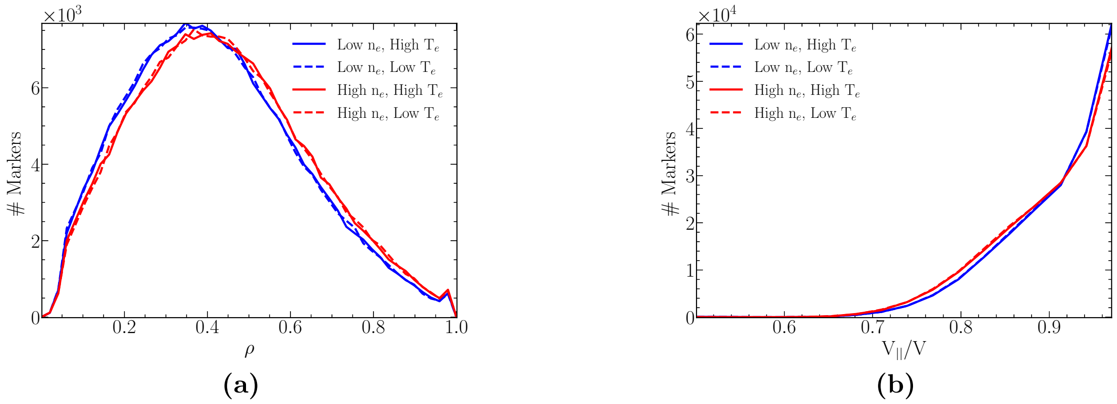

(a) **(b)**

Figure 6.6: Dependence of the initial profile of markers on the radial coordinate (a) and pitch (b), for the four cases considered.

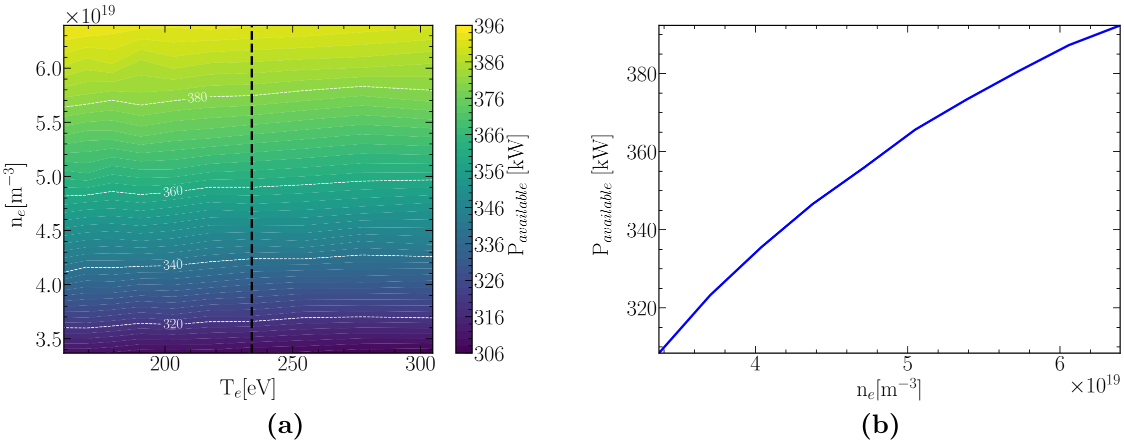

(a) **(b)**

Figure 6.7: (a) Dependence of the available power on electron density and temperature and (b) dependence on density for a given electron temperature ($T_e = 234$ eV) marked by dashed line on the left panel.

6.3 ASCOT5 slowing-down simulations

Once the initial distribution of markers has been created, we simulate the slowing-down process with ASCOT5. In these full-orbit simulations, the markers undergo the helical gyration motion and the drifts caused by the magnetic field as well as the Coulomb collisions with the bulk plasma, which produce pitch-angle scattering and slowing down. The interaction with the electric field is also taken into account.

ASCOT5 follows the trajectories of the markers through the plasma until they are thermalized or lost to the wall. Their steady-state distribution function is computed during the simulation. In our case, $2 \cdot 10^5$ markers have been followed using a time step $\Delta t = 1/(20\Omega_i)$, where Ω_i ($\approx 10^2$ MHz) is the typical ion gyrofrequency. Markers are considered thermalized when their energy is reduced down to twice the bulk-ion temperature by collisions. From the histogram provided by ASCOT5, we can calculate the fast-ion distribution function, $f(\mathbf{r}, \mathbf{v})$, where $\mathbf{r}$ and $\mathbf{v}$ are the position and velocity vectors, respectively. Thus, the fast-ion density (n_b) is given by equation (2.39).

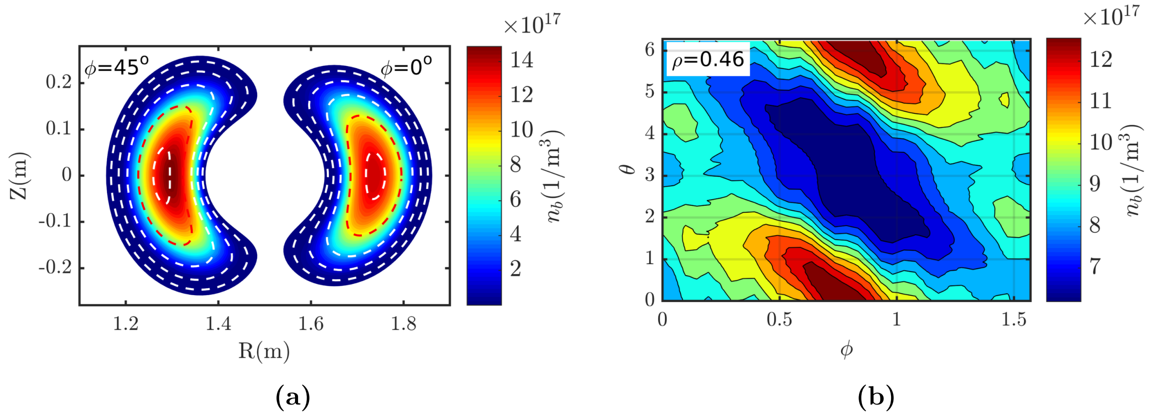

Figure 6.8: (a) n_b at $\phi = 0°$ and $\phi = 45°$ for the low-density, high-temperature case. A few contours corresponding to different flux surfaces (white dashed lines) are represented. (b) A map showing the dependence of n_b on the toroidal and poloidal angles for the flux surface $\rho = 0.46$ (red dashed line in (a)). The label θ corresponds to the poloidal VMEC coordinate. Only one period of the device is shown.

An example of the fast-ion density created by NBI1 together with the contours of a few flux surfaces is shown in figure 6.8. The structure of n_b reflects that it is not a flux function. The maximum and minimum displacements of the n_b-contours from the flux-surface ones is observed at $\phi = 45°$ (half period) and $\phi = 0°$ (beginning of period), which is consistent with the result reported in reference [48], that contains a detailed discussion on particle drifts for 40 keV ions and the displacement of their drift surfaces with respect to the flux surfaces. The values of the fast-ion density, initially given in cylindrical coordinates, have been interpolated in the VMEC grid of the corresponding magnetic equilibrium. In this way, we get $n_b = n_b(s, \theta, \phi)$, where θ and ϕ are the VMEC poloidal and toroidal angles, respectively.

We may immediately calculate the flux-surface average of the fast-ion density as in (1.9). The dependence of the fast-ion density on ρ and the energy profiles are presented in figure 6.9 for the four combinations of the n_e and T_e limiting profiles of section 6.1.

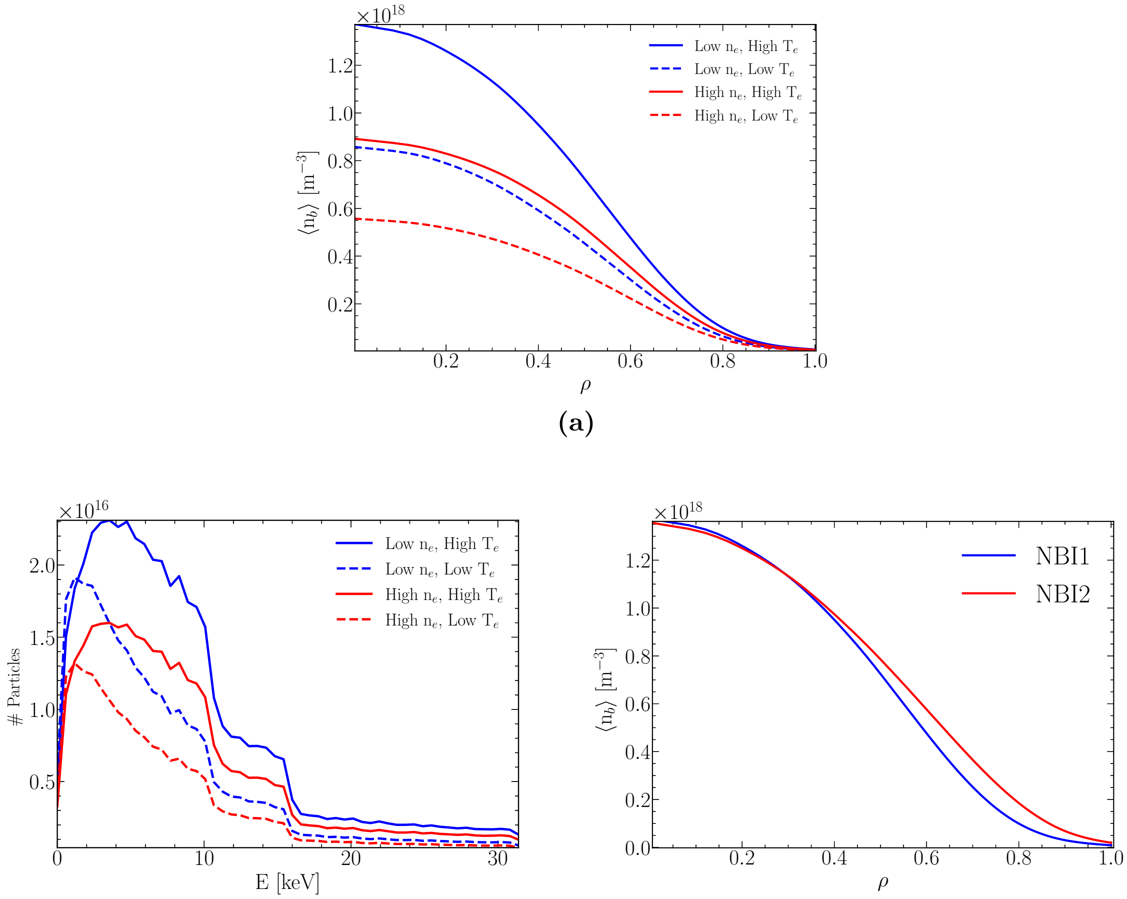

(a)

(b)

(c)

Figure 6.9: (a) Flux-surface-averaged fast-ion density as function of ρ, (b) energy histogram (both for NBI1 only) and (c) comparison of the NBI1 and NBI2 fast-ion density profiles for the low-density high-temperature case.

The most representative feature, shown in figure 6.9a, is the dependence of the fast-ion density on the collisionality of the different combinations of densities and temperatures: higher collisionality results in earlier losses, faster thermalization and a lower density of fast ions. In all cases, the energy distributions, presented in figure 6.9b, clearly show three steps coinciding with the operational energy values of the NBI. The fact that the slowing-down rate of fast ions against electrons decreases with energy makes fast ions spend a longer time at lower energies, which results in particle accumulation in the low energy range. The shape of the energy histograms at low energies is notoriously different for cases with same density but different temperatures. On the one hand, the maxima of the histograms are displaced to lower energies because of the lower values of the critical energy (the energy above which the electron drag dominates over the ion drag and which is roughly given by $E_c \approx 15\,T_e$ for a pure-hydrogen plasma [14]) at low temperatures. On the other hand, the total number of particles at low temperatures is smaller due to the higher values of the diffusion coefficients (see equations (26)-(31) of reference [29]), which shortens the slowing-down time and lifetime of fast ions. Figure 6.9c shows that the central fast-ion density is similar for both NBIs, while it is higher in the outer region of the plasma for NBI2. This is caused by the significantly different amount of prompt losses (we have considered as prompt those that occur before 10 μs) associated to each injector (see figure 6.10). This difference is caused by the opposite radial displacements of the drift surfaces, which are inversely proportional to the pitch-angle, of the particles injected by each NBI [48]. In TJ-II, the consequence is that the drift surfaces of particles injected with NBI1 (co-injection) move towards the helical coil, where they are more likely to collide with the vacuum vessel. In the case of NBI2 (counter-injection), they move towards the low field side of the plasma, where there is more space between plasma and vessel. These different amounts of prompt losses affect the average lifetime of the fast-ion distributions, represented in figure 6.10 by dashed lines.

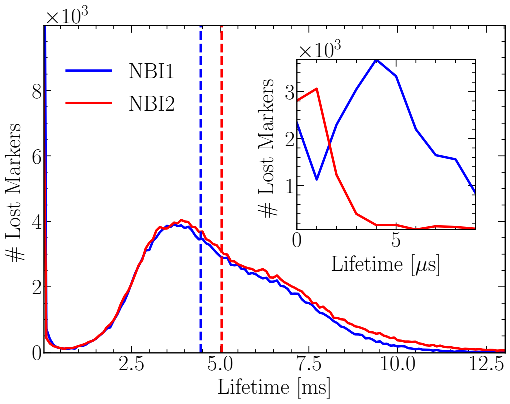

Figure 6.10: Histogram of the markers' lifetime for both NBIs in the low-density high-temperature case. The smaller plot shows the same information in the [0, 9] μs time interval in higher resolution. The dashed vertical lines indicate the average lifetime of the markers for both injectors, t=4.45 ms for NBI1 and t=5.04 ms for NBI2.

Although the dependence of the distribution function on T_i and E_r is not explicitly shown in this work, we have checked that the effect of moderate changes of these variables on the distribution function is small. As the slowing down is dominated by electrons for fast ions, small changes on the already low T_i do not affect the slowing-down distribution function. Also, the slight dependence on E_r is due to the high energy of fast ions, for which the $\mathbf{E} \times \mathbf{B}$ drift is overcome by the magnetic tangential drift, and the fact that the NBI markers are all passing, which makes the $\mathbf{E} \times \mathbf{B}$ drift less important for the confinement of fast ions. The impact of Z_{eff} on the distribution function in the range $Z_{eff} \leq 2$ is also minor. The main effect of thermal ions on the fast-ion population comes through pitch-angle scattering, which transfers fast ions from the passing to the trapped regions of phase space. Since pitch-angle scattering becomes relevant at low energies (< 5 keV) and, for this range of Z_{eff}, the difference between main-ion and impurity densities is large, the effect of Z_{eff} on the fast-ion distribution function is small. However, as we shall see, Z_{eff} has a much larger effect on the electron return current, which decreases with Z_{eff} (see section 5.2), and thus on the NBCD.

The absence of CX reactions in these simulations makes all the available power go to either bulk ions or electrons or wall losses. The amounts of power transferred to the bulk plasma are shown in figure 6.11. The results show that, as expected, higher collisional plasmas absorb more efficiently the power from the NBI.

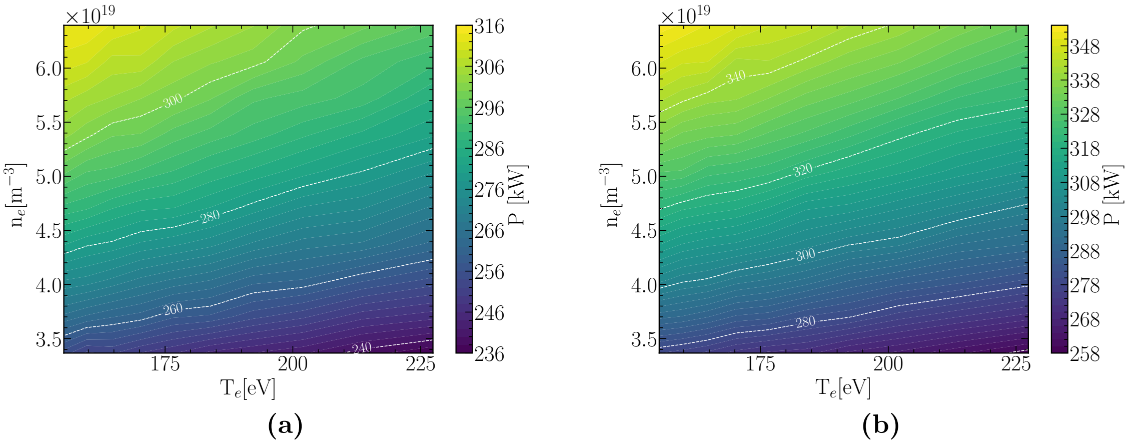

Figure 6.11: Power deposited by NBI1 (a) and by NBI2 (b) as a function of electron density and temperature for 500 kW port-through power.

In addition, the amount of power that goes to the plasma is higher in the NBI2 case. This is again explained by the higher amount of prompt losses of NBI1, which makes NBI2 inject effectively more power. It is worth noting that while the available power is independent of the electron temperature (recall figure 6.7), the deposited power in the plasma shows this dependency due to the slowing-down process (see figure 6.11). Should CX reactions had been included in the simulations, the power deposited would have been reduced by their corresponding amount of CX power losses, whose range of values was given in section 6.1 as calculated by FAFNER2. One caveat to consider, in case of a comparison of FAFNER2 results against ASCOT5's, is that FAFNER2 is only able to

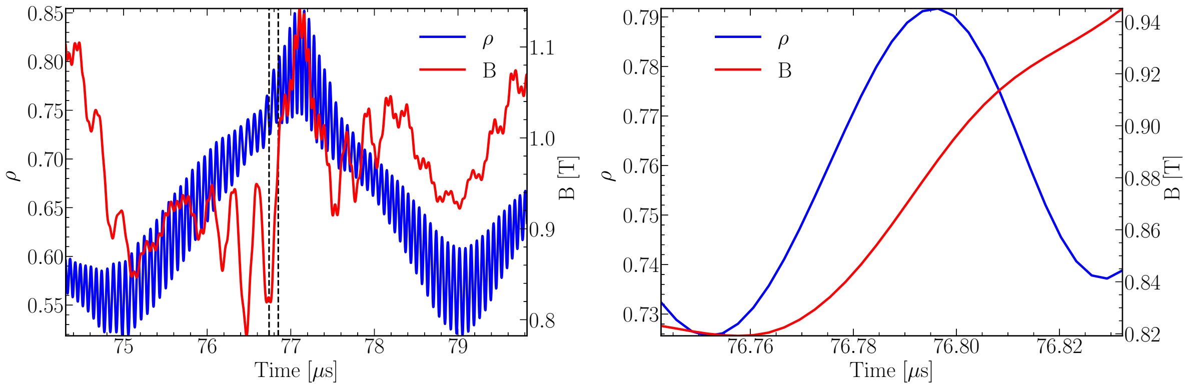

(a) **(b)**

Figure 6.12: (a) Radial coordinate (blue line) and magnitude of the magnetic field (red line) seen by a marker during its collisionless trajectory, (b) zoom in the region between the black lines shown in figure (a) and centered at $t = 76.79\mu s$.

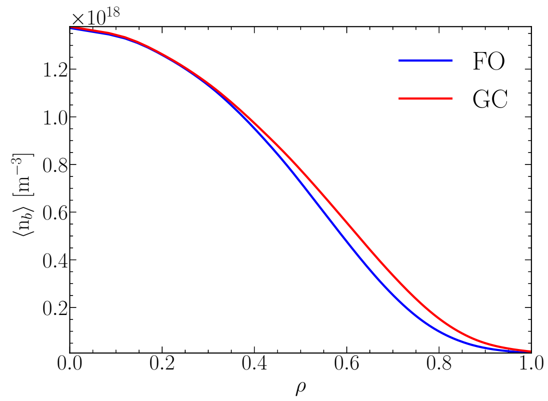

Figure 6.13: Flux-surface-averaged fast-ion densities obtained from full-orbit (FO) and guiding-center (GC) ASCOT5 simulations for the low-density high-temperature case. The results of the simulations give a higher population of fast ions for the GC case compared to the FO one. This excess of fast ions is located in the outer part of plasma.

follow markers using the guiding-center formalism. This assumes that the magnitude of the magnetic field does not change significantly along the gyro orbit ($|B/\nabla B| \ll \rho_L$, where ρ_L is the Larmor radius). However, as shown in figure 6.12, fast-ion trajectories in TJ-II cover the plasma cross section almost entirely, exploring regions of the plasma where the magnetic-field intensity experiences variations larger than 15% during one single gyro-orbit, which, rigorously speaking, makes the formalism inappropriate. Although a detailed analysis of guiding-center and full-orbit simulations is out the scope of this study, an illustration of this difference is shown in figure 6.13, in which it can be observed that the fast-ion population is higher in the guiding-center case and that the difference is placed in the outer part of the plasma. Both results have been obtained with ASCOT5.

6.4 NBCD

In chapter 5, we saw that the total NBCD, $J_{\|}$, was the contribution of two terms: the beam current, $J_{b\|}$, and a correction factor, $1-A$, coming from the response of the plasma electrons to the beam current,

$$J_{\|} = J_{b\|}(1-A). \tag{6.1}$$

Now that we have calculated the fast-ion distribution function, we are in a position to calculate $J_{b\|}$ using the analytical expression of A that was derived in section 5.2. As it was shown in the previous section, the fast-ion density is not a flux function and neither is A, since it actually depends on the magnetic field on the flux surface (see equation (5.21)). The 2D maps of $J_{b\|}$, $1-A$ and $J_{\|}$ are shown in figure 6.14.

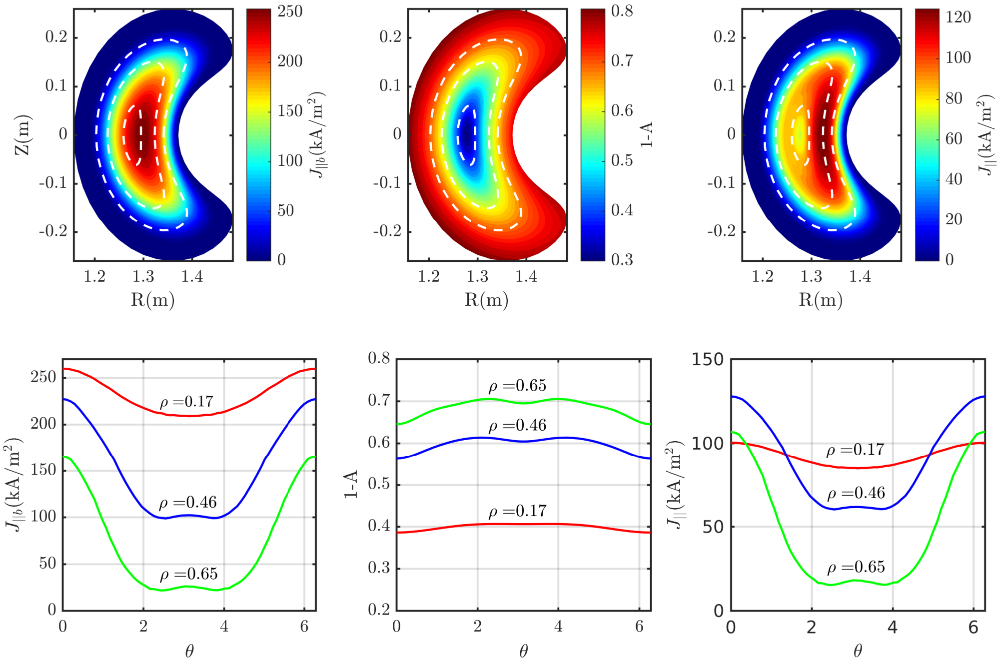

Figure 6.14: Top panels: 2D maps of $J_{b\|}$, $1-A$ and $J_{\|}$ at $\phi = 45°$, together with the contours of three flux surfaces represented by white dashed lines ($\rho = 0.17$, $\rho = 0.46$, $\rho = 0.65$). Bottom panels: the same quantities evaluated along θ on those flux surfaces.

That figure shows that the beam-driven current is not a flux-surface function. While $J_{b\|}$ exhibits a structure similar to that of n_b, and produces a flux-surface-averaged current density, $\langle J_{b\|} \rangle$, that peaks at the core, $J_\|$ reflects the fact that $J_{b\|}$ is more efficiently shielded by electrons in the core, where the trapped particle fraction is lower, and its flux-surface average peaks around $s = 0.1$ (see figure 6.15). The contribution of $J_\|$ to the total toroidal current inside a flux surface is calculated as follows,

$$\begin{aligned}
\mathcal{I}_{tor}(s) &= \int J_\| \hat{\mathbf{b}} \cdot d\mathbf{S}_\phi \\
&= \int_0^s ds' \int_0^{2\pi} J_\| \hat{\mathbf{b}} \cdot \nabla\phi \sqrt{g}\, d\theta \\
&= \int_0^s ds' \int_0^{2\pi} J_\| \frac{B^\phi}{B} \sqrt{g}\, d\theta \\
&= \int_0^s ds' \, \frac{d\mathcal{I}_{tor}}{ds'}
\end{aligned} \tag{6.2}$$

where $d\mathbf{S}_\phi = \nabla\phi\sqrt{g}\, ds d\theta$ is the surface differential at constant toroidal angle ϕ, and $B^\phi = \mathbf{B} \cdot \nabla\phi$ is the contravariant component of the magnetic field along ϕ. All these quantities are calculated with the vacuum VMEC equilibrium used in the slowing down simulations. The profiles of the toroidal current density, $d\mathcal{I}_{tor}/ds'$, and the integrated current, $\mathcal{I}_{tor}(s)$, created with NBI1 and NBI2, for the low-density high-temperature case, are shown in figure 6.15. Following a trend similar to that of the fast-ion density (recall figure 6.9c), the NBI2 current density is higher in the outer part of the plasma, which is

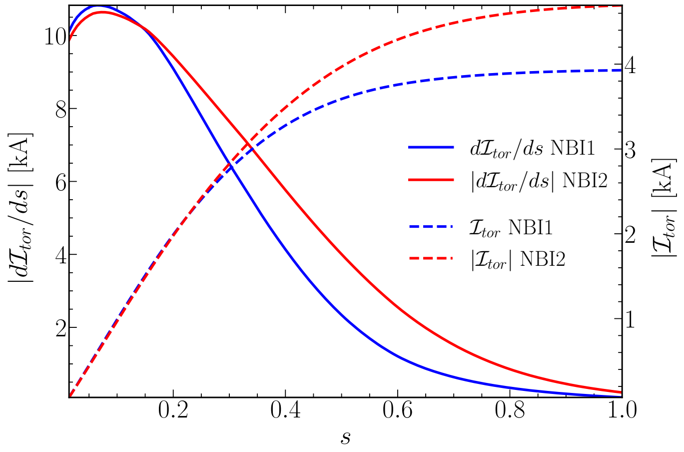

Figure 6.15: Toroidal current density profiles (solid lines) and integrated current (dashed lines) by for the lowest collisionality case and both co (red) and counter (blue) injected neutral beams.

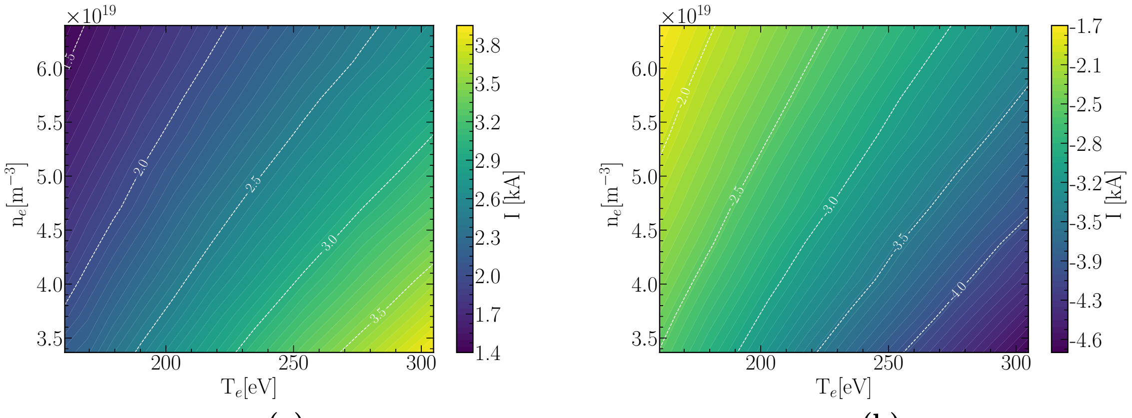

(a) **(b)**

Figure 6.16: Dependence of toroidal current created by NBI1 (a) and NBI2 (b) on plasma parameters.

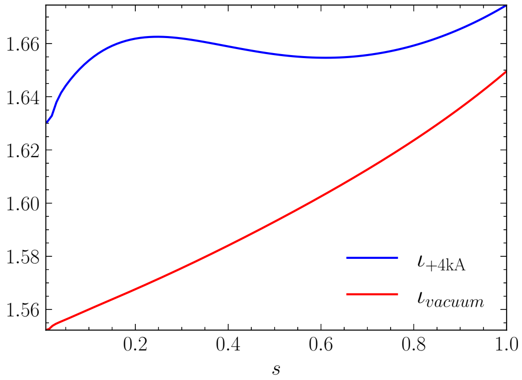

Figure 6.17: ι-profile of the standard magnetic configuration of TJ-II in vacuum and introducing the current profile of the high-density low-temperature case (+4 kA)

again caused by the lower level of prompt losses of NBI2. The electron response given by the $1 - A$ factor in equation (6.1) acts equally on both beams. The total integrated current, given by $I \equiv \mathcal{I}_{tor}(s = 1)$, is represented in figure 6.16. Assuming that the rest of contributions to the total toroidal current are the same whether we use NBI1 or NBI2, it can be observed that balanced injection at same power would not achieve fully compensated toroidal current ($I \approx 0$) since NBI2 systematically produces higher absolute values of the current for the same amount of port-through power injected. This can be explained again by the difference in the amount of prompt losses described in section 6.3. In figure 6.17, a comparison of the ι-profiles of the vacuum standard configuration of TJ-II and including a positive current profile. The effect of the positive current is increasing the rotational transform.

6.4.1 Radial fast-ion current

Another interesting quantity we can study for completeness is the perpendicular fast-ion current, which can be calculated from the parallel component

$$\mathbf{J}_\perp = \mathbf{J} - J_\parallel \hat{\mathbf{b}} \tag{6.3}$$

Since we can calculate **J** from the 6D distribution function given by ASCOT5 and, in the previous section, we have calculated $J_\parallel$, we can obtain $\mathbf{J}_\perp$ from (6.3). The perpendicular current is around two orders of magnitude lower than $J_\parallel$ and its distribution across the plasma cross section is completely different to that of $J_\parallel$. The values are plotted in figure 6.18.

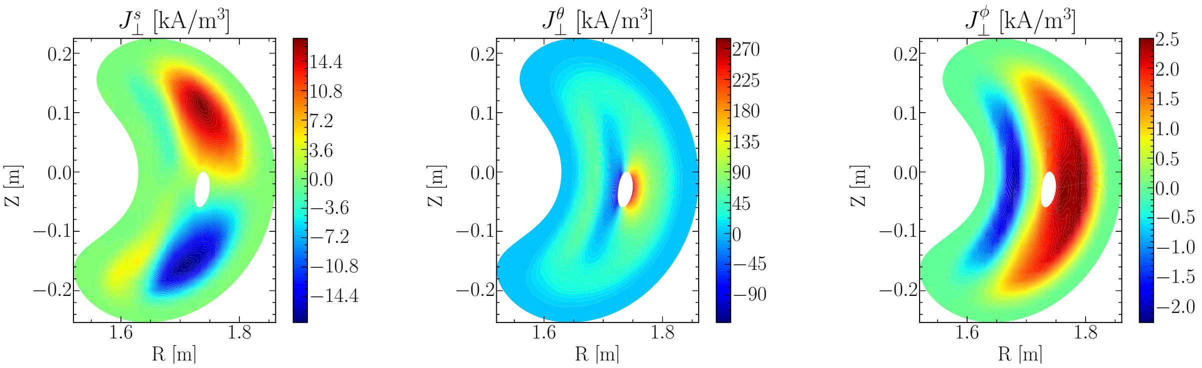

Figure 6.18: Components of $\mathbf{J}_\perp$ in VMEC coordinates for the low-density high temperature case.

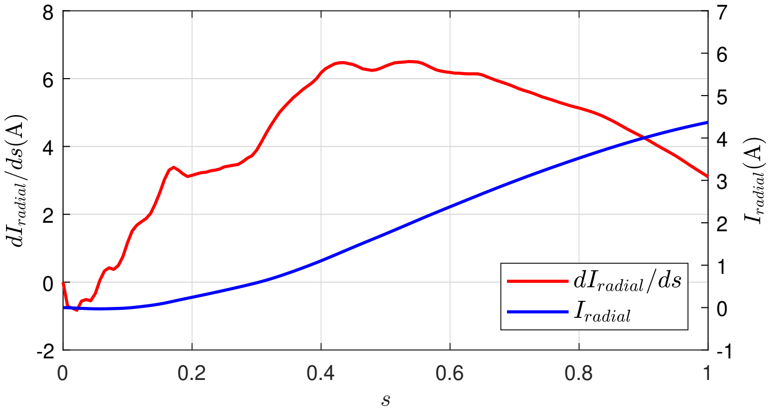

Figure 6.19: Radial profile of $\langle J_\perp^s \rangle$ and its radially integrated values.

Figure 6.18 shows that the three components of $\mathbf{J}_\perp$ present regions with positive and negative contributions, although not quantitatively symmetric. The VMEC coordinate system allows for an estimation of the radial fast-ion current density ($J_\perp^s = \mathbf{J}_\perp \cdot \nabla s$). In figure 6.19, the radial current flowing through the flux surfaces and its radial derivative are plotted. The radial current can be relevant for neoclassical calculations of E_r, since the outward flow of fast ions can induce an extra contribution to E_r comparable to the ambipolar value.

7. Experimental validation of NBCD in TJ-II

In this chapter, the theoretical model and numerical tools presented in chapters 5 and 6 will be tested against experimental results obtained in actual TJ–II plasmas. Specific sets of shots with stationary plasma profiles have been designed for the model validation. This guarantees that the source of driven current is roughly constant and that, once the externally driven inductive components are removed (see Appendix B), the time evolution of plasma current measured experimentally is only originated by the plasma self-inductive response to the internal current sources. Since the plasma current does not reach its steady-state value because the L/R time (τ_{LR}) can be comparable or even much larger than the shot duration, we need to fit the time trace of the plasma current to a shifted exponential, being the fitting parameters the saturation current (I^{exp}) and τ_{LR}. In order to explore the range of validity of the numerical results, different plasma scenarios have been studied: high-density NBI and low-density NBI+ECRH plasmas. In addition, a comparison of the shined-through power has been also performed. Although the simulations performed for this chapter are very similar to the ones in chapter 6, it is worth mentioning that, due to the more realistic character of the following results, the version of ASCOT5 used here includes the CX reactions, which are very relevant in the case of (low density) ECRH plasmas due to its low collisionality[1]. Another effect to consider for the experimental validation is that, in the absence of other sources of current, such as electron cyclotron current drive (ECCD), the measured plasma current is the combination of NBCD and bootstrap current. In order to isolate the NBCD, a determination of the bootstrap current has been done using the code DKES.

---

[1] Low-collisional plasmas, such as low-density and/or high-temperature plasmas, have longer slowing down times. This causes that CX reactions play a larger role.

NBI Parameters			
Injector	**#Shot**	**V$_{acc}$[kV]**	**PT Power [kW]**
NBI2	53577	29.5	477
	53605	27.1	324
NBI1	54097	27.8	286
	24000	32	430

Table 7.1: NBI parameters of the shots studied

7.1 Plasma scenarios

Four different plasma scenarios have been chosen for the validation: two NBI2+ECRH (#53577 and #53605), one NBI1+ECRH (#54097), and one pure NBI1 (#24000) shots

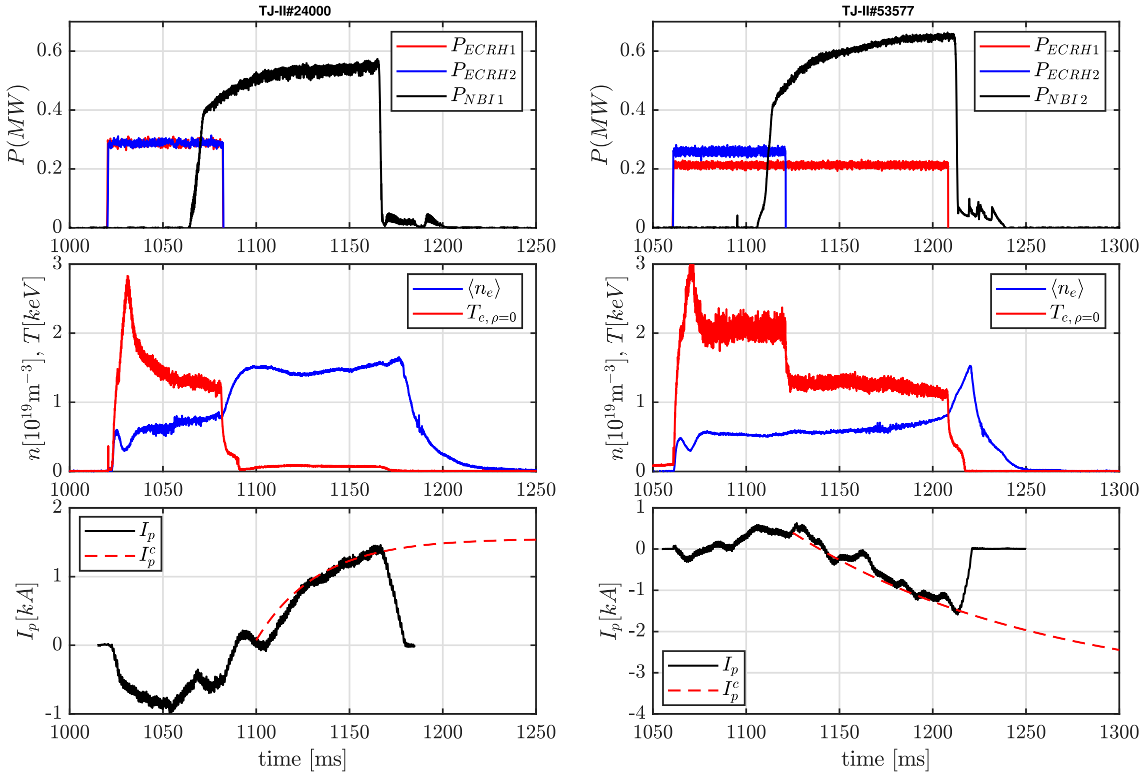

(a) **(b)**

Figure 7.1: (a) Time traces of the TJ–II shots #24000, and (b) #53577. For each shot: top panels show the injected ECRH and NBI powers; middle panels show the line averaged density and electron temperatures at the plasma center; and bottom panels show the plasma current together with the exponential fit.

with different NBI port-through (PT) powers and beam-acceleration voltages (V_{acc}) (these values are summarized in table 7.1). Ideally, it would be desired to have NBI-only heated plasmas (similarly to #24000) but the harsh density control in NBI plasmas prevents us from achieving this condition and ECRH must be used as a density actuator. The drawback of this approach is that the use of ECRH constraints us to low-density and high-electron-temperature plasmas. An attempt of achieving pure NBI plasmas was carried out during the days of the experiments unsuccessfully, even after a recent lithium+boron conditioning of the vacuum vessel. The time evolution of some significant quantities of two representative shots are plotted in figure 7.1.

7.2 Plasma profiles

The electron density and temperature radial profiles have been obtained from measurements of the Thomson scattering diagnostic and from the helium-beam and profile-reflectometry diagnostics.

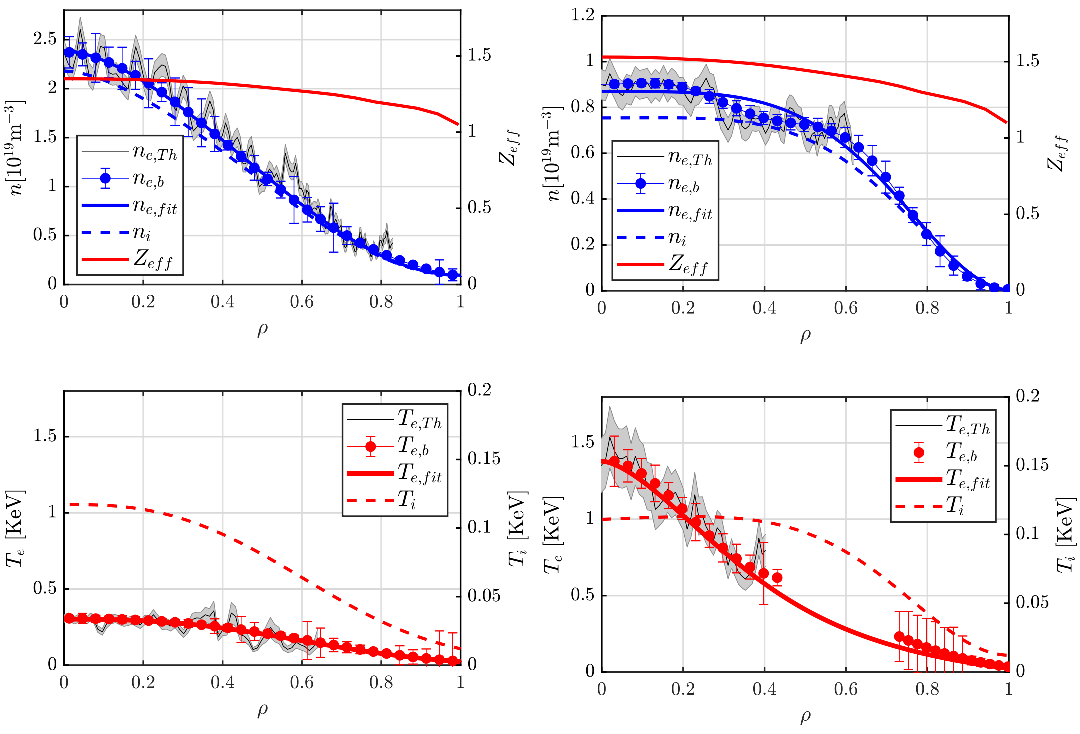

(a) **(b)**

Figure 7.2: (a) Kinetic profiles shots #24000, and (b) #53577 measured at $t = 1120$ ms.

The first one provides the profiles in the core and intermidiate regions of the plasma, while the other two are used for the external one. The experimental measurements of these diagnostics have been fitted to a smooth profile by means of a Bayesian method [49] and ensuring that the interferometric measured line-averaged density is consistent with the computed profile. The Z_{eff} profile is obtained from radiative measurements and the ion-density profile is deduced from the Z_{eff} and electron-density profiles. Likewise, the ion-temperature profile has been obtained from the core ion temperature given by the neutral-particle analyzer (NPA) accordingly to the method developed in [49]. The plasma profiles of the shots #24000 and #53577 are depicted in figure 7.2.

In the cases of the NBI+ECRH shots, the radial profiles of the electric field have been obtained from heavy-ion beam probe (HIBP) measurements and Doppler relectometry (DR) and both diagnostics give consistent results (see figure 7.3). The plasma potential (ϕ) provided by the HIBP has been fitted to a 5^{th}-grade polynomial ($\mathcal{P}_5$) from which the electric field has been calculated as

$$E_r(\rho) = -\nabla\phi = -\frac{d\phi}{d\rho}\left\langle\nabla\rho\right\rangle . \tag{7.1}$$

The raw data from the diagnostics showed no relevant differences between the three NBI+ECRH shots and only one representative case has been taken for the simulations. In the case of the pure NBI shot, only the DR measurement was available and the data have been fitted to a $\mathcal{P}_5$-curve that is everywhere negative (figure 7.4), which is a typical feature of NBI plasmas in TJ–II, unlike in low-density ECRH plasmas, where it is everywhere positive [50]. In addition to this behaviour, mixed situations can be found

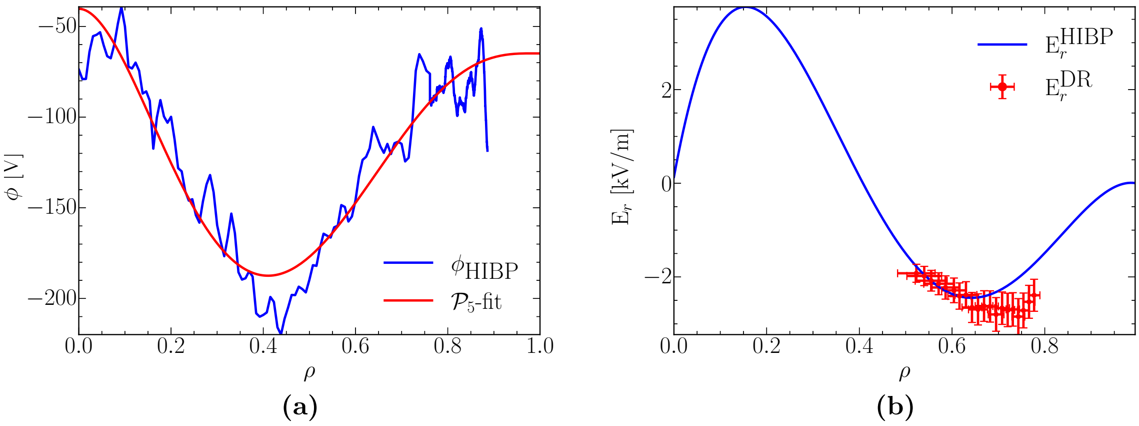

(a) **(b)**

Figure 7.3: Plasma potential measurements from HIBP and corresponding fit for the NBI+ECRH shots (a) and electric field accordingly to HIBP and DR measurement (b).

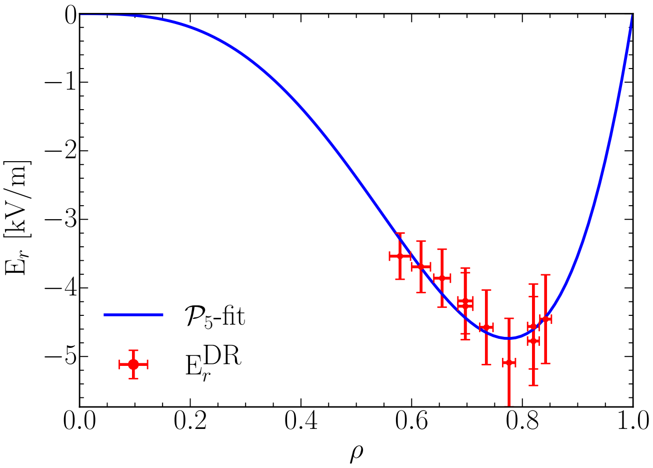

Figure 7.4: DR measurement and corresponding fit for the pure NBI shot.

in which the electric field changes its sign at some radial positions, as in our cases (see figure 7.3). Lastly, the profiles of thermal hydrogen neutrals have been calculated with the transport code ASTRA [51] (coupled to EIRENE) using the same plasma profiles described above and other transport parameters such as the confinement time or the recycling factor of the wall. The neutral densities show only slight differences between the different shots.

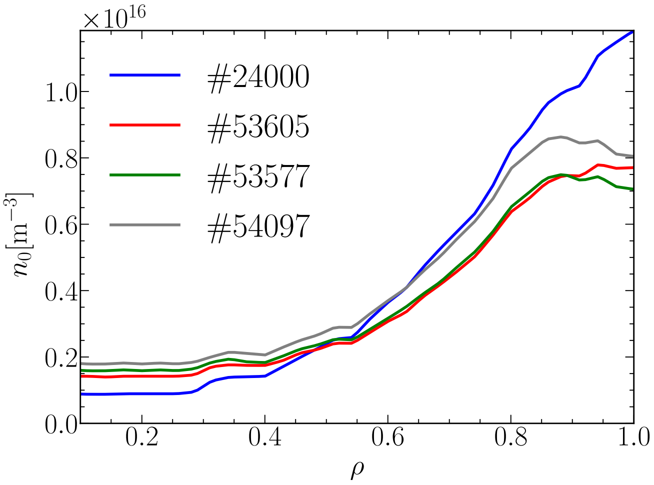

Figure 7.5: Neutral density profiles of the different shots as calculated by ASTRA.

7.3 Simulation results and validation

The simulation setups have been prepared as explained in chapter 4 and performed for the plasma scenarios presented in the previous section.

7.3.1 Shine through

The initial energy of the markers and PT powers of the simulation correspond to those of table 7.1 and the particle fractions have been obtained from spectroscopic measurements in the NBI ducts [52] being 38%, 30% and 32% for the energies $E_{max} = eV_{acc}$, $E_{max}/2$ $E_{max}/3$, respectively, for NBI1 and 48%, 24% and 28% for NBI2. From the results of the BBNBI simulations, we can estimate the power loads to the wall due to the shine through (ST) and compare with the measurements of an infrared camera (IRC) installed in TJ-II to perform thermographic measurements. The experimental values of the shine through have been calculated assuming that the temperature rise in the *beam dump* of the vacuum chamber due to a continuous injection of the NBI is given by

$$T(t) = T_0 + \frac{Q}{C(T)}\sqrt{t}, \tag{7.2}$$

where T_0 is the initial temperature of the target, Q is the heat flux, and $C(T)$ is a temperature-dependent coefficient specific of the material of the target [53]. The term $C(T)$ can not be estimated due to the uncertainty in the composition of the beam dump because of the recurrent treatment of the first wall with boron or lithium to avoid sputtering from the walls. To sort out this uncertainty, the expression used to obtain the ST-power fraction out of the injected power is

$$f_{ST} := \frac{Q^{shot}}{Q^{vac}} = \frac{T^{shot}_{max} - T^{shot}_0}{T^{vac}_{max} - T^{vac}_0}. \tag{7.3}$$

Here, the superscripts refer to the values measured either during the actual shot (shot) or during a calibration shot in vacuum (vac), see figure 7.6. The values obtained both with BBNBI and experimentally (by means of equation 7.3) are in close agreement and show to be quite high, specially in the low-density NBI+ECRH plasmas (see Table 7.2). In figure 7.7, images of the IRC at different times of the NBI1 pulse of shot #53605 are presented together with the ST-power loads as calculated by BBNBI.

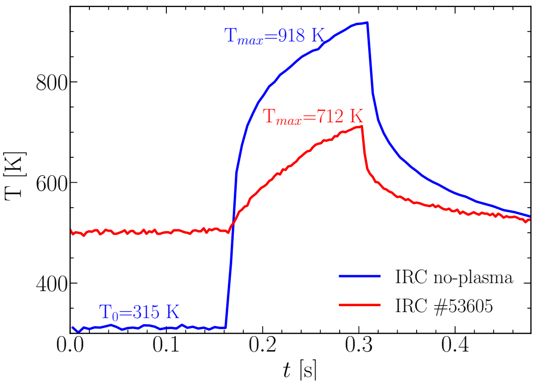

Figure 7.6: Beam-dump temperature from IRC signal during shot #53605 and a calibration shot without plasma. A high-temperature filter only only allowed measurements above 500 K in shot #53605. The initial temperature before the NBI pulses was 315 K.

Shined-Through Power [%]			
Injector	**#Shot**	**BBNBI**	**IRC**
NBI2	53577	70	67
	53605	67	66
NBI1	54097	71	-
	24000	54	49

Table 7.2: Shine-Through powers as calculated by BBNBI and measured with IRC. The IRC was not available for shot #24000.

7.3.2 Distribution function and power balance

The dynamics of fast ions taken into account in the simulations has three different contributions: the Hamiltonian motion due to the electromagnetic field, the slowing down and pitch-angle scattering produced by collisions with the bulk plasma, and the stochastic CX reactions. The relative importance of these mechanisms can produce quite different steady-state fast-ion distribution functions. At fixed available power, a more collisional plasma (lower and higher plasma temperatures and densities, respectively) would reduce the fast-ion density because of the earlier thermalization and more intense pitch-angle diffusion. Likewise, low fast-ion energies and high neutral densities would reduce the population of fast ions due to a strong diffusion of neutralization/reionization cycles by CX reactions. The computed fast-ion density profiles, $n_f(\rho)$, shown figure 7.8a, are approximately one order of magnitude lower than their corresponding plasma densities. The fast-ion densities are ordered accordingly to the available powers (see table 7.3)

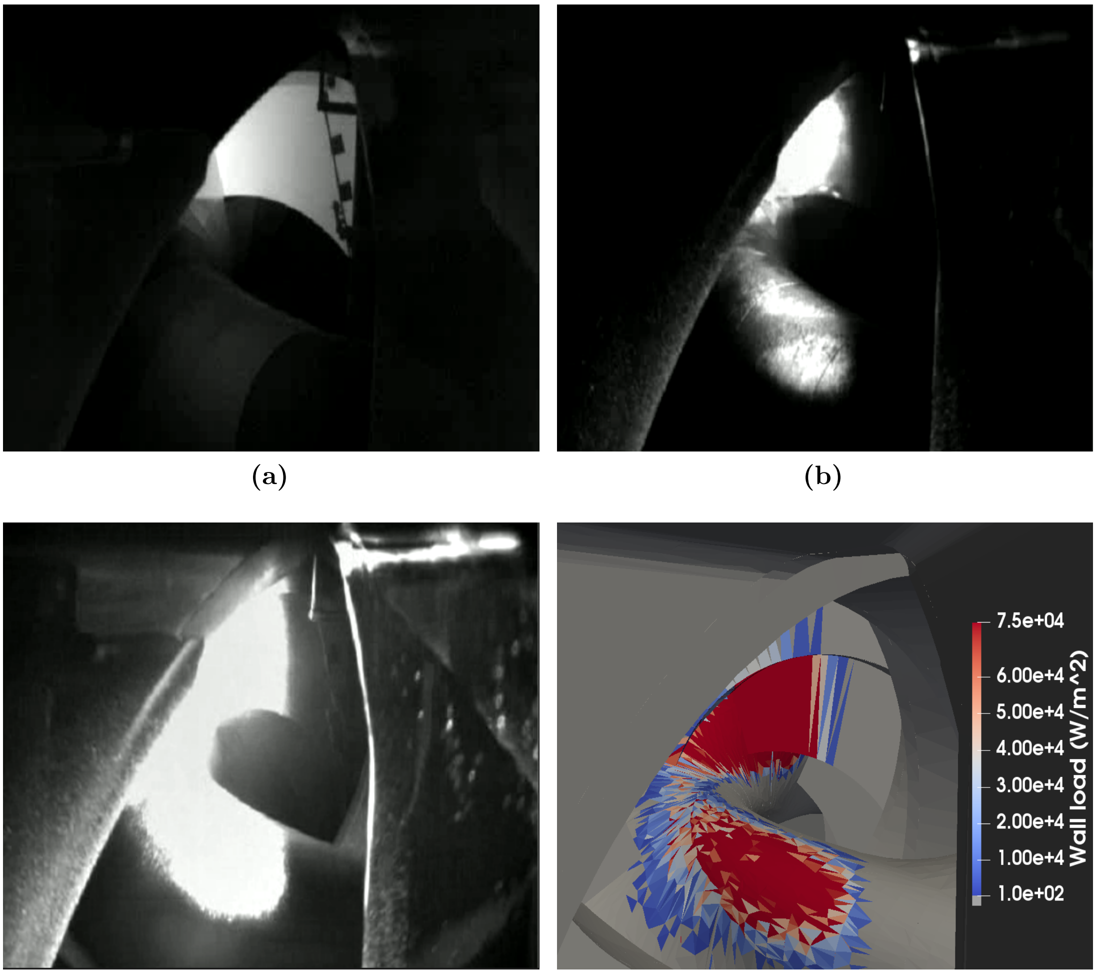

(a) **(b)**

(c) **(d)**

Figure 7.7: Images from the IRC at different times during the shot (top-left,top-right and bottom-left figures) and ST power loads as calculated from BBNBI (bottom right). The colorbar of the computed results have been saturated at $7.5 \cdot 10^4$ [W/m^2] to show clearly the distribution of the power over the first-wall elements, being the maximum value obtained in the simulation $5 \cdot 10^5$ [W/m^2]

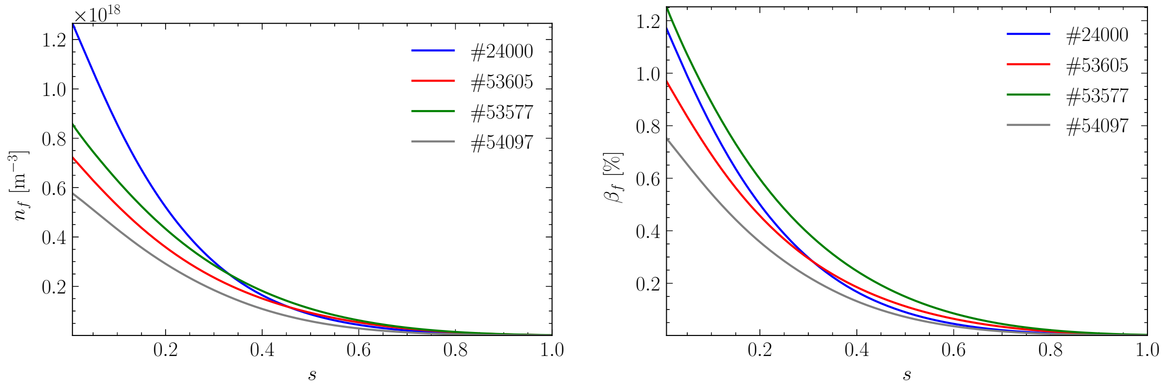

(a) **(b)**

Figure 7.8: (a) Fast-ion density and (b) fast-ion beta profiles, calculated by ASCOT5.

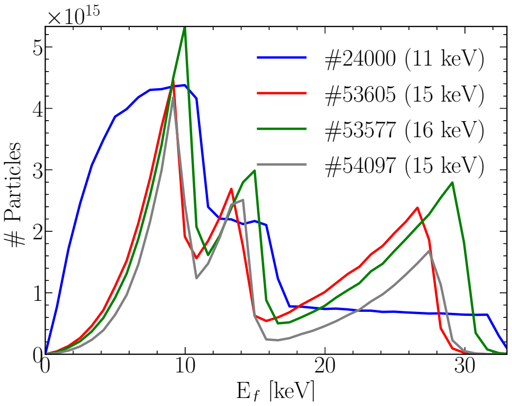

Figure 7.9: Fast-ion energy distributions. The numbers in parenthesis are the average energies of the distributions.

being shot #24000 the one with the highest fast-ion density despite being the most collisional plasma, as a result of the more efficient ionization of NBI neutrals due to the higher plasma density. On the contrary, this shot presents values of fast-ion pressure ($\beta_f = p_f/p_{mag}$, where $p_f = n_f E_f$ and $p_{mag} = \langle B^2\rangle/2\mu_0$ are the fast-ion pressure and the magnetic pressure respectively) similar to those of the other shots. The average energy of the fast-ion distribution of shot #24000 is lower than in the other shots (see figure 7.9), which compensates for the higher fast-ion density and results in β_f values closer (and even lower) to the ones obtained in the other shots. This lower average energy is caused by the presence of a larger amount of slowed-down particles in the distribution (e.g particles with energy below 10 keV), which are missing in the other shots due to the dominance of CX reactions. In fact, almost only newly born fast ions populate the distribution functions of the low density shots (notice the decay of the number of particles as energy decreases, starting at each of the injection energies of the NBI).

The balance between the available power (P_{av}) and the power distributed between the different channels is presented in table 7.3. Roughly, orbit losses (P_l) represent 10% of the available power in all cases, while 70% is lost by CX (P_{cx}), leaving a 20% for heating (P_h). The exception is shot #24000, for which only 28% of the available power is lost by CX and 58% is transferred to the thermal plasma. The reason for this is understood by examining the different neoclassical (orbits and collisions) and CX time scales, characterized by τ_{neo} and τ_{cx} respectively. According to the simulations results, $\tau_{neo} \sim 25$ ms is found for the NBI+ECRH plasmas and $\tau_{neo} \sim 10$ ms for the NBI shot, while $\tau_{cx} = [n_0 \sigma_{cx}(v) v]^{-1} \sim 1$ ms is obtained for a neutral density $n_0 = 10^{16}$ m^{-3} and a fast-ion energy (E$_f$) of 15 keV. At this energy the CX cross section is $\sigma_{cx} = 10^{-19}$ m^2 (see [54]). The smaller difference between time scales found in the NBI shot make up for the different behaviour in the mentioned power balance.

Power balance [kW]					
Injector	**#shot**	P_{av}	P_l	P_{cx}	P_h
NBI2	53577	144	12	103	29
	53605	109	10	74	25
NBI1	54097	86	6.5	64	16
	24000	203	28	58	117

Table 7.3: Distribution of available power between different channels.

7.3.3 Validation of NBCD calculations

In this section, the results of the toroidal plasma current are compared against the experimental measurement. There are two sources of current in these plasmas: bootstrap[2] (BS) and NBCD. The bootstrap current has been calculated with the code DKES for each shot and the radial profiles are presented in figure 7.10. The integrated values at the edge are always positive (same direction as the magnetic field) and smaller than 0.2 kA. The NBCD contribution (accounting for the current driven by the beam ions and the electron return current) has been calculated with the procedure followed in chapter

---

[2] Bootstrap current is produced by the neoclassical transport of the thermal plasma species (see [2, 55]).

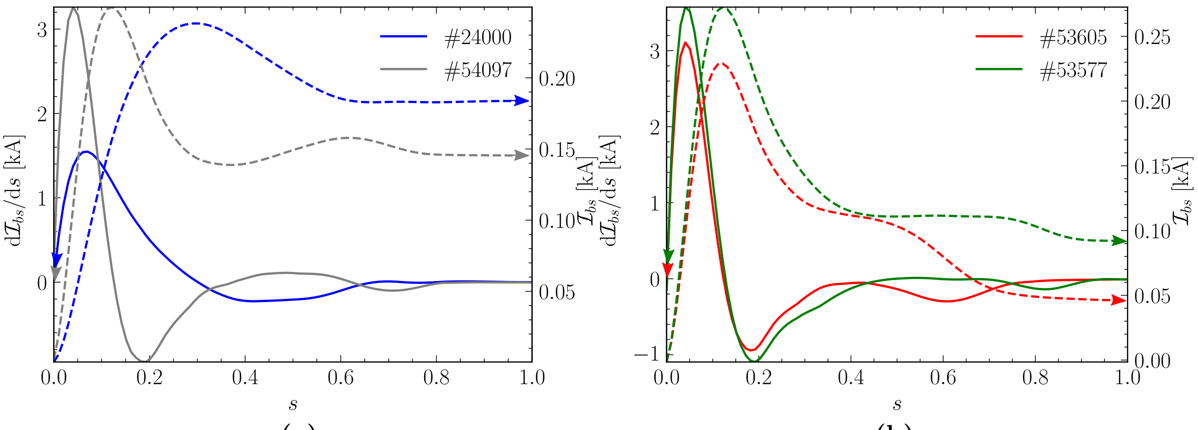

(a) **(b)**

Figure 7.10: (a) Bootstrap-current density and cumulative current for NBI1 shots and (b) NBI2 shots.

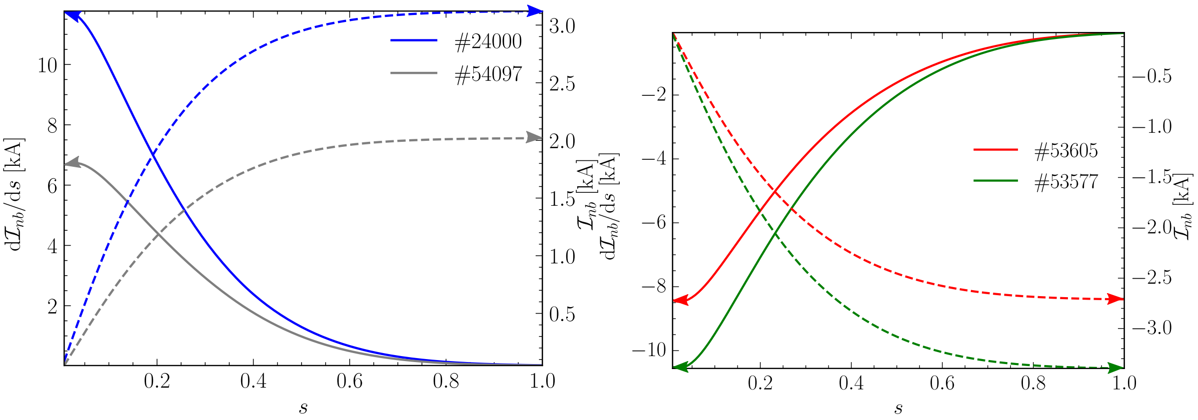

(a) **(b)**

Figure 7.11: (a) Fast-ion NBCD density and cumulative current for NBI1 shots and (b) NBI2 shots.

6 and the current profiles are plotted in figure 7.11. Furthermore, the corresponding errorbars have been also calculated by repeating the simulations with other different possible plasma profiles within the errorbars of the Thomson scattering diagnostic and a ±10% uncertainty in the neutral densities. The experimental values were obtained from the time traces of the plasma current measured by the Rogowski coils [28]. In TJ-II, the coupling of the magnetic-field coil currents and the plasma current is very intense due to the small separation between the plasma and the coils. This coupling produces oscillations in the plasma current (see bottom panels of figure 7.1)), which hidden the

Currents [kA]					
Injector	**#Shot**	$\mathcal{I}_{nb}(s=1)$	$\mathcal{I}_{bs}(s=1)$	$\mathcal{I}_{th}$	$\mathcal{I}_{ni}$
NBI2	53577	-3.5±0.4	0.1±0.1	-3.4±0.4	-3.5±0.4
	53605	-2.8±0.4	0.1±0.1	-2.7±0.4	-2.0
NBI1	54097	2.1±0.3	0.2±0.1	2.3±0.3	0.6±0.1
	24000	3.2±0.9	0.2±0.2	3.4±0.9	1.6

Table 7.4: Computed NBCD ($\mathcal{I}_{nb}$), bootstrap ($\mathcal{I}_{bs}$), and total ($\mathcal{I}_{th}$=$\mathcal{I}_{nb}$+$\mathcal{I}_{bs}$) currents evaluated at the plasma edge (s=1), and experimental current ($\mathcal{I}_{ni}$).

exponential trend that one would expect from a pure inductive response of the plasma to a non-inductive source of current (NBCD and BS in our case). Hence, a method to extract the inductive component out of the Rogowski signal has been developed (see Appendix B) and applied to our shots. In addition, errorbars have been obtained by calculating the experimental current in similar shots to the ones studied here when possible. The values of the contributions to the toroidal current from each source and for each shot have been collected in table 7.4 together with the experimental value. The total calculated toroidal current ($\mathcal{I}_{th}$) roughly agrees with the experiment ($\mathcal{I}_{ni}$) in the NBI2 cases. However, the experimental currents are around half the calculated ones for the NBI1 cases. The source of disagreement between codes and experiment for the NBI1 cases is still an open issue. The agreement between the BBNBI and IRC measurements implies that the discrepancy is not caused in during the injection phase (beam geometry or port-through power). This statement is also supported by the agreement of the results in the NBI2 cases. Actually, shots #54097 and #53605 have similar injected powers but very different plasma currents (0.6 and 2 kA, respectively), which indicates that NBI1 is effectively driving less current than NBI2.

A possible candidate that might cause the discrepancy is the Alfvén-eigenmode (AE) activity. Previous experience with AEs in TJ-II shows that NBI2 drives more activity than NBI1. On the one hand, the opposite signs of the currents driven by NBI1 and NBI2 result in divergent ι-profiles (NBI1 diminishes the vacuum values and NBI2 increases them) that, in turn, create a very different AE gap structure. In principle, one could argue that the gap structure of the NBI1 triggers the transport of fast ions out of the plasma but the accurate results for NBI2 (which presents more AE activity) makes us think that the effect of AE in the plasma current is minor. This can be investigated comparing the measurements of the fast-ion loss detector (FILD) in NBI1 and NBI2 shots. On the other hand, the absence of AE in NBI1 shots can be caused from a lower fast-ion pressure than in NBI2 shots, which lines up with the results obtained here. Another candidate is the presence of lithium in the vecinity of the NBI1 duct. The oven used for the lithium treatment of the wall is located right above the NBI1 duct, which causes that there is more deposition of lithium in this area. In this case, the deposits could be sputtered from the wall resulting in a high concentration of neutral lithium that could produce extra CX losses (no included in ASTRA or ASCOT5) and the reduction of the NBCD.

8. Fast-ion role in stellarator optimization

As it was introduced in section 1.3, the concept of stellarator reactors has numerous advantages with respect to tokamaks, such as their inherent steady-state operation and the absence of plasma disruptions. A successful reactor must provide a good confinement of the alpha particles created from fusion reactions, which will be responsible for heating the plasma by their slowing down. While ideal tokamaks present a perfect confinement of these particles due to their axisymmetry, the lack of that symmetry in stellarators makes alphas not to be inherently confined. This reduction of confinement would cause that alphas left the plasma region, causing strong damages to the plasma facing components and reducing the efficiency of the reactor.

Along with the good confinement of fast particles, a stellarator reactor must fulfill other optimization criteria such as MHD stability, small bootstrap current, and reduced neoclassical and turbulent transport. In order to find a magnetic configuration that satisfies such requirements, a process of optimization must be carried out. The central idea behind optimization is to take an already known magnetic configuration and minimize a cost function, which accounts for the the goodness of a given configuration in terms of the aforementioned criteria. This function is composed of proxies that quantify to what extent each of the criterion satisfies the required level of optimization. All the proxies have an associated weight. The minimization of the cost function is carried out with a genetic algorithm[1], which modifies the characteristic parameters of the initial equilibrium[2] within predefined limits randomly and evaluate the cost function. Should the result of the evaluation were smaller than the previous one, the modification is acquired as a new and improved equilibrium. This process is performed iteratively to find

---

[1] Steepest-descent methods are also used.

[2] Examples of these parameters are the shape and the toroidal magnetic flux of the LCFS, ψ_{LCFS} or the β-profile.

different families of new optimized configurations. The proxies are analytical expressions that, besides quantifying the criteria to optimize, they are required to be computed quickly, in order to make the optimization process computationally efficient. From the fast-particle perspective, the proxies used are related to prompt losses of alpha particles, which are the most dangerous losses for the reactor because particles leave the plasma in a much shorter time scale than the slowing-down time with their initial energy almost intact. Therefore, they are the main target of the fast-particle optimization. Prompt losses are associated to particles that are born as deeply-trapped, performing orbits with large radial excursions [56]. There are several proxies for prompt losses in the literature that have been implemented in optimization suites, e.g. STELLOPT [57], with satisfactory results such as γ_c [58], Γ_α [59]. However, they are based on radially-local approaches of the magnetic configuration, so they lack part of the detailed structure of the magnetic configuration and the (radially global) fast-particle orbits. Aditionally to prompt losses, there is another important loss channel that occurs at longer time scales, the so-called *stochastic losses* [60, 61]. These losses are associated to orbits that lay near the trapped/passing boundary region of phase space and the theoretical models of the proxies do not include the underlying physics of such mechanism. For these reasons, it is necessary to verify a posteriori the fast-particle confinement with orbit-following codes to confirm the good quality of the optimized configuration.

In this chapter, we revise the procedure for the quantification of fast-particle losses and the validation of a newly proposed proxy for prompt losses, Γ_α, developed at CIEMAT in different configurations of W7-X at different betas and a few new optimized magnetic configurations, developed also at CIEMAT, in chase of a candidate for a new and optimized experimental device. With this objective, we have taken advantage of the expertise with the ASCOT5 code acquired while carrying out the studies of the previous chapters to create the specific-purpose pre- and postprocessing tools required to pass from NBI-generated fast ions to the alpha-like initial particles needed for the evaluation of prompt losses in stellarators.

8.1 Fast-particle trajectories

Fast particles can be assorted in two different blocks: passing and trapped particles. Passing particles explore the whole flux surface at which they were born and, therefore, their radial drift averages out along their trajectories, so they are kept confined. On the contrary, trapped particles only move in a region of the flux surface and in general they experience a non-vanishing averaged radial drift. Consequently, the objective of the optimization procedure, regarding fast-particle confinement, is keeping trapped particles confined or reducing the presence of superbanana orbits as much as possible.

This section is devoted to present the relationship between the bounce-average motion of trapped fast particles and the second adiabatic invariant, $\mathcal{J}$, in collisionless magnetized plasmas, which is a very suitable formulation for understanding the dynamics and confinement of such particles (see for instance [56]). Let us express the magnetic field as (see section 1.1)

$$\mathbf{B} = \psi_{LCFS} \nabla s \times \nabla \alpha \tag{8.1}$$

Here, θ and ϕ are the poloidal and toroidal Boozer angles [62], respectively, and $\alpha = \theta - \iota\phi$. In such a field and in the absence of electric field, it can be demonstrated (see Appendix D) that the bounce-averaged radial and poloidal magnetic drifts relate to derivatives of $\mathcal{J}$ according to

$$\partial_\alpha \mathcal{J} = \frac{Ze\psi_{LCFS}}{m} \tau_b \overline{\mathbf{v}_M \cdot \nabla s} \tag{8.2}$$

$$\partial_s \mathcal{J} = -\frac{Ze\psi_{LCFS}}{m} \tau_b \overline{\mathbf{v}_M \cdot \nabla \alpha} \tag{8.3}$$

The second adiabatic invariant is defined as

$$\mathcal{J}(s, \alpha, v, \lambda) = 2v \int_{l_{b_1}}^{l_{b_2}} \sqrt{1 - \lambda B} dl \tag{8.4}$$

and

$$\tau_b = \frac{2}{v} \int_{l_{b_1}}^{l_{b_2}} \frac{dl}{\sqrt{1 - \lambda B}} \tag{8.5}$$

is the time it takes the particle to bounce once in the magnetic well (see figure D.1 in Appendix D), where v is the velocity, l_{b_1} and l_{b_2} are the bounce points, B is the magnetic field intensity and

$$\lambda = \frac{1}{B} \frac{v_\perp^2}{v^2}, \tag{8.6}$$

is the pitch-angle variable, where $v_\perp$ is the perpendicular velocity. The magnetic drift is

$$\mathbf{v}_M = \frac{mv^2}{Ze} \left(1 - \frac{\lambda B}{2}\right) \frac{\mathbf{B} \times \nabla B}{B^3} \tag{8.7}$$

and the overbar in equations (8.2) and (8.3) denotes the bounce-average operator, defined as

$$\overline{f} = \frac{2}{v\tau_b}\int_{l_{b_1}}^{l_{b_2}} \frac{f}{\sqrt{1-\lambda B}}dl. \tag{8.8}$$

According to equation 8.2, the net radial drift of a trapped particle in a single bounce time is proportional to the poloidal variation of $\mathcal{J}$. In collisionless orbits, trapped particles moves at constant $\mathcal{J}$ (see Appendix D). This implies that in magnetic configurations for which $\mathcal{J} = \mathcal{J}(s)$, at fixed v and λ, trapped particles will be confined, as they will only drift on their initial flux surface with the net poloidal velocity given by (8.3). The fields that satisfy this property are called *omnigeneous* [63]. The W7-X stellarator was design to be omnigeneous at $\langle\beta\rangle \gtrsim 3\%$ (see figure 8.1). However, such values of $\langle\beta\rangle$ have not been achieved yet and the experimental verification of fast-ion confinement in this device is still pending. Omnigeneity together with the condition that $\partial_s\mathcal{J} < 0$ is known as *maximum-*$\mathcal{J}$ property. In figure 8.1, it can be seen how the structure of $\mathcal{J}$ changes as $\langle\beta\rangle$ increases in the high-mirror (KJM) configuration of W7-X. Let us consider a particle born in the green regions of figure 8.1. As mentioned above, particles move at constant $\mathcal{J}$, so in the case of $\langle\beta\rangle = 0\%$, figure 8.1a, the particle will drift radially straight away (without precessing poloidally) and will leave the plasma quickly. On the contrary, in the case of $\langle\beta\rangle = 4\%$, figure 8.1d, the particle will mainly precess poloidally without net radial displacement. This confining precession will be directed counter-clockwise due to the maximum-$\mathcal{J}$ property.

8.2 Proxies for the evaluation of prompt losses of fast particles

A common proxy, introduced in [58], used for the optimization of quasi-symmetric configurations is Γ_c, which is defined as

$$\Gamma_c = \frac{\pi}{4\sqrt{2}}\left\langle \int_{B_{max}^{-1}}^{B^{-1}} d\lambda \frac{B}{\sqrt{1-\lambda B}}(\gamma_c^*)^2 \right\rangle \tag{8.9}$$

Here, B_{max} is the maximum value of B on the flux surface and

$$\gamma_c^* = \frac{2}{\pi}\arctan\frac{\overline{\mathbf{v}_M\cdot\nabla s}}{|\overline{\mathbf{v}_M\cdot\nabla\alpha}|}. \tag{8.10}$$

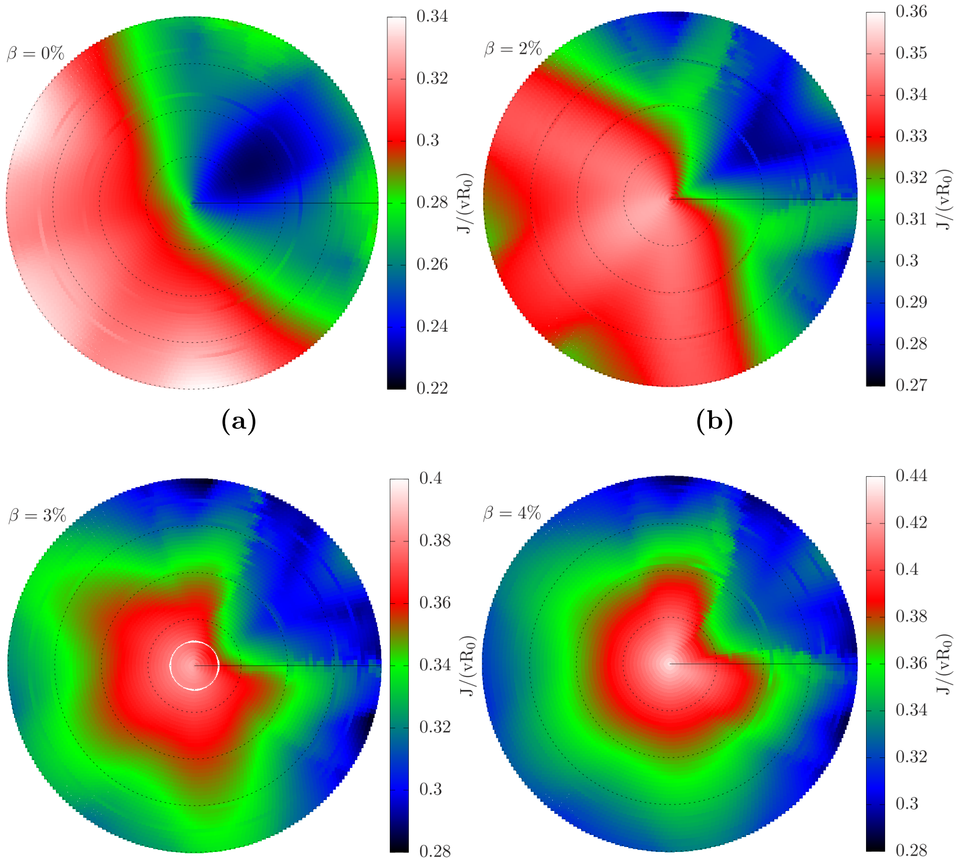

(a) **(b)**

(c) **(d)**

Figure 8.1: Contours of $\mathcal{J}/\nu R_0$ in (s,α)-space for the KJM configuration of W7-X at $\langle\beta\rangle = 0\%$ (a), $\langle\beta\rangle = 2\%$ (b), $\langle\beta\rangle = 3\%$ (c) and $\langle\beta\rangle = 4\%$ (d).

The quantity $\gamma_c^* \in [-1, 1]$ can characterize trapped-particle orbits. When $\gamma_c^* = 1$ or $\gamma_c^* = -1$ particles drift radially purely outwards or inwards, respectively. However, if $\gamma_c^* = 0$ they will not have radial drift at all. In figure 8.2, γ_c^* is plotted for different orbits at a few flux surfaces. The outward-drifting orbits are represented by red colors and the inward-drifting orbits by blue ones. It can be seen how the area with non-vanishing net radial drifts becomes smaller as $\langle\beta\rangle$ increases, which is consistent with the closure of the $\mathcal{J}$-contours seen in figure 8.1. Therefore, $\pi/2\sqrt{2}\Gamma_c \in [0, f_{trapped}]$ can be seen as a measure of the portion of phase space that have non-vanishing net radial drift. The Γ_c proxy has shown to provide good optimization of quasi-symmetric stellarators [64]. However, its use in helias configurations was not as successful [65]. In reference [59], a new proxy, $\Gamma_\alpha \in [0, f_{trapped}]$, was introduced and its results compared to Monte Carlo

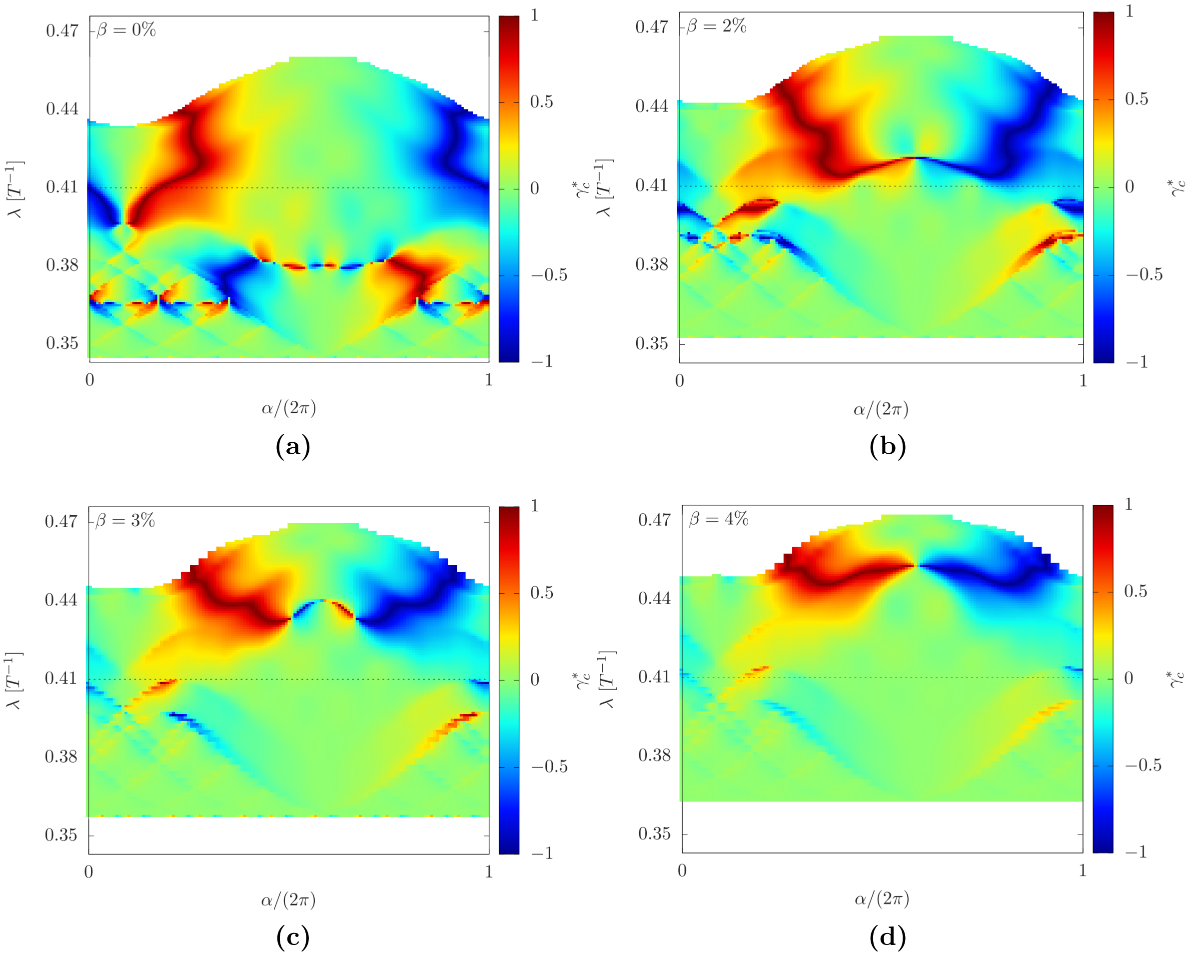

(a) (b) (c) (d)

Figure 8.2: Angular dependence of γ_c^* at s=0.25 for different trapped orbits in the KJM configuration of W7-X at $\langle\beta\rangle = 0\%$ (a), $\langle\beta\rangle = 2\%$ (b), $\langle\beta\rangle = 3\%$ (c) and $\langle\beta\rangle = 4\%$ (d).

full-orbit simulations performed with ASCOT5. The expression of this new proxy is

$$\Gamma_\alpha = \frac{1}{2}\left\langle \int_{B_{max}^{-1}}^{B^{-1}} d\lambda \frac{B}{\sqrt{1-\lambda B}} \Theta((\alpha-\alpha_{in})\overline{\mathbf{v}_M\cdot\nabla\alpha})\Theta((\alpha_{out}-\alpha)\overline{\mathbf{v}_M\cdot\nabla\alpha})\right\rangle, \tag{8.11}$$

where $\Theta(x)$ is the Heaviside function. The presence of the parameters α_{in} and α_{out} can be motivated inspecting the sketch of figure 8.1d, plotted in figure 8.3. The surface s_0 (dashed green line) has two regions with $\overline{\mathbf{v}_M\cdot\nabla s}\neq 0$: one close to α_{in}, where $\overline{\mathbf{v}_M\cdot\nabla s}<0$, and another close to α_{out}, where $\overline{\mathbf{v}_M\cdot\nabla s}>0$. A particle born in an α-region of s_0 such that $\alpha_{in}>\alpha$ and $\alpha>\alpha_{out}$ will follow the $\mathcal{J}$-contour precessing counter-clockwise ($\partial_s\mathcal{J}<0$) until α_{in}, when it will undergo an inwards radial excursion to later drift outwards in α_{out} and come back to its starting position. Therefore, the orbits of this α-region are confined. On the contrary, those of $\alpha_{in}<\alpha<\alpha_{out}$ will be quickly lost, since its $\mathcal{J}$-contour at

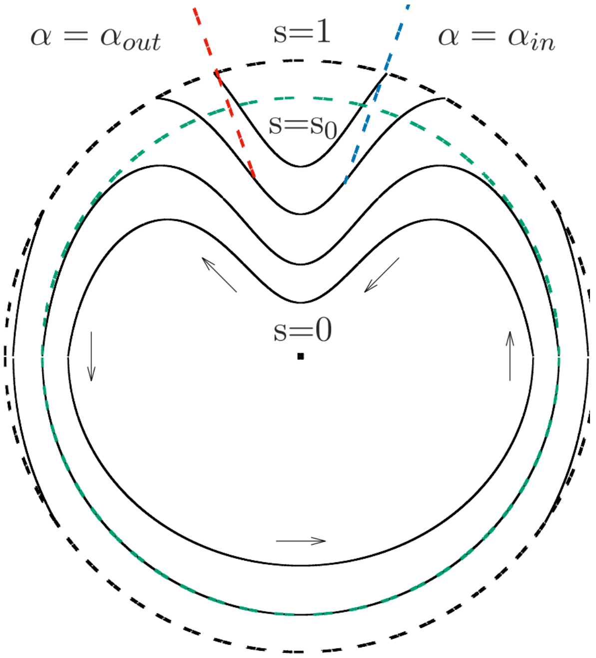

Figure 8.3: Sketch of the $\mathcal{J}$-contours of figure 8.1d. The red and blue lines represent the angular positions with outwards and inwards radial drifts, respectively

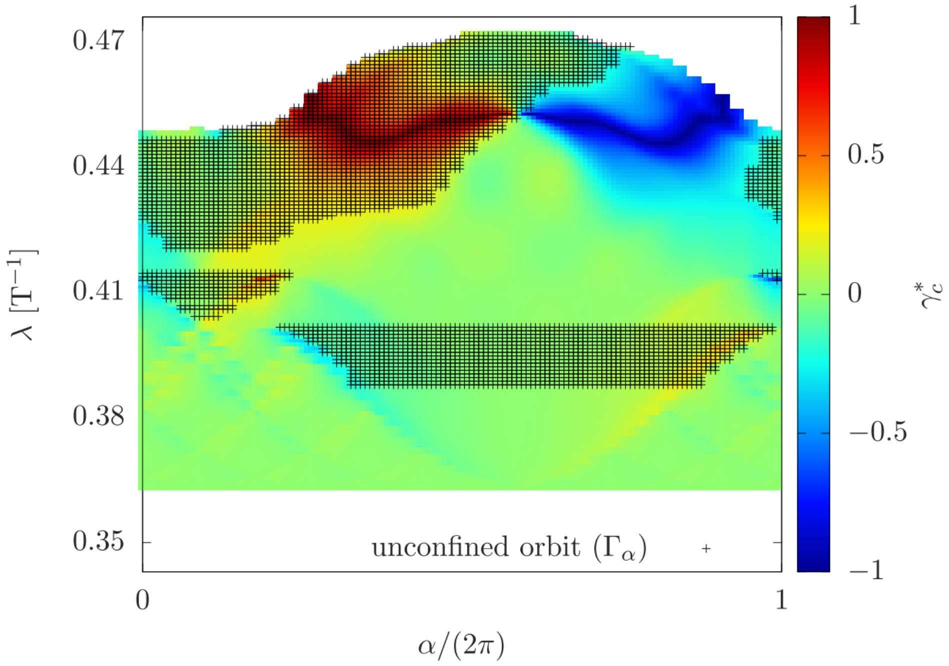

Figure 8.4: Orbits identified as unconfined by Γ_α (crosses) for the KJM configuration of W7-X with $\beta = 4\%$ at $s = 0.25$.

that region intersects the LCFS. The opposite behaviour of these trajectories is well captured by Γ_α. However, Γ_c will count them all as unconfined since it can not filter the trajectories that, besides moving radially, are still confined. A visual example of the characterization of the orbits given by Γ_α for the KJM configuration of W7-X can be seen in figure 8.4. The region that the model identifies as unconfined is represented with crosses. Clearly, Γ_c overestimates the amount of unconfined orbits since it considers both the reddish and blueish regions as unconfined.

8.3 Validation of the Γ_α model with ASCOT5

The magnitude commonly used to assess the performance of a magnetic configuration with respect to fast-particle confinement is the the fraction of initial particles that leave the plasma as a function of time (*loss fraction*). As it was mentioned in the introduction of this chapter, one of the key points of the stellarator reactor concept is the confinement of fusion alphas. Although the prospects of realizing a stellarator reactor are remote nowadays, the current experiments and the potential new ones must confirm the good confinement of fast ions in stellarators. Nevertheless, in such experiments, there will not be deuterium and tritium that react to produce alphas because of the complicated treatment of the reactants regarding nuclear safety. In adittion, the size of the experiments will be significantly smaller and with a substantially lower magnetic field, so the achievable plasma densities and temperatures will not be sufficiently high to produce relevant amounts of alpha particles even for deuterium plasmas. Yet, the assessment of the performance of the experiments with respect to alpha-particle confinement can be done by mimicking the behaviour of alpha particles in the magnetic configuration of the experiment with hydrogen particles.

Prompt losses occur at a time scale much smaller than the slowing down. Then, the behaviour of fast ions can be modeled by their collisionless trajectories and in absence of electric field, since for fast ions $\overline{\mathbf{v}_M \cdot \nabla\alpha} \gg \mathbf{v}_E$. In order to scale the alpha-particle trajectories of a reactor down to their analogous in an scaled experiment, we impose that the normalized Larmor radii are equivalent in both cases. Let the magnetic field, major and minor radii of a reactor be $B_r = 5$T, $R_r = 20$m and $a_r = 2$m, respectively. In such a field, the normalized Larmor radius of an alpha particle is

$$\rho_\alpha^* := \frac{\rho_\alpha}{a_r} = \frac{\sqrt{2E_\alpha m_\alpha}}{q_\alpha a_r B_r}. \tag{8.12}$$

Now, we consider an experimental device with $B_{exp} = 5$T, $R_{exp} = 2$m and $a_{exp} = 0.2$m. Then, the hydrogen ion that will mimick the alpha has to satisfy that $\rho^*_{alpha} = \rho^*_H$, which implies that the energy of the hydrogen is

$$E_H \approx \left(\frac{a_{exp}B_{exp}}{a_r B_r}\right)^2 E_\alpha = 36\text{keV}. \tag{8.13}$$

This energy scaling will be used in this chapter for both W7-X and the new optimized configurations.

8.3.1 Initial alpha-like fast-ion distribution

The spatial and velocity distributions of the alpha particles are both uniform, so must be the initial distributions of fast ions in the simulations. The spatial one is created by distributing the initial positions of the markers so that the marker density is uniform on a given flux surface (according to the Jacobian of the flux surface). Likewise, the velocity distribution of those markers is created uniformly distributing the vector directions in an unit velocity-space sphere to later scale the vectors with their modules in accordance to the marker's energy. In figure 8.5, an example of the distributions of 10^4 markers at 50 keV is shown in both real space (a) and in velocity space (b) for the surface $s = 0.25$ of the KJM configuration of W7-X.

8.3.2 Comparison between Γ_α and ASCOT5

The validation of Γ_α has been carried out with ASCOT5 for different configurations of W7-X. The markers used in the simulations correspond to hydrogen ions distributed in phase space as described in section 8.3.1 and with energy of 50 keV, which guarantees that the Larmor radius of the markers is similar to that of the alphas in a reactor-size W7-X. The maximum time evolution of the markers has been 0.1 s. This time is enough for the marker to perform as many toroidal turns as an alpha did during one slowing-down time in the reactor-size W7-X. The collisions and the electric field have been neglected in the simulations, as it was previously nentioned. The magnetic configurations of W7-X studied have been: standard (EIM), high-iota (FTM), low-iota (DBM), and a beta scan of KJM with values of 0%, 1%, 2%, 3%, 4%. The markers have been initialized on flux surfaces $s = 0.06$, 0.25, 0.5 for each configuration. Figure 8.6a, shows the loss fraction as a function of time for the beta scan calculated by ASCOT5 (lines) and the prediction of Γ_α (squares).

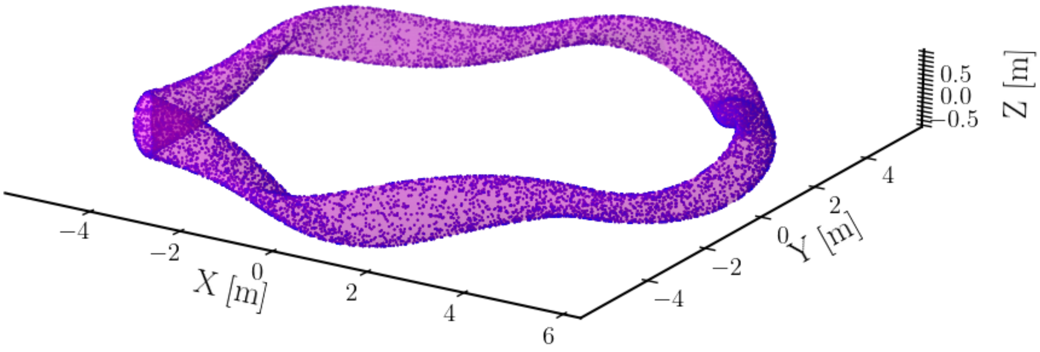

(a)

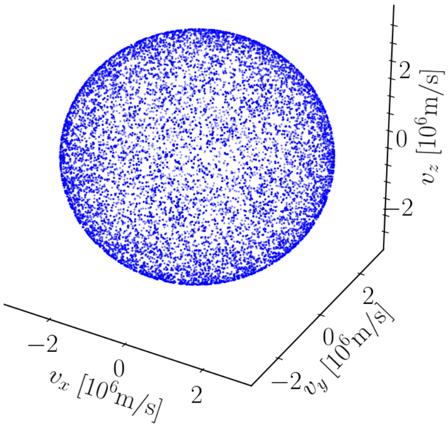

(b)

Figure 8.5: (a) Initial distribution of alpha-like hydrogen markers on the flux surface s=0.5 of W7-X in position space and (b) in velocity space

The first feature of the plot is the improvement of confinement at high beta as discussed in section 8.2. The second one is the two different time scales that appear for all beta values. There is a rapidly increasing amount of losses in the interval $10^{-4} \leq t \leq 10^{-3}$ s, corresponding to prompt losses, and a slower increase for $t > 10^{-3}$ s, stochastic losses. The values predicted by the model agree, even quantitatively, with the values of the simulations for the prompt losses. Some inaccuracy can be observed for low beta cases but it must be considered that the choice of the prompt-loss time ($t = 10^{-3}$ s) is slightly loose, since it is not clear where the initial slope of losses starts to flatten. In figures 8.6b and 8.6c, the loss fraction of ions born at each λ is represented as calculated by ASCOT5 and Γ_α, respectively. It can be seen how all λ values present losses and that the effect of increasing beta is reducing these losses both around the trapped/passing boundary ($\lambda = 1/B_{max}$) and the deeply trapped region ($\lambda = 1/B_{min}$). The results provided by Γ_α

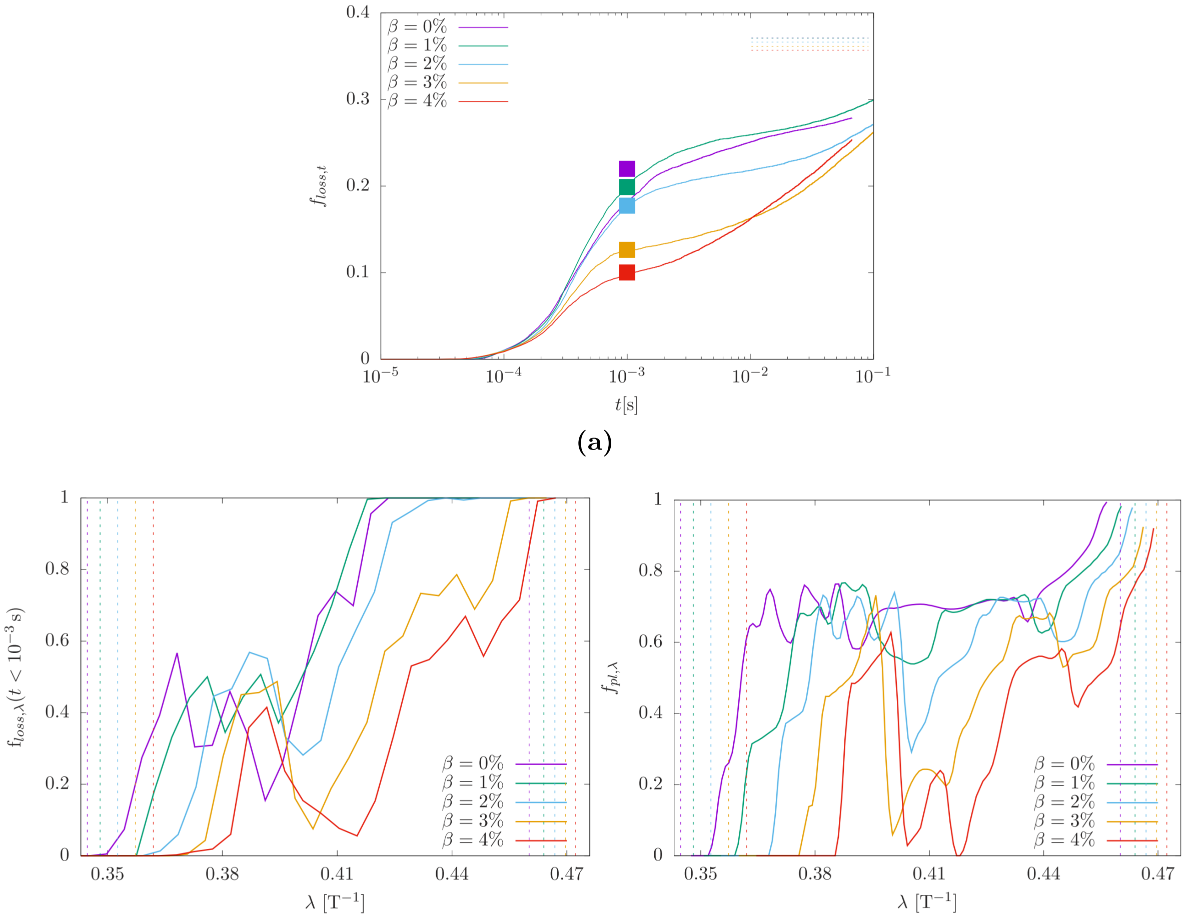

(a)

(b)

(c)

Figure 8.6: (a) Loss fraction as a function of time obtained with ASCOT5 (lines) and values predicted by Γ_α (squares). (b) Velocity-resolved loss fraction of markers born at s=0.25 calculated by ASCOT5 and (c) Γ_α. The dashed vertical lines represent the values $\lambda = 1/B_{min}$ (left) and $\lambda = 1/B_{max}$ (right) for each configuration.

show good qualitative agreement with those of ASCOT5.

In figure 8.7, the results of the proxies Γ_c and Γ_α (green and red dots, respectively) for the 8 configurations studied are plotted and compared to ASCOT5. Each row represents the amount of losses calculated with ASCOT5 in each of the flux surfaces of interest ($s = 0.06$, $s = 0.25$, $s = 0.5$) versus the values given by the proxies in the three flux surfaces, one for each column. From the figures in the diagonal (losses calculated by ASCOT5 versus the prediction of the proxies for each flux surface), we can see that the predictions of Γ_α are more accurate than those of Γ_c, the red dots are closer to the diagonal line, which tends to overestimate the losses. In the figures below the diagonal, we plot the losses calculated by ASCOT5 at a given flux surface versus the predictions of the proxies in outer surfaces. It can be observed that the predictions of the proxies still succeed qualitatively in predicting the loss fraction. This suggest that the properties ensuring fast-ion confinement are not radially local, but they are present at nearby surfaces. In addition, if we made a linear fit of the data for each proxy, we see that the values of the proxies on a given flux surface tend to zero faster than the ASCOT5 values at an inner flux surface, which confirms that the proxies (particularly the new Γ_α) can optimize in the surface on which they are evaluated and in inner surfaces at the same time. On the contrary, following the same reasoning, the plots over the diagonal, where the losses predicted by ASCOT5 at a given surface are plotted against the values of the proxies at inner surfaces, show that optimizing for a surface in general does not mean that the fast-ion confinement is conserved in outer surfaces. Consequently, this suggests that it is more efficient to optimize at outer surfaces.

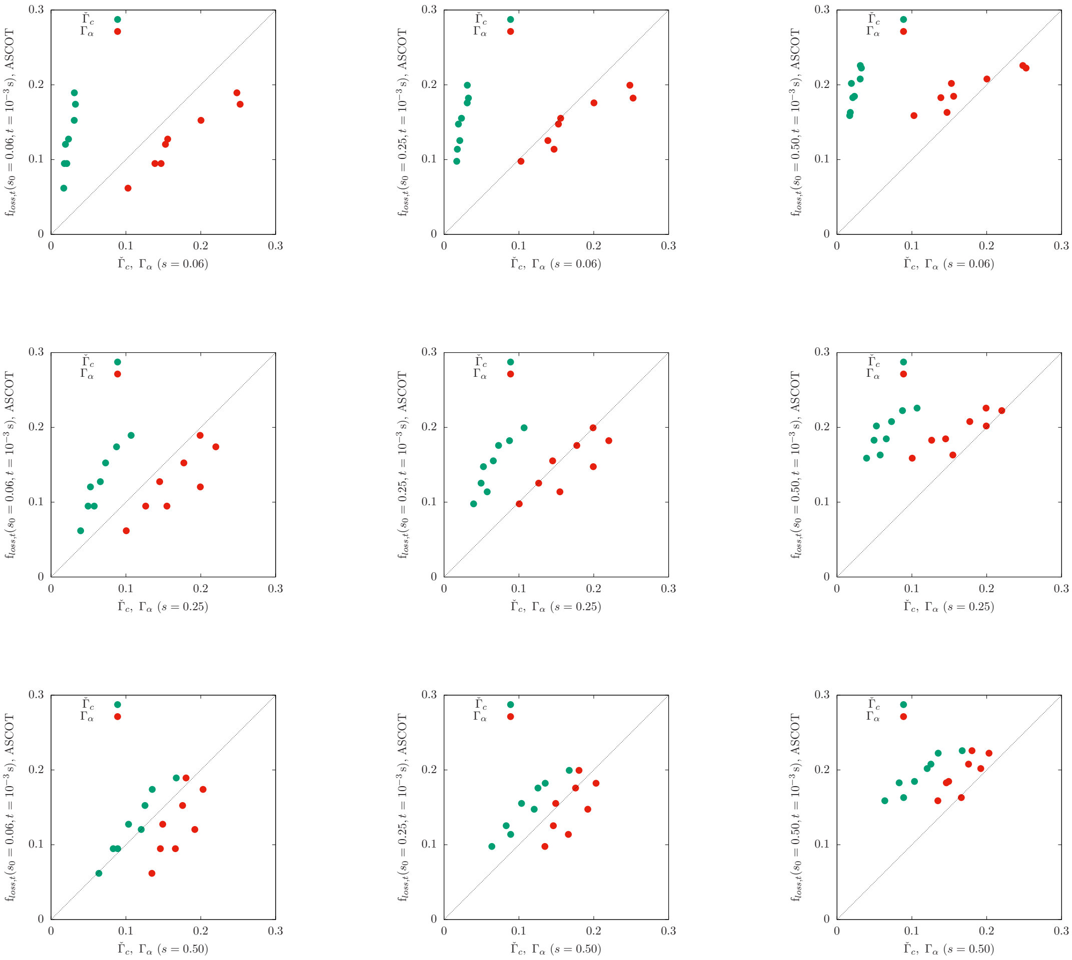

Figure 8.7: Comparison between the loss fractions calculated by ASCOT5 and Γ_α for different configurations and flux surfaces

8.4 Quasi-isodynamic configuration

The first steps to obtain an optimized magnetic configuration that fulfils the expected criteria for a stellarator reactor have been given using STELLOPT within the theory unit of the Laboratorio Nacional de Fusión (LNF).

Again, we have used the ASCOT5 code to confirm the good fast-ion confinement properties of the optimized configuration obtained with STELLOPT. The approach taken to find a suitable magnetic configuration has been focused on quasi-isodynamic (QI) configurations since, contrary to other configurations which exhibit other quasi-symmetries, the bootstrap current is expected to be small.

The best candidate found so far is a compact (A=9.94) 4-period magnetic configuration with reduced effective ripple ($\epsilon_{eff} < 0.5\%$), low magnetic shear, MHD stable up to $\beta \sim 5\%$, low bootstrap current and fast-ion losses below 2% at $\beta \geq 1.5\%$ in the plasma core. The shape of the LCFS, Poincare's plots of the LCFS and other two inner surfaces as well as the intensity of the magnetic field along a field line laying at s=0.06 are plotted in figure 8.8 (see reference [66] for further details).

8.4.1 Evaluation of fast-ion losses in the optimized configuration

The proxies included in STELLOPT regarding fast-ion transport are Γ_α, Γ_c. In order to validate the confinement of fast particles and to obtain a more accurate value not only for the fraction of prompt losses but also for stochastic losses, orbit-following simulations with ASCOT5 must be performed. Before performing such simulations, it is worthy examining the contours of $\mathcal{J}$ of the optimized configuration (figure 8.9). Even at medium beta ($\beta = 1.5\%$), the contours close on themselves and almost align with the flux surfaces. In addition, maximum-$\mathcal{J}$ property has been achieved at all poloidal positions. These characteristics indicate that the fast-ion confinement will be satisfactory. Here, we have followed the full-orbit trajectories of 40 keV hydrogen ions. The results of the loss fraction obtained for the optimized configuration for different flux surfaces and β are represented in figure 8.10, along with the KJM configuration of W7-X for comparison. The results show that indeed the loss fractions of this configuration are extremely low for $\beta = 1.5\%$ and $\beta = 4\%$ (specially at the inner flux surfaces) and considerably lower than the best case scenario of W7-X (KJM, $\beta = 4\%$).

The results presented so far correspond to fixed-boundary VMEC equilibria.

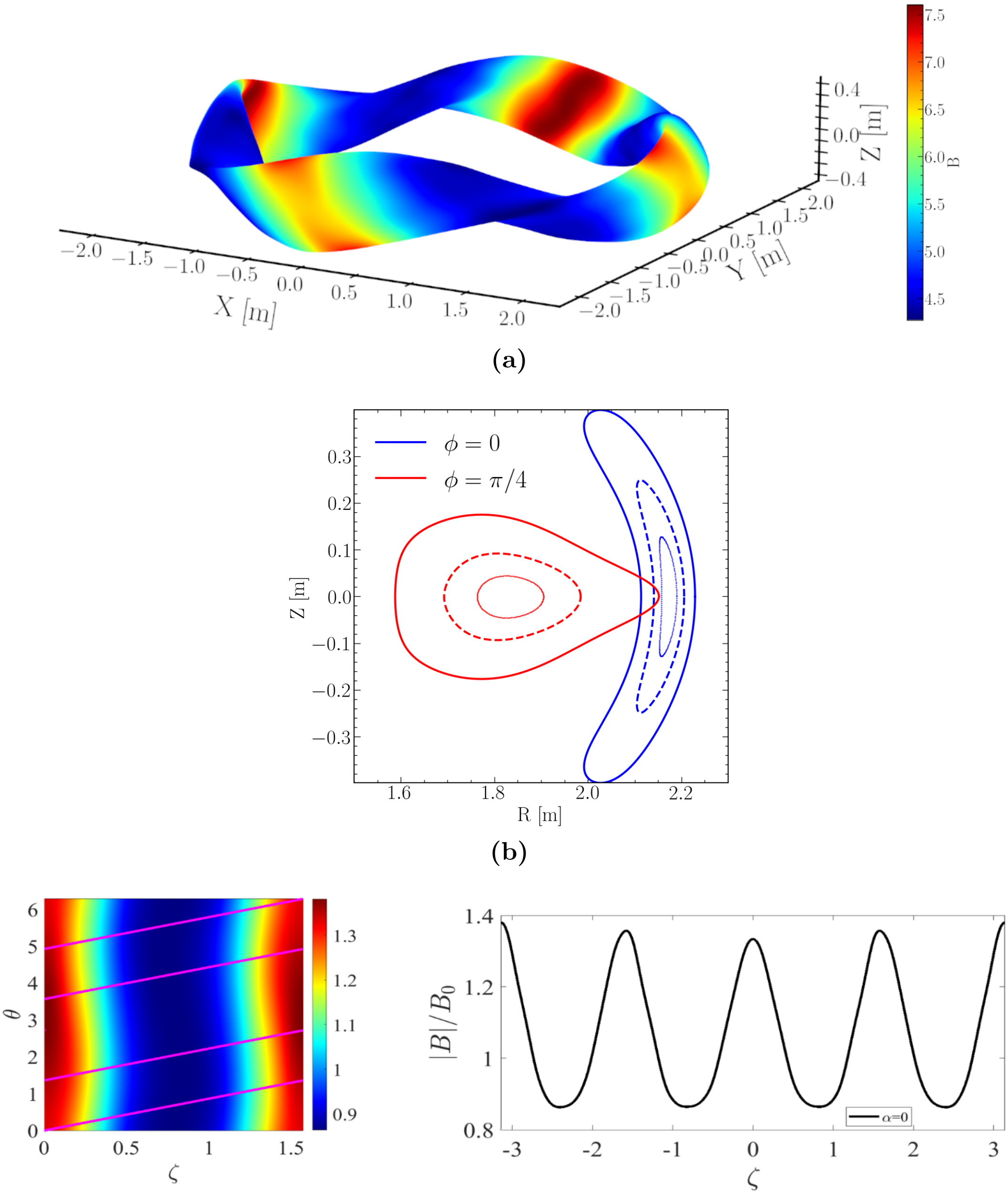

(a)

(b)

(c)

Figure 8.8: (a) Contours of B on the LCFS of the optimized configuration. (b) Poincare's plots of the surfaces s =0.06, 0.25, 0.5 at toroidal angles $\phi = 0$ (blue lines) and half period, $\phi = \pi/4$ (red lines). (c) Contours of B/B_0 on the surface $s = 0.06$ (left) and the same variable along the field line $\alpha = 0$ (right). This field line is represented in magenta on the left plot.

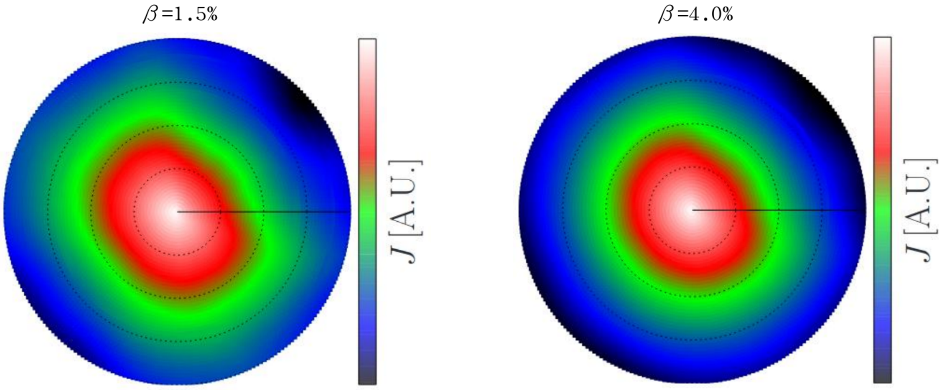

Figure 8.9: Contours of $\mathcal{J}$ for the optimized configuration at $\beta = 1.5\%$ (left) and $\beta = 4.0\%$ (right)

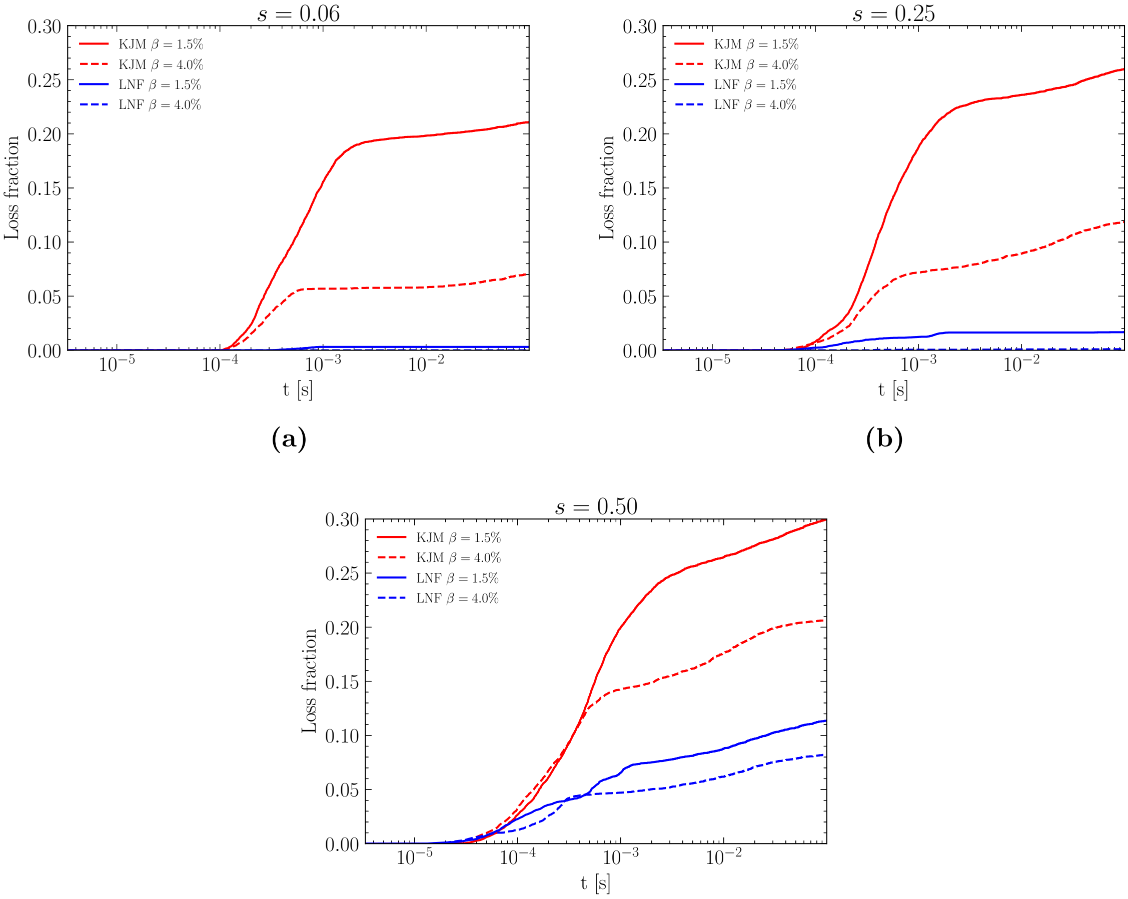

(a) **(b)**

(c)

Figure 8.10: Comparison of the loss fractions between the optimized (LNF) and W7-X high mirror configurations (KJM) for different flux surfaces and β values.

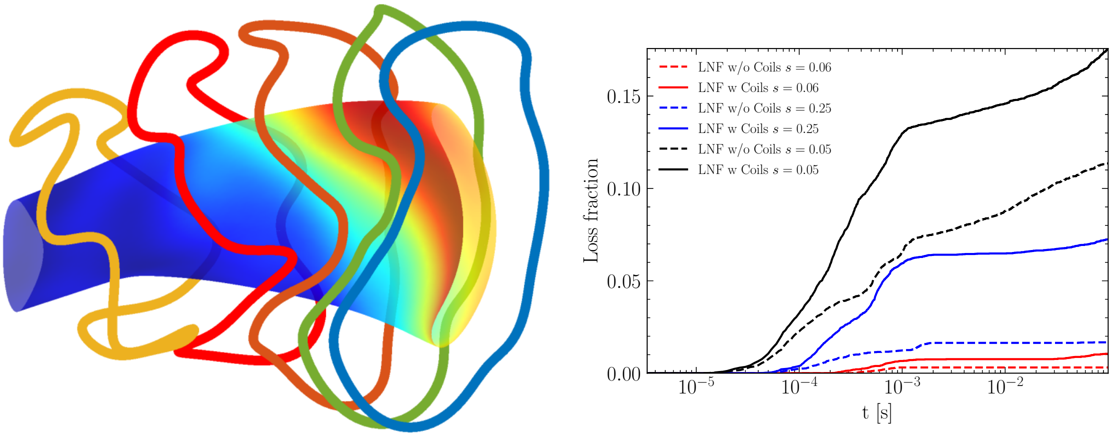

Figure 8.11: Filamentary coil model obtained with REGCOIL (left) and comparison of the loss fractions between the configuoodration with and without the coils.

This means that, despite having a magnetic configuration, we do not have a set of coils that can actually generate them. In general, the design of the magnetic coils for a given magnetic configuration it is quite cumbersome. Firstly, the discrete arrangement of the coils increases the effective ripple, which worsens the fine confinement of particles obtained with the optimization procedure. Secondly, the number of coils must be suffiently low so as to leave space in the vacuum chamber to place enough ports for diagnostics and heating systems. Thirdly, if the shapes of the coils are very intrincated, their construction might turn to be unfeasible from both the mechanical resistance and economic considerations. This problem has been tackled with the code REGCOIL [67], which can generate filamentary models of the coils suitable for a given equilibrium. The best set of coils obtained so far is composed of 5 different coils per semi-period (see figure 8.11a). In order to check to what extent fast-particle confinement has been affected by the presence of the discrete coils, we have performed again the ASCOT5 simulations. In figure 8.11b, we can see that the loss fraction in the configuration with coils has indeed increased but they have been kept at very reasonable ($\lesssim 5\%$) levels in the core regions of the plasma.

9. Discussion and outlook

The methods and results presented in this thesis have been aimed at studying fast-ion physics in stellarators making use of the state-of-the-art Monte Carlo code for particle tracing in fusion devices ASCOT5. Although ASCOT has been previously used extensively to characterize the fast-ion distribution functions and fast-ion losses in magnetic-confinement devices, it has been the latest version of the code, ASCOT5, the one used for this work.

This thesis presents the most extensive work on fast-ion physics performed so far with ASCOT5 in stellarators and, in particular, it has been the first time that this code has been used to model fast ions in TJ-II. Therefore, the thesis has required the setup of the complete models of TJ-II and its NBI systems, in the appropriate format, from scratch. Furthermore, new post-processing routines have been developed to estimate different quantities related to fast ions in stellarators.

In the case of TJ-II, an analysis of the fast-ion populations created by both NBI systems (co and counter) was performed. In particular, the shine through, available power, the 3D structure of the fast-ion densities (alongside their radial profiles), energy and pitch distributions, power deposited in the plasma and NBCD have been estimated for a wide range of accessible plasma densities and temperatures in TJ-II. What is more, the estimation of the NBCD has required reviewing the theoretical concepts and models needed to account for the electron response of the plasma to the NBI. These macroscopic observables have not been only estimated but also validated against experimental results from designed experiments in TJ-II, which serves as a proof of the reliability of the code and the methods used from the point of view of fast-ion modelling and code validation.

In parallel to the studies in TJ-II, the ASCOT5 code has been also exploited for performing calculations of fast-ion prompt losses in optimized stellarator configurations, which is a cutting-edge topic in the development of stellarators as a reactor concept. Specifically, we have calculated the prompt-loss fraction of fast ions with ASCOT5 and validated a new proxy for this quantity. The impact of this study relies on the fact that the proposed new proxy has proven to be more precise than others, while being still fast enough to be computed within an optimization-suite loop. In addition, both the new proxy and ASCOT5 have been used to assess the good confinement of fast ions of a new magnetic configuration that might serve as a candidate for a new stellarator device at LNF.

It is worth mentioning that this thesis has required work on several aspects of the fusion field that are normally tackled individually: coding, theory and experiments. This makes the studies complete enough for a PhD thesis, yet, there is still room for improvement. From the point of view of code validation, a natural way to continue this research line is making a complete comparison of the results from ASCOT5 with as many fast-ion diagnostics as possible that guarantees, without any source of doubt, the reliability of the code in all aspects. In this sense, TJ-II and its diagnostic systems (IRC, FILD, NPA, MSE, HIBP, magnetic diagnostics, etc) are perfect for this kind of studies. Furthermore, including new fast-ion physics, such as AE interaction with fast ions, is an unexplored possible source of information about fast-ion confinement in stellarators. This is a study that can be already done with ASCOT5, together with other MHD-stability codes such as FAR3D.

Beyond the particular results presented in this work, the methods and tools developed are general enough so as to be directly extensible to any magnetic configuration. In fact, they are open to the community with the aim of being used as a starting point to carry out further fast-ion studies in 3D magnetic configurations beyond (or complementaryly to) the ones presented here.

The quality of the scientific results presented here is supported by the four peer-to-peer publications in the well-known journal Nuclear Fusion (JCR-Q1) in which this thesis has played a crucial role.

A. Linearized collision operator

A detailed description of the linearized collision operator is given in [14]. Here, we present the explicit expresssions used for the calculations of chapter 5.
For electron-electron collisions, we take the model operator

$$C_{ee}^{(\ell)}[g_e] = \nu_{ee}\left(\mathcal{L}[g_e] + \frac{m_e v_{||} u_e}{T_e} f_{Me}\right), \tag{A.1}$$

where

$$\mathcal{L}[g_e] = \frac{2v_{||}}{v^2 B}\partial_\lambda\left(v_{||}\lambda\partial_\lambda g_e\right) \tag{A.2}$$

is the Lorentz operator,

$$\nu_{ee}(v) = \frac{3\sqrt{\pi}}{4\tau_{ee}}\,\frac{\phi\left(v\sqrt{m_e/(2T_e)}\right) - G\left(v\sqrt{m_e/(2T_e)}\right)}{\left(v\sqrt{m_e/(2T_e)}\right)^3} \tag{A.3}$$

is the electron-electron collision frequency, $\tau_{ee} = 6\sqrt{2}\pi^{3/2}\epsilon_0^2 m_e^{1/2} T_e^{3/2}/(e^4 n_e \ln\Lambda_{ee})$, $\ln\Lambda_{ss'}$ is the Coulomb logarithm for collisions between species s and s', ϵ_0 is the vacuum permittivity,

$$\phi(x) = \frac{2}{\sqrt{\pi}}\int_0^x e^{-y^2}\mathrm{d}y \tag{A.4}$$

and

$$G(x) = \frac{\phi(x) - x\phi'(x)}{2x^2}\,. \tag{A.5}$$

In (A.1), u_e is determined by imposing momentum conservation on electron-electron collisions,

$$\int v_{||} C_{ee}^{(\ell)}[g_e] = 0, \tag{A.6}$$

giving

$$u_e = \frac{\int \nu_{ee} v_{||} g_e \mathrm{d}^3 v}{\int \nu_{ee} (m_e v_{||}^2 / T_e) f_{Me} \mathrm{d}^3 v} \,. \tag{A.7}$$

Assume an ion species I such that $\sqrt{m_e/m_I} \ll 1$ and $v_I \ll v_{te}$, where v_I is a characteristic velocity of the ions and m_I is the ion mass. Assume also that the electron distribution can be expanded around a Maxwellian distribution. Then, one can prove that

$$C_{eI}^{(\ell)}[g_e] \simeq \nu_{eI} \left(\mathcal{L}[g_e] + \frac{m_e v_{||} V_{I||}}{T_e} f_{Me} \right) , \tag{A.8}$$

where

$$\nu_{eI}(v) = \frac{2 n_I}{m_e^2 v^3} \frac{2\pi Z_I^2 e^4 \ln \Lambda_{eI}}{(4\pi\epsilon_0)^2} \,. \tag{A.9}$$

To obtain (A.8), one does not need to expand the distribution function of the ions around a Maxwellian distribution. Hence, we can use expression (A.8) for both, thermal ions and beam ions. That is, we take

$$C_{ei}^{(\ell)}[g_e] = \nu_{ei} \left(\mathcal{L}[g_e] + \frac{m_e v_{||} V_{i||}}{T_e} f_{Me} \right) , \tag{A.10}$$

with

$$\nu_{ei}(v) = \frac{2 n_i}{m_e^2 v^3} \frac{2\pi Z_i^2 e^4 \ln \Lambda_{ei}}{(4\pi\epsilon_0)^2} , \tag{A.11}$$

$$C_{ez_k}^{(\ell)}[g_e] = \nu_{ez_k} \left(\mathcal{L}[g_e] + \frac{m_e v_{||} V_{z_k||}}{T_e} f_{Me} \right) , \tag{A.12}$$

with

$$\nu_{ez_k}(v) = \frac{2 n_{z_k}}{m_e^2 v^3} \frac{2\pi Z_{z_k}^2 e^4 \ln \Lambda_{ez_k}}{(4\pi\epsilon_0)^2} \tag{A.13}$$

and

$$C_{eb}^{(\ell)}[g_e] = \nu_{eb} \left(\mathcal{L}[g_e] + \frac{m_e v_{||} V_{b||}}{T_e} f_{Me} \right) \tag{A.14}$$

with

$$\nu_{eb}(v) = \frac{2 n_b}{m_e^2 v^3} \frac{2\pi Z_b^2 e^4 \ln \Lambda_{eb}}{(4\pi\epsilon_0)^2} \,. \tag{A.15}$$

Lastly,

$$\ln \Lambda_{ss'} = \ln \left(\frac{\lambda_D}{b_{cl}} \right) \tag{A.16}$$

where the Debye's length, λ_D, and the classical impact parameter, b_{cl}, are defined as

$$\lambda_D = \sqrt{\frac{\varepsilon_0 T_{s'}}{n_{s'} q_{s'}^2}}; \qquad b_{cl} = \frac{q_s q_{s'} (m_s + m_{s'})}{4\pi\varepsilon_0 m_s m_{s'} (v_s^2 + v_{s'}^2)} \tag{A.17}$$

B. Experimental determination of plasma current and LR-time

In TJ-II, the time traces of the plasma current, measured by a Rogowski coil, exhibit large oscillatory deviations from the typical exponential behaviour expected from non-inductive sources (such as bootstrap, ECCD or NBCD) observed in other devices [68–70]. The currents of the vacuum-field coils present two superimposed oscillations at low and high frequency (see figure B.1). These oscillations and the proximity of the coils to the

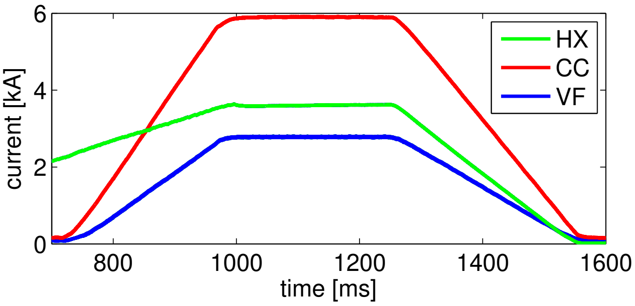

(a)

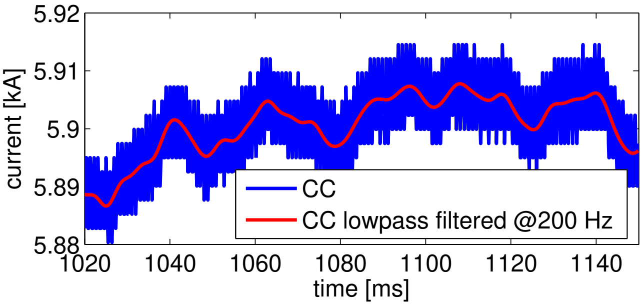

(b)

Figure B.1: Time traces of the different coil currents (a) including current ramp-up and ramp-down. Enlarged view of the current evolution in the central coil (b). Applying a low pass filter helps separate high and low frequency contributions.

plasma (see figure B.2) produce a non-negligible inductive current in the latter. Should the plasma and the coils be described by a circuital model, the time evolution of the measured plasma current (I_P) is governed by

$$\tau_{LR}\frac{dI_P}{dt} + I_P = \sum_i \mu_i \frac{dI_c^i}{dt} + I_{NI} \tag{B.1}$$

where I_c^i are the coil currents, I_{NI} is the current due to non-inductive sources. Being R_P the plasma resistance and L_P the plasma self-inductance, the time constant is defined as $\tau_{LR} := L_P/R_P$ and the induction coefficients as $\mu_i := M_i/R_P$, where M_i are the inductive coupling coefficient between the plasma and the vacuum-field coils. Although the inductive oscillations of $I_P(t)$ could be calculated using the coefficients μ_i, the unknown finite-volume distribution of I_P in the plasma prevent us from obtaining a reliable estimate. Instead, a minimization procedure has been applied to find the appropriate values of the coefficients so that equation B.1 is fulfilled.

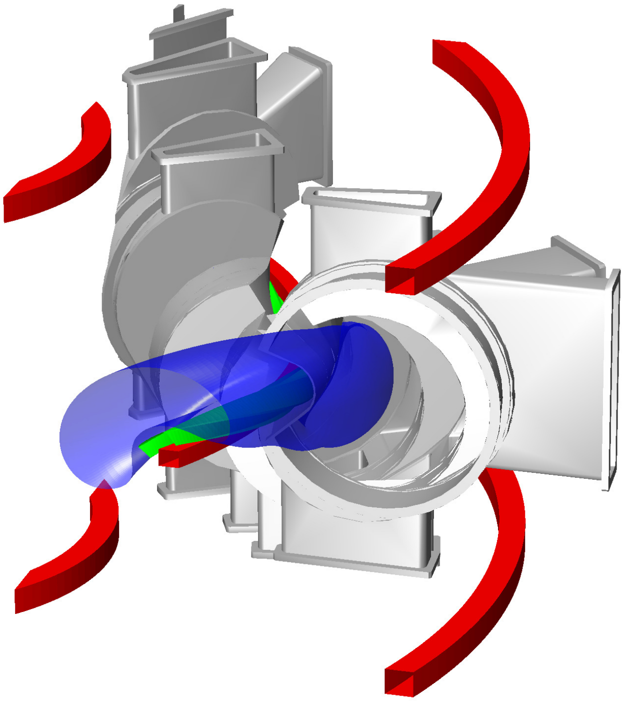

Figure B.2: Detailed view showing both the plasma in blue and the different coils: the central coil (CC), in red; the helical coil (HX) twisted around CC, in green; and the outer vertical field coils (VF), in red.

A simple solution of equation B.1 exists when τ_{LR} and I_{NI} are approximately constant, and either the ripple of the coil currents can be neglected ($dI_c^i/dt \approx 0$) or the inductive couplings vanish ($M_i \approx 0$). In this case, the well-known exponential evolution is recovered,

$$I_P(t) = (I_P(0) - I_{NI})e^{-t/\tau_{LR}} + I_{NI} \tag{B.2}$$

and the plasma current asymptotically approaches I_{NI}. When both coupling coefficients and dI_c^i/dt cannot be neglected, as it is the actual case, it is helpful to write eq. B.1 in its integral form and then define the time dependent residual of equation B.1, $\mathcal{R}(t)$, as

$$\begin{aligned}\mathcal{R}(t) \coloneqq I_P(t) &+ \frac{1}{\tau_{LR}}\int_0^t I_P(t')dt' \\ &- \sum_i \eta_i I_c^i(t) - \frac{1}{\tau_{LR}}\int_0^t I_{NI}(t')dt' - \varphi\end{aligned} \tag{B.3}$$

where $\eta_i \coloneqq \mu_i/\tau_{LR}$ and $\varphi \coloneqq I_P(0) - \Sigma_i \eta_i I_c^i(0)$ is an integration constant.

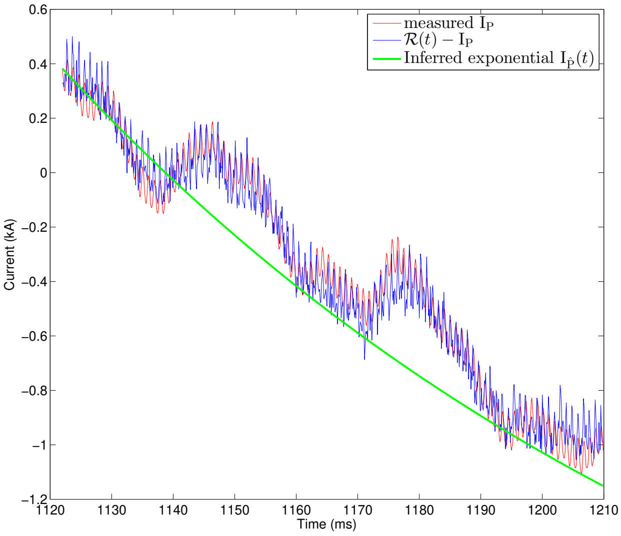

Figure B.3: Measured current I_P (red line) and $I_P - \mathcal{R}$ (blue). The inferred exponential behaviour is also depicted (black dashed line).

Since $I_P(t)$ and $I_c^i(t)$ are known, an optimization can be performed on the rest of parameters, namely τ_{LR}, η_i, I_{NI} and φ. The functional to be minimized is then $\sum_k |\mathcal{R}(t_k)|$. This also leads to the determination of R_P, L_P and M_i, provided one of them is known. Figure B.3 shows the result of this process applied to an NBI discharge in a time window in which both the density and temperature were constant enough to ensure also a nearly constant τ_{LR} and I_{NI}. The red line plots the toroidal current measured by the Rogowski coil while the blue line depicts the rest of the terms in $\mathcal{R}$ evaluated with the parameters given by the optimization. Both time traces should be equal at all times in order for equation B.1 to be fulfilled. As shown in the figure, both traces show a very similar behaviour. Since I_{NI} and τ_{LR} are given by the optimization, they can be used to construct the time evolution of the plasma current as if there was no inductive contribution. This is also represented in Figure B.3.

C. CX effects on fast-ion confinement in stellarators

The fast-ion dynamics is usually described and modelled by the Hamiltonian motion driven by the electromagnetic field and the collisions with the bulk plasma, responsible for the slowing down and the pitch-angle scattering. In addition to this dynamics, fast ions can undergo other physical phenomena such as charge-exchange reactions with the thermal neutral particles and molecules of the plasma. The relative dominance of all these interactions is based on their respective time scales. The nature of the sources of neutrals in the plasma can be very different. The main one is the recycling of the first wall i.e. part of the hydrogen of the plasma is absorbed by the materials of the first wall at the end of the shots and it is liberated in the succesive shots in form of neutral hydrogen gas. Another source of neutrals is the subproduct of the CX reactions between the fast neutrals injected by NBI and the bulk ions of the plasma: the fast neutrals become fast ions and the bulk ions turn into thermal neutrals, which are usually called *halo neutrals*. These two sources produce a quite inhomogeneous distribution of neutrals along the toroidal direction of the device due to the higher recycling in regions with more particle losses and the localization of the NBI ducts. There are methods to control the recycling of the first wall such as the deposition of lithium or boron, although the frequent use of this treatment can have deleterious effects in the plasma because of their accumulation in the vacuum vessel. Hence, the study of fast-ion dynamics must take into account this atomic process.

C.1 CX in TJ-II

In order to study the interaction of fast ions with the neutrals in TJ–II we must calculate the time scales of the different processes. The pitch-angle scattering moves particles from the passing to the trapped region of phase space and they are quickly lost, the slowing down only reduces the energy of the particles. Thus an increase of the collisionality would enhance both mechanisms (collision-driven orbit losses and thermalization) reducing the confinement time of fast ions. These two processes can not be decoupled, since they both depend on the plasma parameters, so we will give a joint *neoclassical* time scale τ_{neo} for the case in which CX reactions are not taken into account. The time scale for the CX reactions can be estimated by $\tau_{cx} \simeq [n_0 \sigma_{cx}(v) v]^{-1}$, where n_0 is the neutral density, σ_{cx} is the CX cross section, and v the fast-ion speed. The dependence of the cross section on the ion's energy is plotted in figure C.1. Then, we can estimate that, for a 15 keV ion and a typical TJ–II plasma neutral density $n_0 \sim 10^{16}$ m^{-3}, $\tau_{cx} \sim 1$ ms.

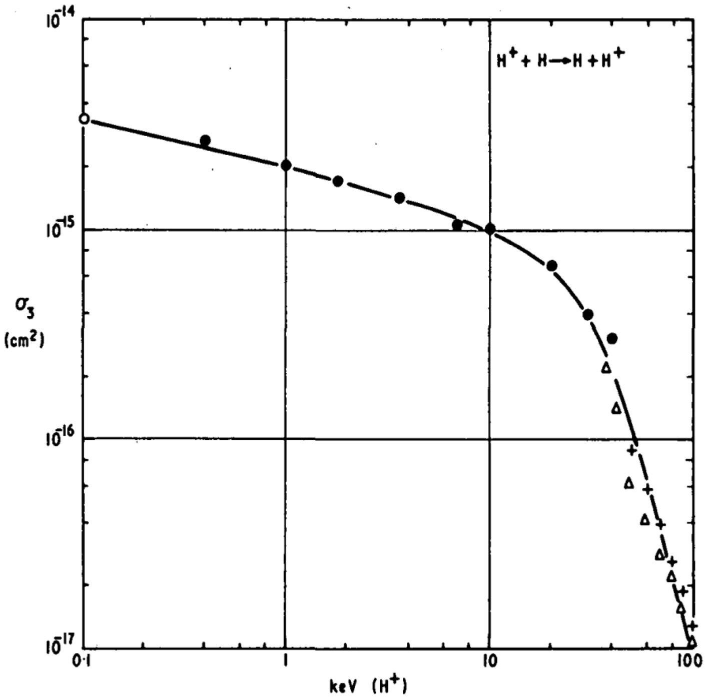

Figure C.1: Cross section of atomic reaction H$^+$+H$\rightarrow$ H+H$^+$ as a function of the energy of the reactant ion [54].

It can be seen in figure C.2a that in an ECRH (low collisional) plasma (shot #44272) $\tau_{neo} \sim 25$ ms. The different time scales τ_{neo} and τ_{cx} explain the results of chapter 7, where we saw that in the low-collisional plasmas the CX reactions clearly dominate over the neoclassical dynamics. Futhermore, the energy distributions, figure C.2b, show that almost the only fast-ion energies present in the distributions are the ones very close to the injected energies of the NBI, reflecting that fast ions barely deposit energy in the plasma. The dominance of the CX reactions in ECRH plasmas is obvious when looking at the fast-ion density and β-profiles, see figure C.3, that are strongly reduced in the case with CX.

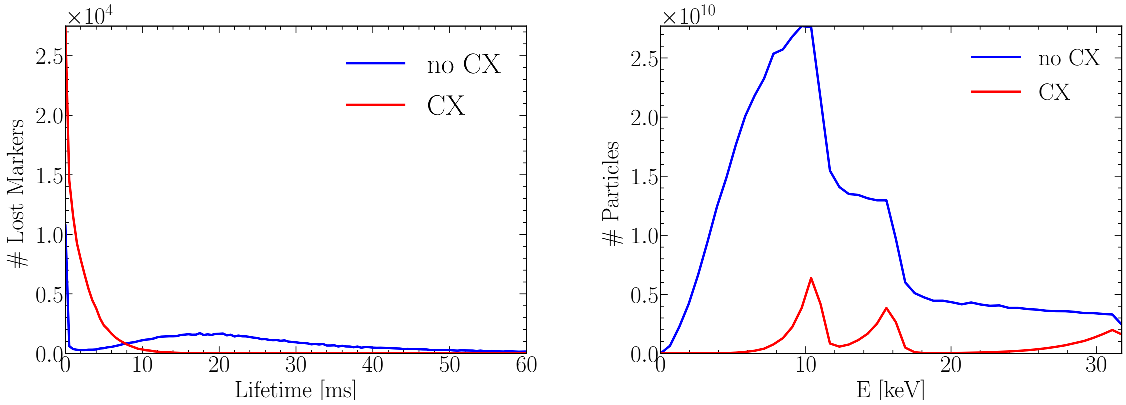

(a) **(b)**

Figure C.2: (a) Lifetimes of fast ions. (b) Energy distributions for ECRH shot #44272 with and without CX reactions.

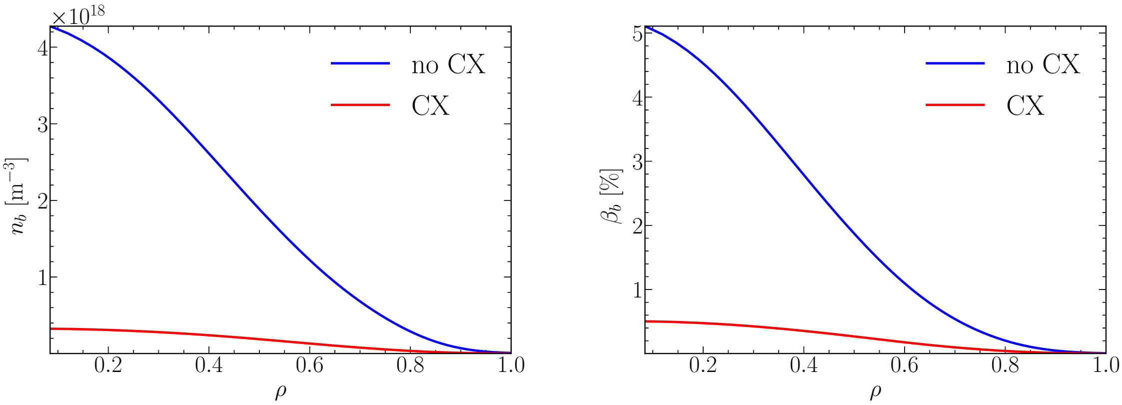

(a) **(b)**

Figure C.3: (a) Fast-ion densities. (b) β-profiles for ECRH shot #44272 with and without CX reactions.

It was shown in chapter 2 that $\tau_{neo} \sim 5$ ms for high-density NBI plasmas. In this case, the two time scales are closer and result in a much smaller effect of CX in the fast-ion population because of the earlier thermalization of fast ions than in the ECRH case. Figure C.4, shows indeed that the shorter τ_{neo} in a medium-density NBI plasma recovers the part of the distribution function in the energy range between the three distinct NBI energies, reducing the CX effects even with the same neutral density than in shot #44272. Likewise, the lower effect of CX is observed in the fast-ion densities and β-profiles, figure C.5.

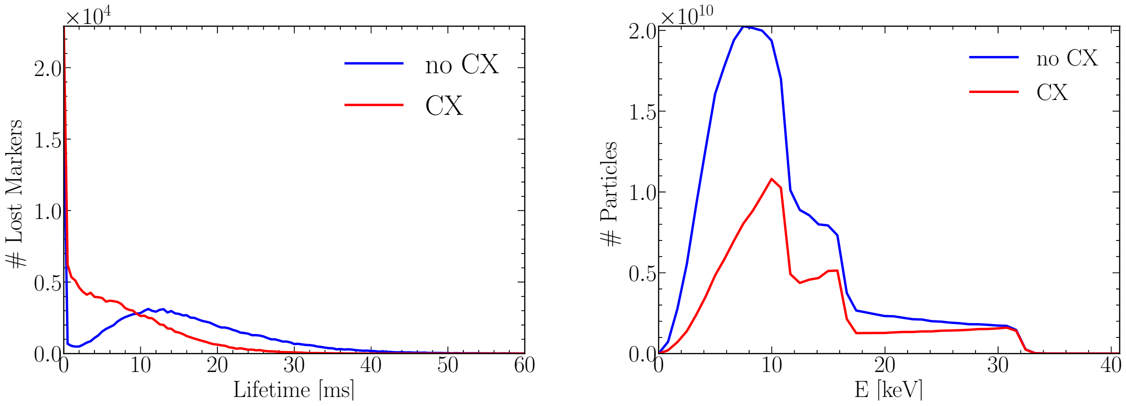

(a) (b)

Figure C.4: (a) Lifetimes of fast ions. (b) Energy distributions for ECRH shot #44257 with and without CX reactions.

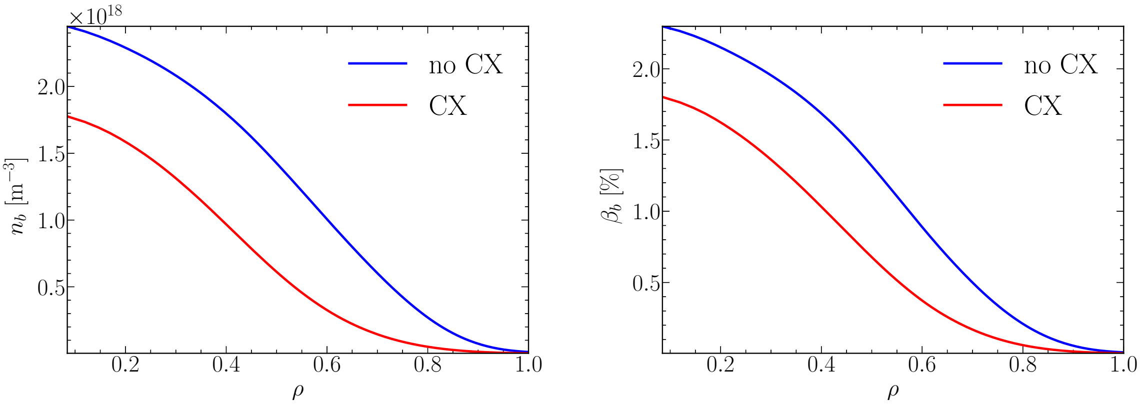

(a) (b)

Figure C.5: (a) Fast-ion densities. (b) β-profiles for ECRH shot #44257 with and without CX reactions.

C.2 CX in W7-X

The interest of CX reactions in W7-X has arised from previous studies on the power loads to the first wall by fast-ion losses [71]. This study showed that there could be important hot spots of power losses caused by fast ions, but no quantitative agreement was observed with IR imaging. A possible candidate causing these discrepancy between the simulations and experiment was thought to be the diffusion of fast-ion losses induced by CX reactions. The first step towards the assessment of this proposition is simulating a W7X shot including CX reactions. As for TJ-II, the neutral density present in the plasma is highly dependant on the toroidal region. In reference [72], upper and lower limits for the neutral-density profiles were given from experimental measurements.

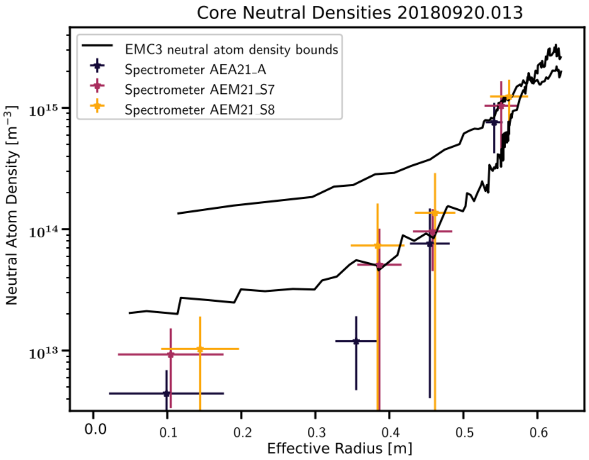

Figure C.6: A comparison of the core neutral density measured in the experiment (colored symbols) with the core neutral density profiles in EMC3-EIRENE. Because the neutral density varies depending on toroidal location, an upper and lower bound are given [72].

Taking these profiles, figure C.6, shot number 20180918.045 has been simulated including CX reactions. The results of the simulation are plotted in figures C.7 and C.8. The results imply that the influence of CX reactions is negligible, with only 4% and 1% ionized power lost due to CX for the maximum and minimum neutral density profiles, respectively. This low loss of power is understood comparing the time scales of τ_{neo} and τ_{cx}. While $\tau_{neo} \sim 10$ ms, figure C.7a, the estimated time scale of CX for the densities of figure C.6 and the NBI energies of W7-X (55, 28 and 18 keV), see figure C.1, is $\tau_{cx} \sim 100$ ms, which is much longer than the slowing-down time[1], so CX reactions occur at a time

---

[1] The good confinement of trapped particles in W7-X results in a very low percentage of fast-ion

scale not explored by fast ions. Furthermore, the CX losses would only become important if the neutral densities reached high enough levels so that $\tau_{cx} \sim \tau_{neo}$.

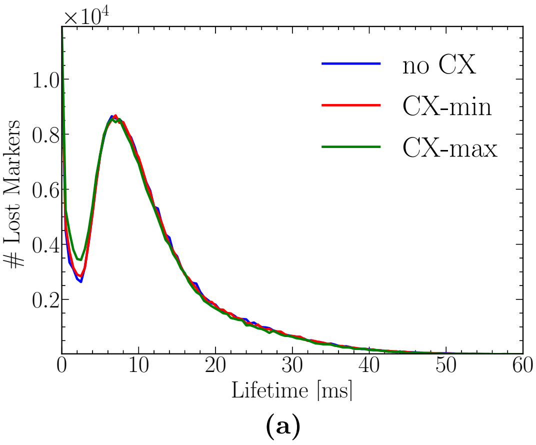

(a) **(b)**

Figure C.7: Lifetimes of fast ions, (a), and energy distributions for shot 20180918.045 with and without CX reactions, (b).

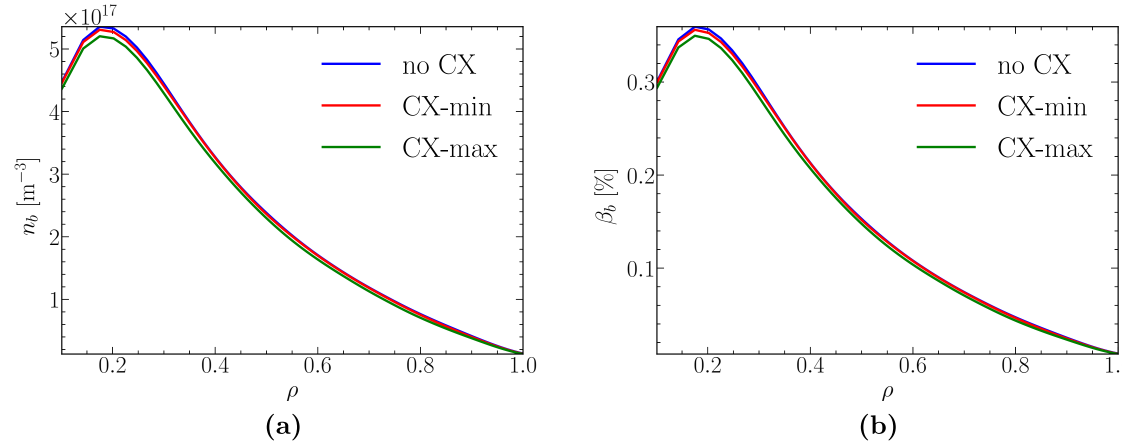

(a) **(b)**

Figure C.8: Fast-ion densities, (a), and β-profiles for shot 20180918.045 with and without CX reactions, (b).

As for the diffusion of the hot spots, figure C.9 depicts the power loads in W7-X calculated by ASCOT5 with and without CX reactions. The accumulation of fast-ion power loads in the case without CX does not dissapear in the case with CX, due to the

---

losses, hence, slowing down is the main neoclassical effect for fast ions in W7-X.

low level of power lost by CX. Yet, the extra power losses due to CX appear scattered over the first wall when CX are considered.

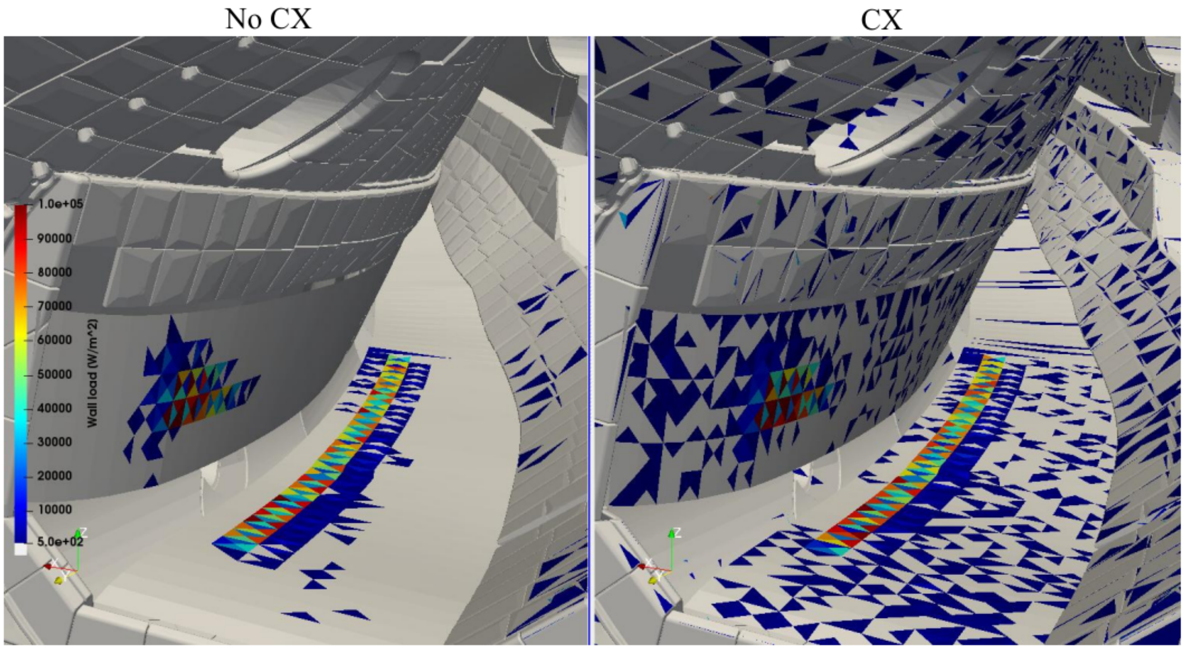

Figure C.9: Power loads calculated by ASCOT5 for shot 20180918.045 with and without CX reactions.

Recent new studies about the NBI-produced wall loads have shown agreement between simulations and experiment [73] even though CX reactions were not included in the calculations. This lines up with the results presented in this Appendix, taking into account that if the estimates of the wall loads due to CX losses had been higher the numerical results presented in [73] would not have agreed with the IR measurements.

.

D. Trapped particles and bounce-averaged drifts

The orbits of particles moving in an inhomogeneous magnetic field can be divided in two groups: passing and trapped. The parallel velocity can be written as

$$v_{\|} = \pm v\sqrt{1-\lambda B} \tag{D.1}$$

where $\lambda = \mu/E = v_{\perp}^2/(v^2 B)$ is the pitch-angle variable. As it was shown in chapter 2, the magnetic moment (μ) is conserved along the collisionless orbits of the particles and so it is the energy (E). Thus, λ is also conserved, which implies that there exist a magnetic field $B_{ref})1/\lambda$ at which the parallel velocity becomes complex which physically means that there are regions of the magnetic field through which the particle can not penetrate and it is reflected back and forth, bouncing between two points of the magnetic field line such that $\{B(l_{bi}) = B_{ref}\}_{i=1,2}$ and $\{v_{\|}(l_{bi}) = 0\}_{i=1,2}$ (see figure D.1).

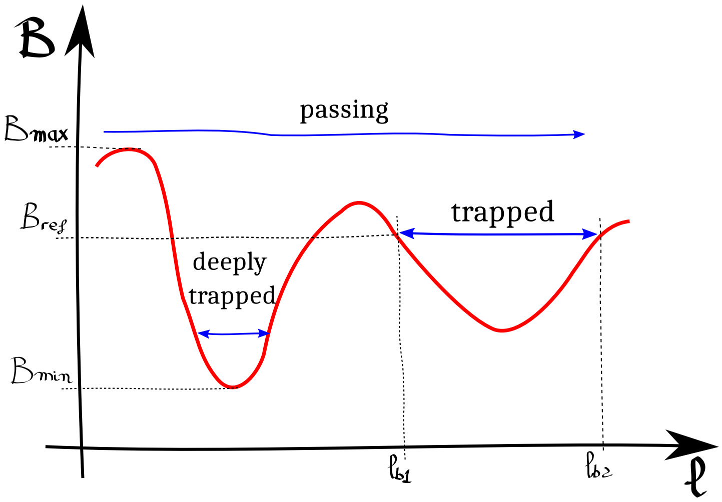

Figure D.1: Scheme of the magnetic field intensity along a field line. Trapped orbits correspond to particles that are reflected at points (l_{b1} and l_{b2}) where the magnetic field is lower or equal than the maximun one (B_{max}) at a given flux surface.

These particles are said to be trapped[1]. However, if the particle has a low enough perpendicular velocity, its corresponding B_{ref} could be higher than the maximum magnetic field of the configuration (B_{max}). For this particle $v_{\|} \neq 0$ everywhere in its trajectory and it is said to be passing[2]. Trapped orbits, in general, are not well confined and a extreme case of trapping appears when B_{ref} is close to the minimum of the flux surface (B_{min}). This case is called deeply trapping. The particles trapped in these deep magnetic wells cover a very small region of the flux surface, which makes them leave the magnetic configuration much more promptly than other trapped particles that can cover a wider region of the flux surface.

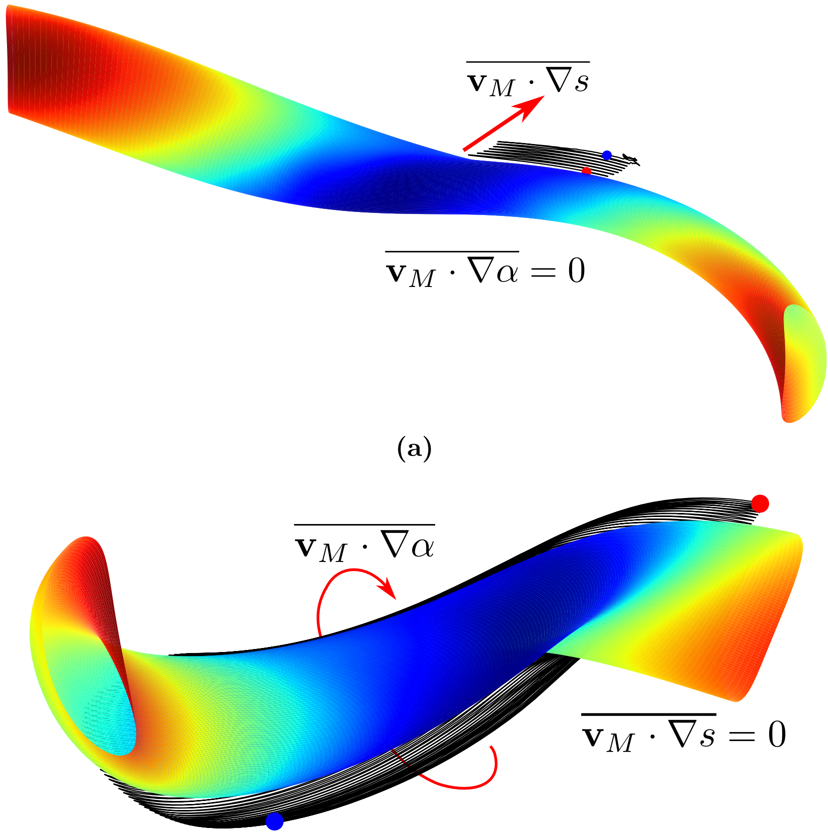

(a)

(b)

Figure D.2: Orbits of lost (a) and confined (b) particles in W7-X. The red dots represent the initial position of the particles and the blue ones the final position. The portion of the flux surfaces correspond to one period of the magnetic configuration. Notice the short toroidal excursion of the lost particle.

---

[1] Notice that the terms trapped and confined orbits/particles have a different meaning, since a particle trapped between two points of a magnetic field line can be confined (it does not leave the magnetic configuration) if its (bounce) average radial drift vanishes.

[2] Passing particles are always confined, since they cover the whole flux surface and their (flux) averaged radial drift vanishes, $\langle \mathbf{v}_M \cdot \nabla s \rangle = 0$.

In figure D.2, two trapped particle orbits are depicted. The figure on the left corresponds to a deeply trapped particle, which is quickly lost due to the radial magnetic drift, while that on the right shows the orbit of a confined particle, even though it is also trapped, due to the tangential magnetic drift.

D.1 Expressions of the bounce-averaged drifts in terms of $\mathcal{J}$ for collisionless orbits.

In this section, the expressions of the bounce-averaged drifts (radial and tangential) as a function of the second adiabatic invariant, $\mathcal{J}$, are derived for collisionless trapped orbits. In addition, we demonstrate the $\mathcal{J}$-conservation using those expressions. The importance of these expressions lie in that they give a very clear image of the link between the movement of the trapped particles and the magnetic configuration, since the bounce-average drifts on the flux surface depend on the structure of $\mathcal{J}$ that, for a given λ, is a function only of the magnetic configuration.
We consider a stellarator with nested flux surfaces in the reference system (s, α, l). The first coordinate, s, determines the flux surface; α, is the angular coordinate that labels the magnetic field lines at a fixed s and l is the length along the field line for fixed s and α. Then, the magnetic field can be expressed as

$$\mathbf{B} = \psi_{LCFS} \nabla s \times \nabla \alpha \tag{D.2}$$

where ψ_{LCFS} is the toroidal magnetic flux at the last closed flux surface.
We start with the expresion of the guiding-center drifts presented in chapter 2:

$$\mathbf{v}_d = \mathbf{v}_{M,i} + \mathbf{v}_E = \frac{1}{\Omega_i}\hat{\mathbf{b}} \times (v_{||}^2 \boldsymbol{\kappa} + \mu \nabla B) + \frac{1}{B}\hat{\mathbf{b}} \times \nabla \varphi, \tag{D.3}$$

where $\Omega_i = qB/m$ is the gyrofrequency of the ions, $\hat{\mathbf{b}} = \mathbf{B}/B$, $v_{||}$ is the parallel velocity, $\boldsymbol{\kappa} = \hat{\mathbf{b}} \cdot \nabla \hat{\mathbf{b}}$ is the curvature of the magnetic field line, $\mu = mv_{\perp}^2/(2B)$ and φ the electrostatic potential.

D.2 Bounce-averaged radial drift

The radial drift is defined as $\mathbf{v}_d \cdot \nabla s$. Hence, we start manipulating the vector terms appearing in (D.3) after projecting them in the radial direction:

$$(\hat{\mathbf{b}}\times\boldsymbol{\kappa})\cdot\nabla s \tag{D.4}$$

$$(\hat{\mathbf{b}}\times\nabla B)\cdot\nabla s \tag{D.5}$$

$$(\hat{\mathbf{b}}\times\nabla\varphi)\cdot\nabla s. \tag{D.6}$$

We calculate, for convinience, the Jacobian of the transformation to the (s,α,l) coordinate system. If the vectors $\{\mathbf{e}_i\}_{i=s,\alpha,l}$ represent the vectors (covariant) tangent to the flux surface in the radial, poloidal and field line directions, the vector $\hat{\mathbf{b}}$ can be expressed as

$$\hat{\mathbf{b}}\equiv\frac{\mathbf{B}}{B}=\frac{\psi_{LCFS}}{B}\nabla s\times\nabla\alpha=\frac{\psi_{LCFS}}{B\sqrt{g}}\mathbf{e}_l\equiv\frac{\psi_{LCFS}}{B\sqrt{g}}\hat{\mathbf{b}}, \tag{D.7}$$

since the vector $\mathbf{e}_l\equiv\hat{\mathbf{b}}$, from which we obtain that the jacobian of the transformation is

$$\sqrt{g}=\frac{\psi_{LCFS}}{B}. \tag{D.8}$$

Now, ee can work out the term (D.4). The curvature $\boldsymbol{\kappa}$ can be expressed in terms of the contravariant vectors as

$$\boldsymbol{\kappa}=\hat{\mathbf{b}}\cdot\nabla\hat{\mathbf{b}}=(\hat{\mathbf{b}}\cdot\nabla\hat{\mathbf{b}}\cdot\mathbf{e}_s)\nabla s+(\hat{\mathbf{b}}\cdot\nabla\hat{\mathbf{b}}\cdot\mathbf{e}_\alpha)\nabla\alpha+(\hat{\mathbf{b}}\cdot\nabla\hat{\mathbf{b}}\cdot\mathbf{e}_l)\nabla l. \tag{D.9}$$

Now, taking into account that $\mathbf{e}_l\equiv\hat{\mathbf{b}}$ and that $\mathbf{A}\times(\nabla\times\mathbf{B})=(\nabla\mathbf{B})\mathbf{A}-(\mathbf{A}\cdot\nabla)\mathbf{B}$ one can see that the last term vanishes and then

$$\boldsymbol{\kappa}=(\hat{\mathbf{b}}\cdot\nabla\hat{\mathbf{b}}\cdot\mathbf{e}_s)\nabla s+(\hat{\mathbf{b}}\cdot\nabla\hat{\mathbf{b}}\cdot\mathbf{e}_\alpha)\nabla\alpha. \tag{D.10}$$

from which is easy to see that

$$\begin{aligned}(\hat{\mathbf{b}}\times\boldsymbol{\kappa})\cdot\nabla s=&(\hat{\mathbf{b}}\times(\hat{\mathbf{b}}\cdot\nabla\hat{\mathbf{b}}\cdot\mathbf{e}_\alpha)\nabla\alpha)\cdot\nabla s=\\&(\hat{\mathbf{b}}\cdot\nabla\hat{\mathbf{b}}\cdot\mathbf{e}_\alpha)(\hat{\mathbf{b}}\times\nabla\alpha)\cdot\nabla s=\\&(\hat{\mathbf{b}}\cdot\nabla\hat{\mathbf{b}}\cdot\mathbf{e}_\alpha)(g_{li}\mathbf{e}^i\times\nabla\alpha)\cdot\nabla s=\\&(\hat{\mathbf{b}}\cdot\nabla\hat{\mathbf{b}}\cdot\mathbf{e}_\alpha)(\nabla l\times\nabla\alpha)\cdot\nabla s=\\&-(\hat{\mathbf{b}}\cdot\nabla\hat{\mathbf{b}}\cdot\mathbf{e}_\alpha)\frac{1}{\sqrt{g}}=-\frac{B}{\psi_{LCFS}}(\hat{\mathbf{b}}\cdot\nabla\hat{\mathbf{b}}\cdot\mathbf{e}_\alpha)\end{aligned} \tag{D.11}$$

where we have used that $\hat{\mathbf{b}}\equiv\mathbf{e}_l=g_{li}\mathbf{e}^i$, assuming Einstein's summation and that the coeffients $g_{li}=\mathbf{e}_l\cdot\mathbf{e}_i$ are the metric coefficients. Noting that $\hat{\mathbf{b}}\cdot\nabla\hat{\mathbf{b}}\cdot\mathbf{e}_\alpha=\partial_l\hat{\mathbf{b}}\cdot\partial_\alpha\mathbf{r}=\partial_l(\hat{\mathbf{b}}\cdot\partial_\alpha\mathbf{r})-\cancelto{0}{\hat{\mathbf{b}}\cdot\partial_l\partial_\alpha\mathbf{r}}$, (D.4) becomes

$$(\hat{\mathbf{b}}\times\boldsymbol{\kappa})\cdot\nabla s=-\frac{B}{\psi_{LCFS}}\partial_l(\hat{\mathbf{b}}\cdot\partial_\alpha\mathbf{r}) \tag{D.12}$$

In order to calculate the term in (D.5), is useful to write the explicit expression of the gradient of the magnetic field intensity,

$$\nabla B = \partial_s B \nabla s + \partial_\alpha B \nabla \alpha + \partial_l B \nabla l. \tag{D.13}$$

This expression, together with the tools used to obtain (D.12) we find that

$$(\hat{\mathbf{b}} \times \nabla B) \cdot \nabla s = \frac{B}{\psi_{LCFS}} (\hat{\mathbf{b}} \cdot \mathbf{e}_\alpha \partial_l B - \partial_\alpha B) \tag{D.14}$$

The term (D.6) is analogous to the (D.5) if we exchange ($B \leftrightarrow \varphi$):

$$(\hat{\mathbf{b}} \times \nabla \varphi) \cdot \nabla s = \frac{B}{\psi_{LCFS}} (\hat{\mathbf{b}} \cdot \mathbf{e}_\alpha \partial_l \varphi - \partial_\alpha \varphi) \tag{D.15}$$

Now, we are in the position of calculating the bounce-averaged radial drift. The bounce-average operator is defined as

$$\begin{aligned} \overline{F} &= \frac{2}{\tau_b} \int_{l_{b1}}^{l_{b2}} \frac{F}{|v_{||}|} dl \\ \tau_b &= 2 \int_{l_{b1}}^{l_{b2}} \frac{1}{|v_{||}|} dl \end{aligned} \tag{D.16}$$

Then, using (D.3), (D.12), (D.14) and (D.15) we can write

$$\begin{aligned} \overline{(\mathbf{v}_M + \mathbf{v}_E) \cdot \nabla s} = \frac{2}{\tau_b \psi_{LCFS}} \int_{l_{b1}}^{l_{b2}} dl \Big\{ \frac{m}{q} \Big(& - |v_{||}| \partial_l (\hat{\mathbf{b}} \cdot \partial_\alpha \mathbf{r}) + \\ & \frac{\mu}{m|v_{||}|} (\hat{\mathbf{b}} \cdot \partial_\alpha \mathbf{r} \partial_l B - \partial_\alpha B) \Big) + \\ & \frac{1}{|v_{||}|} (\hat{\mathbf{b}} \cdot \partial_\alpha \mathbf{r} \partial_l \varphi - \partial_\alpha \varphi) \Big\}. \end{aligned} \tag{D.17}$$

Considering that the first term in the brackets of (D.17) can be expressed as $|v_{||}| \partial_l (\hat{\mathbf{b}} \cdot \partial_\alpha \mathbf{r}) = \partial_l (|v_{||}| \hat{\mathbf{b}} \cdot \partial_\alpha \mathbf{r}) - \partial_l |v_{||}| \hat{\mathbf{b}} \cdot \partial_\alpha \mathbf{r}$ and that $|v_{||}| = \sqrt{\frac{2}{m}(\mathcal{E} - q\varphi) - \frac{2\mu B}{m}}$ and substituting them in (D.17) we obtain that

$$\begin{aligned} \overline{(\mathbf{v}_M + \mathbf{v}_E) \cdot \nabla s} = & - \frac{2}{\tau_b \psi_{LCFS}} \int_{l_{b1}}^{l_{b2}} \frac{m}{q} \partial_l (|v_{||}| \hat{\mathbf{b}} \cdot \partial_\alpha \mathbf{r}) dl \\ & - \frac{2}{q \tau_b \psi_{LCFS}} \int_{l_{b1}}^{l_{b2}} (\mu \partial_\alpha B + q \partial_\alpha \varphi) \frac{dl}{|v_{||}|}, \end{aligned} \tag{D.18}$$

where the first integral vanishes beacause $v_{||} = 0$ at the bounce points. Lastly the final expression for the bounce-averaged radial drift reads

$$\overline{(\mathbf{v}_M + \mathbf{v}_E) \cdot \nabla s} = \frac{m}{q \tau_b \psi_{LCFS}} \partial_\alpha \mathcal{J} \tag{D.19}$$

with

$$\mathcal{J} = 2 \int_{l_{b1}}^{l_{b2}} |v_{||}| dl \tag{D.20}$$

D.3 Bounce-averaged tangential drift

Analogously to the procedure of section D.2, one can show that the bounce-averaged tangential drift reads

$$\overline{(\mathbf{v}_M + \mathbf{v}_E) \cdot \nabla\alpha} = -\frac{m}{q\tau_b\psi_{LCFS}}\partial_s\mathcal{J} \tag{D.21}$$

D.4 Conservation of $\mathcal{J}$

It is worth mentioning that due to expressions (D.19) and (D.21) one can see that particles move maintaining the second adiabatic invariant constant,

$$\frac{d\mathcal{J}}{dt} = \dot{s}\partial_s\mathcal{J} + \dot{\alpha}\partial_\alpha\mathcal{J} = 0. \tag{D.22}$$

Resumen

Durante las dos últimas décadas, los desarrollos teóricos relativos al transporte neoclásico en stellarators han aumentado el interés por muchos aspectos de la física de iones rápidos en estos dispositivos. Este trabajo está dedicado al estudio de la dinámica de dichas partículas así como a la validación de códigos para su modelado en stellarators, lo cual es fundamental a la hora de interpretar datos experimentales y predecir el resultado de experimentos futuros.

Un análisis detallado de la función de distribución de iones rápidos, generados por inyección de haces neutros (NBI) y calculada mediante el código Monte Carlo de seguimiento de órbitas ASCOT5, ha sido llevado a cabo en diferentes escenarios de plasma del stellarator TJ-II. Esta función de distribución se ha utilizado en el cálculo y la validación de la corriente eléctrica producida por la inyección de haces neutros, empleada habitualmente para el calentamiento del plasma. El sistema de NBI del TJ-II ha sido simulado con el módulo de ASCOT5 beamlet-based neutral-beam injection (BBNBI). Este código Monte Carlo toma los parámetros operativos y la geometría de los inyectores del haz de neutros y simula el vuelo de las partículas neutras hacia el plasma, así como su proceso de ionización dentro del mismo. ASCOT5, usando los iones rápidos generados con BBNBI, la configuración magnética, los perfiles del plasma y un modelo de la primera pared de TJ-II, resuelve la ecuación de Fokker-Planck asociada a la función de distribución de iones rápidos con un método Monte Carlo, siguiendo las trayectorias de los mismos a lo largo del campo magnético y simulando la transferencia de energía al plasma (slowing down). La función de distribución calculada se utiliza posteriormente para calcular la corriente generada por el haz de neutros (NBCD), que tiene dos contribuciones: la corriente de los propios iones rápidos y la respuesta de los electrones del plasma a esta corriente. La primera se calcula a partir del primer momento en velocidad paralela de la función de distribución, mientras que la segunda se obtiene resolviendo analíticamente la ecuación de deriva cinética (DKE) para los electrones del plasma a baja colisionalidad. Junto con las estimaciones de NBCD, se presentan los

resultados de potencia no ionizada (shine-through), depositada en el plasma y la densidad de iones rápidos para plasmas de TJ-II con alta densidad.

A continuación, los resultados computacionales de la fracción de shine-through y NBCD han sido validados frente a valores experimentales obtenidos en escenarios de plasma generados mediante el uso de ambos inyectores (paralelo y antiparalelo) por separado. Las estimaciones de la fracción de shine-through y NBCD han sido comparadas con medidas por termografía infrarroja y la corriente toroidal del plasma medida por la bobina de Rogowski respectivamente. Para la validación de la NBCD, es necesario tener en cuenta la contribución de la corriente de bootstrap a la corriente toroidal, que ha sido calculada con el código DKES. La comparación de las fracciones de shine-through muestra una buena concordancia entre las simulaciones y los experimentos para ambos inyectores, mientras que la comparación de la corriente toroidal calculada y la medida muestra similitud sólo para el caso del inyector antiparalelo. Se discuten las posibles causas de la discrepancia observada para los casos con inyección paralela.

Aprovechando la experiencia adquirida con ASCOT5, se ha llevado a cabo una validación de un nuevo modelo (Γ_α) que evalua de forma rápida la fracción de pérdidas tempranas de iones rápidos en stellarators en diferentes configuraciones magnéticas del stellarator Wendelstein 7-X (W7-X). Esto ha permitido incluirlo en el paquete de códigos de optimización de stellarators STELLOPT. La predicción del modelo Γ_α ha sido comprobada con ASCOT5 siguiendo las órbitas de una población de iones rápidos uniformemente distribuidos en el espacio de fases en varias configuraciones magnéticas de W7-X. La comparación de la fracción de iones perdidos hasta $t = 1$ ms con los valores dados por Γ_α muestra un acuerdo cuantitativo entre los dos métodos. Este estudio también ha demostrado el mejor rendimiento de Γ_α frente a otros modelos, como Γ_c, utilizados ampliamente en la optimización de stellarators.

Por último, se ha evaluado la fracción de pérdidas de iones rápidos en una nueva configuración cuasi-isodinámica optimizada para el confinamiento de iones rápidos, obtenida con STELLOPT, siguiendo las mismas técnicas anteriormente descritas. Los resultados muestran un muy buen confinamiento de iones rápidos a $\beta = 1,5\%$, que se convierte en excelente a $\beta = 4\%$. Durante una segunda fase del proceso de optimización ha sido diseñado un conjunto de bobinas magnéticas para la nueva configuración. A pesar de que se esperaba una degradación del confinamiento en esta situación más realista, la fracción de pérdidas calculada por ASCOT5 indica que la configuración ha preservado un nivel bueno de confinamiento de los iones rápidos en el centro del plasma.

Bibliography

[1] Jef Ongena and Yuichi Ogawa.
Nuclear fusion: Status report and future prospects.
Energy Policy, 96:770–778, 2016.

[2] Allen H. Boozer and Henry J. Gardner.
The bootstrap current in stellarators.
Physics of Fluids B: Plasma Physics, 2:2408–2421, 10 1990.

[3] J. P. Freidberg.
Ideal magnetohydrodynamic theory of magnetic fusion systems.
Rev. Mod. Phys., 54:801–902, Jul 1982.

[4] Per Helander.
Theory of plasma confinement in non-axisymmetric magnetic fields.
Reports on Progress in Physics, 77, 2014.

[5] W. D. D'Haeseleer, W. N. G. Hitchon, J. D. Callen, and J. L. Shohet.
Flux Coordinates and Magnetic Field Structure - A Guide to a Fundamental Tool of the Plasma Theory.
Springer Series in Computational Physics, Springer Verlag Berlin, 1991.

[6] R.J. Goldston and P.H. Rutherford.
Introduction to Plasma Physics.
CRS Press, 1995.

[7] J. Wesson and D.J. Campbell.
Tokamaks.
International series of monographs on physics. Clarendon Press, 2004.

[8] M. Wakatani.

Stellarator and Heliotron Devices.
Oxford University Press, 1998.

[9] Lise-Marie Imbert-Gerard, Elizabeth J. Paul, and Adelle M. Wright.
An Introduction to Stellarators: From magnetic fields to symmetries and optimization.
aug 2019.

[10] T. Sunn Pedersen and et al.
Confirmation of the topology of the wendelstein 7-x magnetic field to better than 1:100,000.
Nature Communications, 7(13493), 2016.

[11] Matt Landreman, Bharat Medasani, and Caoxiang Zhu.
Stellarator optimization for good magnetic surfaces at the same time as quasisymmetry.
Physics of Plasmas, 28(9):092505, 2021.

[12] Felix I Parra and Iván Calvo.
Phase-space Lagrangian derivation of electrostatic gyrokinetics in general geometry.
Plasma Physics and Controlled Fusion, 53(4):045001, apr 2011.

[13] V.I. Arnold.
Mathematical methods of classical mechanics, volume 60.
Springer, 1989.

[14] P. Helander and D. J. Sigmar.
Collisional Transport in Magnetized Plasmas.
Cambridge University Press, 2005.

[15] N. G. Van Kampen.
Stochastic Processes in Physics and Chemistry.
Elsevier, 2007.

[16] Eero Hirvijoki.
Theory and models for Monte Carlo simulations of minority particle populations in tokamak plasmas.
Doctoral thesis, School of Science, 2014.

[17] C. Alejaldre, J. Alonso, J. Botija, F. Castejón, J. R. Cepero, J. Guasp, A. Lopez-Fraguas, L. García, V. I. Krivenski, R. Martín, A. P. Navarro, A. Perea, A. Rodriguez-Yunta, M. Sorolla, and A. Varias.
TJ-II Project: A Flexible Heliac Stellarator.
Fusion Technology, 17(1):131–139, jan 1990.

[18] S. P Hirshman.
Steepest-descent moment method for three-dimensional magnetohydrodynamic equilibria.
Physics of Fluids, 26:3553, 1983.

[19] J. Martínez-Fernández, Á. Cappa, M. Tereshchenko, A. Tolkachev, A. Ros, and G. Catalán.
High power characterisation of the ecrh transmission lines and power deposition calculations in the tj-ii stellarator.
Fusion Engineering and Design, 161:112065, 2020.

[20] M. Liniers, J. Damba, J. Guasp, J. A. Sebastián, F. Martín, B. Rojo, R. Carrasco, E. Sánchez, F. Miguel, G. Wolfers, A. Soleto, and E. Ascasíbar.
Beam transmission dependence on beam parameters for TJ-II Neutral Beam Injectors.
Fusion Engineering and Design, 123:259–262, nov 2017.

[21] J. Guasp and M. Liniers.
Fast ion behaviour for NBI scenarios in TJ-II.
Proceedings of the 10th Stellarator Workshop, page 204, 1995.

[22] C. J. Barth, F. J. Pijper, H. J. v. d. Meiden, J. Herranz, and I. Pastor.
High-resolution multiposition thomson scattering for the tj-ii stellarator.
Review of Scientific Instruments, 70(1):763–767, 1999.

[23] A V Melnikov, L G Eliseev, J M Barcala, A Cappa, A A Chmyga, M A Drabinskiy, C Hidalgo, P O Khabanov, N K Kharchev, A S Kozachek, M Liniers, D López-Bruna, U Losada, S E Lysenko, F Medina, A Molinero, M Ochando, J L De Pablos, I Pastor, and TJ-II Team.
2d distributions of potential and density mean-values and oscillations in the ecrh and nbi plasmas at the tj-ii stellarator.
Plasma Physics and Controlled Fusion, 64(5):054009, apr 2022.

[24] T. Happel, T. Estrada, E. Blanco, V. Tribaldos, A. Cappa, and A. Bustos.
Doppler reflectometer system in the stellarator tj-ii.
Review of Scientific Instruments, 80(7):073502, 2009.

[25] T Estrada, J Sánchez, B van Milligen, L Cupido, A Silva, M E Manso, and V Zhuravlev.
Density profile measurements by am reflectometry in tj-ii.
Plasma Physics and Controlled Fusion, 43(11):1535, oct 2001.

[26] A. Hidalgo, D. Tafalla, B. Brañas, and F. L. Tabarés.
Multipulse supersonic helium beam diagnostic in the tj-ii stellarator.
Review of Scientific Instruments, 75(10):3478–3480, 2004.

[27] J. M. Fontdecaba, S. Ya. Petrov, V. G. Nesenevich, A. Ros, F. V. Chernyshev, K. J. McCarthy, and J. M. Barcala.
Upgrade of the neutral particle analyzers for the tj-ii stellarator.
Review of Scientific Instruments, 85(11):11E803, 2014.

[28] I. H. Hutchinson.
Principles of Plasma Diagnostics.
Cambridge University Press, jul 2002.

[29] E. Hirvijoki, O. Asunta, T. Koskela, T. Kurki-Suonio, J. Miettunen, S. Sipilä, A. Snicker, and S. Äkäslompolo.
Ascot: Solving the kinetic equation of minority particle species in tokamak plasmas.
Computer Physics Communications, 185:1310–1321, 4 2014.

[30] K. Särkimäki.
Modelling and understanding fast particle transport in non-axisymmetric tokamak plasmas.
PhD thesis, Department of Applied Physics, Aalto University, 2019.

[31] J. Varje, K. Särkimäki, J. Kontula, P. Ollus, T. Kurki-Suonio, A. Snicker, E. Hirvijoki, and S. Äkäslompolo.
High-performance orbit-following code ASCOT5 for Monte Carlo simulations in fusion plasmas.
aug 2019.

[32] M. Drevlak, D. Monticello, and A. Reiman.

Pies free boundary stellarator equilibria with improved initial conditions.
Nuclear Fusion, 45:731–740, 7 2005.

[33] G. V. Pereverzev and P. N. Yushmanov.
ASTRA automated system for transport analysis in a tokamak.
Technical report, Max-Planck-Institut für Plasmaphysik, Garching, 2002.

[34] O. Asunta, J. Govenius, R. Budny, M. Gorelenkova, G. Tardini, T. Kurki-Suonio, A. Salmi, and S. Sipilä.
Modelling neutral beams in fusion devices: Beamlet-based model for fast particle simulations.
Computer Physics Communications, 188:33–46, mar 2015.

[35] S. Äkäslompolo, P. Drewelow, Y. Gao, A. Ali, O. Asunta, S. Bozhenkov, J. Fellinger, O.P. Ford, N. den Harder, D. Hartmann, M. Jakubowski, P. McNeely, H. Niemann, F. Pisano, N. Rust, A. Puig Sitjes, M. Sleczka, A. Spanier, and R.C. Wolf.
Validating fast-ion wall-load IR analysis-methods against W7-X NBI empty-torus experiment.
Journal of Instrumentation, 14(07):P07018–P07018, jul 2019.

[36] S. Suzuki, T. Shirai, M. Nemoto, K. Tobita, H. Kubo, T. Sugie, A. Sakasai, and Y. Kusama.
Attenuation of high-energy neutral hydrogen beams in high-density plasmas.
Plasma Physics and Controlled Fusion, 40(12):2097–2111, dec 1998.

[37] T. Ohkawa.
New methods of driving plasma current in fusion devices.
Nuclear Fusion, 10(2):185–188, jun 1970.

[38] D. F. H. Start, P. R. Collins, E. M. Jones, A. C. Riviere, and D. R. Sweetman.
Observation of Beam-Induced Currents in a Toroidal Plasma.
Physical Review Letters, 40(23):1497–1500, jun 1978.

[39] S. P. Hirshman.
Classical collisional theory of beam-driven plasma currents.
Physics of Fluids, 23(6):1238, 1980.

[40] J. G. Cordey, E. M. Jones, D. F. H. Start, A. R. Curtis, and I. P. Jones.
A kinetic theory of beam-induced plasma currents.
Nuclear Fusion, 19(2):249–259, feb 1979.

[41] J. W. Connor and J. G. Cordey.
Effects of neutral injection heating upon toroidal equilibria.
Nuclear Fusion, 14(2):185–190, apr 1974.

[42] D. F. H. Start, J. G. Cordey, and E. M. Jones.
The effect of trapped electrons on beam driven currents in toroidal plasmas.
Plasma Physics, 22(4):303–316, apr 1980.

[43] Y. R. Lin-Liu and F. L. Hinton.
Trapped electron correction to beam driven current in general tokamak equilibria.
Physics of Plasmas, 4(11):4179–4181, nov 1997.

[44] Y. J. Hu, Y. M. Hu, and Y. R. Lin-Liu.
Electron shielding current in neutral beam current drive in general tokamak equilibria and arbitrary collisionality regime.
Physics of Plasmas, 19(3):034505, mar 2012.

[45] N. Nakajima and M. Okamoto.
Beam-Driven Currents in the $1/\nu$ Regime in a Helical System.
Journal of the Physical Society of Japan, 59(10):3595–3601, oct 1990.

[46] S. Mulas, Á. Cappa, J. Kontula, D. López-Bruna, I. Calvo, F.I. Parra, M. Liniers, T. Kurki-Suonio, and M. Mantsinen.
ASCOT5 simulations of neutral beam heating and current drive in the TJ-II stellarator.
Nuclear Fusion, 62(10):106008, oct 2022.

[47] Á. Cappa, J. Varela, D. López-Bruna, E. Ascasíbar, M. Liniers, L. G. Eliseev, J. M. Fontdecaba, J. M. García-Regaña, A. González-Jerez, N. K. Kharchev, F. Medina, A. V. Melnikov, S. Mulas, M. Ochando, D. Spong, J. L. Velasco, and TJ-II Team.
Stability analysis of TJ-II stellarator NBI driven Alfvén eigenmodes in ECRH and ECCD experiments.
Nuclear Fusion, 61(6):066019, jun 2021.

[48] J. Guasp and M. Liniers.
Loss cone structure for ions in the TJ-II helical axis stellarator Part I: Properties without a radial electric field.
Nuclear Fusion, 40(3):397–409, mar 2000.

[49] B. Ph. van Milligen, T. Estrada, E. Ascasíbar, D. Tafalla, D. López-Bruna, A. López Fraguas, J. A. Jiménez, I. García-Cortés, A. Dinklage, and R. Fischer.
Integrated data analysis at TJ-II: The density profile.
Review of Scientific Instruments, 82(7):073503, jul 2011.

[50] Tim Happel.
Doppler refectometry in the TJ-II stellarator: design of an optimized Doppler reflectometer and its application to turbulence and radial electric field studies.
dec 2010.

[51] D López-Bruna, J L Velasco, M Ochando, J Guasp, A López-Fraguas, B P van Milligen, E Ascasíbar, M Liniers, T Estrada, J M Fontdecaba, I Pastor, D Tafalla, F Medina, L Eliseev, A Melnikov, S Perfilov, J Herranz, B Zurro, K J McCarthy, and F Tabarés.
Transport in threshold plasmas for a confinement transition in the TJ-II stellarator.
Plasma Physics and Controlled Fusion, 55(1):015001, jan 2013.

[52] Kieran J McCarthy, V Tribaldos, J Arévalo, and M Liniers.
The detection of fast oxygen ions in neutral beam-heated plasmas of the TJ-II stellarator using spectroscopy methods.
Journal of Physics B: Atomic, Molecular and Optical Physics, 43(14):144020, jul 2010.

[53] Mark J H Cornelissen, Samuel A Lazerson, Yu Gao, Josefine H E Proll, Paul McNeely, Norbert Rust, Dirk Hartmann, Marcin W Jakubowski, Adnan Ali, Fabio Pisano, Holger Niemann, Aleix Puig Sitjes, Ralf König, Robert C Wolf, and the W7-X Team.
Identification of fast ion wall loads in wendelstein 7-x from thermographic measurements.
Plasma Physics and Controlled Fusion, 64:125015, 12 2022.

[54] A.C. Riviere.
Penetration of fast hydrogen atoms into a fusion reactor plasma.
Nuclear Fusion, 11:363–369, 8 1971.

[55] J L Velasco, K Allmaier, A López-Fraguas, C D Beidler, H Maassberg, W Kernbichler, F Castejón, and J A Jiménez.
Calculation of the bootstrap current profile for the tj-ii stellarator.

Plasma Physics and Controlled Fusion, 53:115014, 11 2011.

[56] J.M. Faustin, W.A. Cooper, J.P. Graves, D. Pfefferlé, and J. Geiger.
Fast particle loss channels in Wendelstein 7-X.
Nuclear Fusion, 56(9):092006, sep 2016.

[57] Samuel Lazerson, John Schmitt, Caoxiang Zhu, Joshua Breslau, All STELLOPT Developers, and USDOE Office of Science.
Stellopt, version 2.7.5, 5 2020.

[58] V. V. Nemov, S. V. Kasilov, W. Kernbichler, and G. O. Leitold.
Poloidal motion of trapped particle orbits in real-space coordinates.
Physics of Plasmas, 15:052501, 5 2008.

[59] J.L. Velasco, I. Calvo, S. Mulas, E. Sánchez, F.I. Parra, Á. Cappa, and the W7-X Team.
A model for the fast evaluation of prompt losses of energetic ions in stellarators.
Nuclear Fusion, 61:116059, 11 2021.

[60] C. D. Beidler, Ya. I. Kolesnichenko, V. S. Marchenko, I. N. Sidorenko, and H. Wobig.
Stochastic diffusion of energetic ions in optimized stellarators.
Physics of Plasmas, 8(6):2731–2738, jun 2001.

[61] Ya. I. Kolesnichenko, V. V. Lutsenko, and A. V. Tykhyy.
Stochastic diffusion of energetic ions in Wendelstein-line stellarators: Numerical validation of theory predictions and new findings.
Physics of Plasmas, 29(10):102506, oct 2022.

[62] Allen H. Boozer.
Plasma equilibrium with rational magnetic surfaces.
Physics of Fluids, 24(11):1999, 1981.

[63] Iván Calvo, Felix I Parra, José Luis Velasco, and J Arturo Alonso.
The effect of tangential drifts on neoclassical transport in stellarators close to omnigeneity.
Plasma Physics and Controlled Fusion, 59:055014, 5 2017.

[64] Aaron Bader, M. Drevlak, D. T. Anderson, B. J. Faber, C. C. Hegna, K. M. Likin, J. C. Schmitt, and J. N. Talmadge.
Stellarator equilibria with reactor relevant energetic particle losses.

Journal of Plasma Physics, 85(5):905850508, oct 2019.

[65] M. Drevlak, J. Geiger, P. Helander, and Y. Turkin.
Fast particle confinement with optimized coil currents in the W7-X stellarator.
Nuclear Fusion, 54(7):073002, jul 2014.

[66] E. Sánchez, J. L. Velasco, I. Calvo, and S. Mulas.
A quasi-isodynamic configuration with good confinement of fast ions at low plasma β, 2022.

[67] Matt Landreman.
An improved current potential method for fast computation of stellarator coil shapes.
Nuclear Fusion, 57(4):046003, apr 2017.

[68] A. Dinklage, G. Fuchert, R.C. Wolf, A. Alonso, T. Andreeva, C.D. Beidler, M. de Baar, Y. Gao, J. Geiger, M. Jakubowski, H. Laqua, N. Marushchenko, U. Neuner, N. Pablant, A. Pavone, K. Rahbarnia, J. Schmitt, H.M. Smith, T. Stange, Yu. Turkin, and the W7-X Team.
Validation of theory-based models for the control of plasma currents in w7-x divertor plasmas.
Nuclear Fusion, 61(12):126022, oct 2021.

[69] T. Klinger, T. Andreeva, S. Bozhenkov, C. Brandt, R. Burhenn, B. Buttenschön, G. Fuchert, B. Geiger, O. Grulke, H.P. Laqua, N. Pablant, K. Rahbarnia, T. Stange, A. von Stechow, N. Tamura, H. Thomsen, Y. Turkin, T. Wegner, I. Abramovic, S. Äkäslompolo, J. Alcuson, P. Aleynikov, K. Aleynikova, A. Ali, A. Alonso, G. Anda, E. Ascasibar, J.P. Bähner, S.G. Baek, M. Balden, J. Baldzuhn, M. Banduch, T. Barbui, W. Behr, C. Beidler, A. Benndorf, C. Biedermann, W. Biel, B. Blackwell, E. Blanco, M. Blatzheim, S. Ballinger, T. Bluhm, D. Böckenhoff, B. Böswirth, L.-G. Böttger, M. Borchardt, V. Borsuk, J. Boscary, H.-S. Bosch, M. Beurskens, R. Brakel, H. Brand, T. Bräuer, H. Braune, S. Brezinsek, K.-J. Brunner, R. Bussiahn, V. Bykov, J. Cai, I. Calvo, B. Cannas, A. Cappa, A. Carls, D. Carralero, L. Carraro, B. Carvalho, F. Castejon, A. Charl, N. Chaudhary, D. Chauvin, F. Chernyshev, M. Cianciosa, R. Citarella, G. Claps, J. Coenen, M. Cole, M.J. Cole, F. Cordella, G. Cseh, A. Czarnecka, K. Czerski, M. Czerwinski, G. Czymek, A. da Molin, A. da Silva, H. Damm, A. de la Pena, S. Degenkolbe, C.P. Dhard, M. Dibon, A. Dinklage, T. Dittmar, M. Drevlak, P. Drewelow, P. Drews, F. Durodie, E. Edlund, P. van Eeten, F. Effenberg, G. Ehrke, S. Elgeti, M. Endler,

D. Ennis, H. Esteban, T. Estrada, J. Fellinger, Y. Feng, E. Flom, H. Fernandes, W.H. Fietz, W. Figacz, J. Fontdecaba, O. Ford, T. Fornal, H. Frerichs, A. Freund, T. Funaba, A. Galkowski, G. Gantenbein, Y. Gao, J. García Regaña, D. Gates, J. Geiger, V. Giannella, A. Gogoleva, B. Goncalves, A. Goriaev, D. Gradic, M. Grahl, J. Green, H. Greuner, A. Grosman, H. Grote, M. Gruca, C. Guerard, P. Hacker, X. Han, J.H. Harris, D. Hartmann, D. Hathiramani, B. Hein, B. Heinemann, P. Helander, S. Henneberg, M. Henkel, J. Hernandez Sanchez, C. Hidalgo, M. Hirsch, K.P. Hollfeld, U. Höfel, A. Hölting, D. Höschen, M. Houry, J. Howard, X. Huang, Z. Huang, M. Hubeny, M. Huber, H. Hunger, K. Ida, T. Ilkei, S. Illy, B. Israeli, S. Jablonski, M. Jakubowski, J. Jelonnek, H. Jenzsch, T. Jesche, M. Jia, P. Junghanns, J. Kacmarczyk, J.-P. Kallmeyer, U. Kamionka, H. Kasahara, W. Kasparek, Y.O. Kazakov, N. Kenmochi, C. Killer, A. Kirschner, R. Kleiber, J. Knauer, M. Knaup, A. Knieps, T. Kobarg, G. Kocsis, F. Köchl, Y. Kolesnichenko, A. Könies, R. König, P. Kornejew, J.-P. Koschinsky, F. Köster, M. Krämer, R. Krampitz, A. Krämer-Flecken, N. Krawczyk, T. Kremeyer, J. Krom, M. Krychowiak, I. Ksiazek, M. Kubkowska, G. Kühner, T. Kurki-Suonio, P.A. Kurz, S. Kwak, M. Landreman, P. Lang, R. Lang, A. Langenberg, S. Langish, H. Laqua, R. Laube, S. Lazerson, C. Lechte, M. Lennartz, W. Leonhardt, C. Li, C. Li, Y. Li, Y. Liang, C. Linsmeier, S. Liu, J.-F. Lobsien, D. Loesser, J. Loizu Cisquella, J. Lore, A. Lorenz, M. Losert, A. Lücke, A. Lumsdaine, V. Lutsenko, H. Maaßberg, O. Marchuk, J.H. Matthew, S. Marsen, M. Marushchenko, S. Masuzaki, D. Maurer, M. Mayer, K. McCarthy, P. McNeely, A. Meier, D. Mellein, B. Mendelevitch, P. Mertens, D. Mikkelsen, A. Mishchenko, B. Missal, J. Mittelstaedt, T. Mizuuchi, A. Mollen, V. Moncada, T. Mönnich, T. Morisaki, D. Moseev, S. Murakami, G. Náfrádi, M. Nagel, D. Naujoks, H. Neilson, R. Neu, O. Neubauer, U. Neuner, T. Ngo, D. Nicolai, S.K. Nielsen, H. Niemann, T. Nishizawa, R. Nocentini, C. Nührenberg, J. Nührenberg, S. Obermayer, G. Offermanns, K. Ogawa, J. Ölmanns, J. Ongena, J.W. Oosterbeek, G. Orozco, M. Otte, L. Pacios Rodriguez, N. Panadero, N. Panadero Alvarez, D. Papenfuß, S. Paqay, E. Pasch, A. Pavone, E. Pawelec, T.S. Pedersen, G. Pelka, V. Perseo, B. Peterson, D. Pilopp, S. Pingel, F. Pisano, B. Plaum, G. Plunk, P. Pölöskei, M. Porkolab, J. Proll, M.-E. Puiatti, A. Puig Sitjes, F. Purps, M. Rack, S. Récsei, A. Reiman, F. Reimold, D. Reiter, F. Remppel, S. Renard, R. Riedl, J. Riemann, K. Risse, V. Rohde, H. Röhlinger, M. Romé, D. Rondeshagen, P. Rong, B. Roth, L. Rudischhauser, K. Rummel, T. Rummel, A. Runov, N. Rust, L. Ryc,

S. Ryosuke, R. Sakamoto, M. Salewski, A. Samartsev, E. Sanchez, F. Sano, S. Satake, J. Schacht, G. Satheeswaran, F. Schauer, T. Scherer, J. Schilling, A. Schlaich, G. Schlisio, F. Schluck, K.-H. Schlüter, J. Schmitt, H. Schmitz, O. Schmitz, S. Schmuck, M. Schneider, W. Schneider, P. Scholz, R. Schrittwieser, M. Schröder, T. Schröder, R. Schroeder, H. Schumacher, B. Schweer, E. Scott, S. Sereda, B. Shanahan, M. Sibilia, P. Sinha, S. Sipliä, C. Slaby, M. Sleczka, H. Smith, W. Spiess, D.A. Spong, A. Spring, R. Stadler, M. Stejner, L. Stephey, U. Stridde, C. Suzuki, J. Svensson, V. Szabó, T. Szabolics, T. Szepesi, Z. Szökefalvi-Nagy, A. Tancetti, J. Terry, J. Thomas, M. Thumm, J.M. Travere, P. Traverso, J. Tretter, H. Trimino Mora, H. Tsuchiya, T. Tsujimura, S. Tulipán, B. Unterberg, I. Vakulchyk, S. Valet, L. Vano, B. van Milligen, A.J. van Vuuren, L. Vela, J.-L. Velasco, M. Vergote, M. Vervier, N. Vianello, H. Viebke, R. Vilbrandt, A. Vorköper, S. Wadle, F. Wagner, E. Wang, N. Wang, Z. Wang, F. Warmer, T. Wauters, L. Wegener, J. Weggen, Y. Wei, G. Weir, J. Wendorf, U. Wenzel, A. Werner, A. White, B. Wiegel, F. Wilde, T. Windisch, M. Winkler, A. Winter, V. Winters, S. Wolf, R.C. Wolf, A. Wright, G. Wurden, P. Xanthopoulos, H. Yamada, I. Yamada, R. Yasuhara, M. Yokoyama, M. Zanini, M. Zarnstorff, A. Zeitler, D. Zhang, H. Zhang, J. Zhu, M. Zilker, A. Zocco, S. Zoletnik, and M. Zuin.
Overview of first Wendelstein 7-X high-performance operation.
Nuclear Fusion, 59(11):112004, nov 2019.

[70] K. Wanatabe, S. Sakakibara, and H. Sasao et al.
Study of time evolution of toroidal current in lhd.
Journal of Plasma Fusion Research, 5(11):124–130, 2002.

[71] S. Äkäslompolo, M. Drevlak, Y. Turkin, S. Bozhenkov, T. Jesche, J. Kontula, T. Kurki-Suonio, and R.C. Wolf.
Modelling of NBI ion wall loads in the W7-X stellarator.
Nuclear Fusion, 58(8):082010, aug 2018.

[72] V R Winters, F Reimold, R König, M Krychowiak, T Romba, C Biedermann, S Bozhenkov, P Drewelow, M Endler, Y Feng, H Frerichs, G Fuchert, J Geiger, Y Gao, J H Harris, M Jakubowski, P Kornejew, T Kremeyer, H Niemann, E Pasch, A Puig-Sitjes, G Schlisio, E R Scott, and G A Wurden.
Emc3-eirene simulation of first wall recycling fluxes in w7-x with relation to h-alpha measurements.

Plasma Physics and Controlled Fusion, 63:045016, 4 2021.

[73] Samuel A. Lazerson, Oliver Ford, Simppa Äkaslompolö, Sergey Bozhenkov, Christoph Slaby, Lilla Vanó, Annabelle Spanier, Paul McNeely, Norbert Rust, Dirk Hartmann, Peter Poloskei, Birger Buttenscho, Rainer Burhenn, Naoki Tamura, Rene Bussiahn, Thomas Wegner, Michael Drevlak, Yuriy Turkin, Kunihiro Ogawa, Jens Knauer, Kai Jakob Brunner, Ekkehard Pasch, Marc Beurskens, Hannes Damm, Golo Fuchert, Philipp Nelde, Evan Scott, Novimir Pablant, Andreas Langenberg, Peter Traverso, Pranay Valson, Uwe Hergenhahn, Andrea Pavone, Kian Rahbarnia, Tamara Andreeva, Jonathan Schilling, Christian Brandt, Ulrich Neuner, Henning Thomsen, Neha Chaudhary, Udo Höefel, Torsten Stange, Gavin Weir, Nikolai Marushchenko, Marcin Jakubowski, Adnan Ali, Yu Gao, Holger Niemann, Aleix Puig Sitjes, Ralf Koenig, Ralf Schroeder, Niek den Harder, Bernd Heinemann, Christian Hopf, Rudolf Riedl, Robert C. Wolf, and the W7-X Team.
First neutral beam experiments on Wendelstein 7-X.
Nuclear Fusion, 61(9):096008, sep 2021.